REACTIVE TRANSPORT IN THE FRACTURE-ROCK MATRIX SYSTEM AND THE CARBONATE DIAGENESIS

A Dissertation

by

RENJIE ZHOU

Submitted to the Office of Graduate and Professional Studies of
Texas A&M University
in partial fulfillment of the requirements for the degree of

DOCTOR OF PHILOSOPHY

Chair of Committee,	Hongbin Zhan
Committee Members,	Benchun Duan
	David W. Sparks
	Yalchin Efendiev
Head of Department,	Michael Pope

December 2018

Major Subject: Geology

ABSTRACT

The study of reactive transport processes is the basis of characterizing transport behaviors in many disciplines. This dissertation mainly investigates the reactive solute transport problems in two categories: reactive solute transport in fracture-rock matrix system and applications of the coupled depositional-reactive transport of strontium and calcium in the deep-sea carbonate sediments during diagenesis.

Concretely, the following scenarios of reactive solute transport in a single fracture are discussed: 1). Many single fractures in the field are filled with sediments, and the transport in such filled single fractures has received much less attention up to present. This study deals with a coupled three-domain transport problem using mobile and immobile domains to characterize a filled single fracture and a matrix domain to characterize the rock. 2). When transport properties are asymmetrically distributed in the adjacent rock matrixes, reactive solute transport needs to be considered as a coupled three-domain problem. Mathematical models are developed for such a problem under the first-type and the third-type boundary conditions to analyze the spatial-temporal concentration and mass distribution in the system 3). Due to the natural heterogeneity of porous media, the fracture dispersivity exhibits to be scale-dependent. This study investigated linear-scale and exponential-scale dependent dispersivities against constant dispersity.

The reactive transport modeling is a powerful tool to understand and quantitatively analyze the coupled physical, chemical and biological processes of Earth system. A well-designed model has a better potential to describe the interactions between different processes over large spatial and time scales. This dissertation focuses on the following carbonate diagenesis problems: 1). the model developed in this study estimates the recrystallization and precipitation rates of carbonate sediments and further reconstructs past chemical conditions in the ocean by matching the present measurements of strontium and calcium concentrations in the pore fluids. 2). Mechanical compaction and chemical cementation are responsible for the porosity reduction with depth in carbonate rocks. This coupled model is applied to distinguish the mechanical compaction and chemical compaction and estimate their relative importance on the total porosity reduction. 3). The model is further applied to various sites with different conditions, such as sedimentation rates and carbonate calcite contents. The general relationship between the calcite recrystallization rates and sedimentation conditions will be discussed and summarized.

DEDICATION

To my beloved family

ACKNOWLEDGEMENTS

First, I would like to express my sincere gratitude to my advisor, Dr. Hongbin Zhan for encouraging my research, for his patience, motivation and immense knowledge. His guidance is critical for me all the time. This work would not be possible without Dr. Zhan’s help.

Besides, my advisor, I would like to thank the rest of my thesis committee: Dr. Benchun Duan, Dr. Yalchin Efendiev and Dr. David W. Sparks for their insightful comments and tremendous help during the past years.

Also, I would like to thank Dr. Shuo Zhang for his generous support and kind help during my summer internship at Aramco Global Research Center.

Finally, I would like to thank my family for their constant support in every aspect. Especially, I greatly thank my wife, Dr. Yanyan Zhang, for her love and encouragement all the time.

CONTRIBUTORS AND FUNDING SOURCES

Contributor

This work was supervised by a dissertation committee consisting of Dr. Hongbin Zhan (advisor), Dr. Benchun Duan and Dr. David W. Sparks of the Department of Geology & Geophysics [Home Department], and Dr. Yalchin Efendiev of the Department of Mathematics [Outside Department].

Dr. Hongbin Zhan provided support for the analytical derivations and discussion for Chapters 2, 3, and 4. Besides, Dr. Shuo Zhang of Aramco Global Research Center provided generous help in the development of models and ideas for Chapters 5 and 6.

All the work conducted for the dissertation was completed by the student.

Funding Sources

Graduate study was supported by a teaching assistant grant from Department of Geology & Geophysics and by my family’s support.

TABLE OF CONTENTS

LIST OF FIGURES

Page

LIST OF TABLES

1. INTRODUCTION

1.1 Background and goals

Reactive transport modeling has been considered as an important method to understand the complex processes in Earth system. It makes a significant impact on the studies of solute transport in fractured media, which have been studied by many scholars for more than three decades because of its broad range of applications in different disciplines (Grisak and Pickens, 1981; Roubinet et al., 2012). For instance, for dealing with problems such as the disposal of radioactive materials, CO_2 geological sequestration and storage (Pouya, 2012), and groundwater pollution in fractured reservoirs (Bodin et al., 2003). Since fractures are much more permeable than the surrounding rock matrix (Wilson and Witherspoon, 1970), fractures have the potential for being the most effective pathways for solute migration. For this reason, transport in the rock matrix is often highly simplified in mathematical models, for instance, limited to a diffusion-dominating process (Tang et al., 1981). Specifically, some experiments have been designed and conducted to confirm that advective transport in the rock matrix can often be ignored but diffusive transport in the rock matrix must be considered in most cases (Maloszewski and Zuber, 1993; Roubinet et al., 2012).

Understanding transport in a single fracture is the foundation of understanding transport in fracture networks (Long and Billaux, 1987; Tang et al., 1981). Analytical solutions developed at the scale of fracture-matrix systems can be applied directly to solute transport in fracture networks. This is the case for the particle-tracking methods developed by Dershowitz and Miller (1995) and Cvetkovic et al. (2004) and reviewed by

Noetinger et al. (2016). The solutions developed for a single fracture-matrix system can also be extended rather straightforwardly to deal with transport in fractured rocks with multiple parallel fractures which may or may not have the same apertures, as demonstrated in detail by Sudicky and Frind (1982), Zhu et al. (2016), and others.

There are multiple reasons to explain why investigators are interested in single fracture transport. First, this is the simplest possible fracture transport case that may be solved using an analytical approach, which can offer insights on various transport processes. Such analytical or semi-analytical solutions may serve the purpose of benchmarking numerical solutions developed for transport in a fracture-matrix system, which may suffer from non-negligible (and often hidden) numerical errors, partially because of the sharp differences of fracture and rock matrix parameters (Grisak and Pickens, 1981). One may consult Seo and Mittal (2011) for numerical challenges related to sharp interfaces (such as along a fracture-matrix boundary). Also, a thin fracture, often with an aperture on the order of millimeter or less, requires a very fine grid to discretize the fracture in numerical simulations which may not be practical for dealing with large-scale field transport problems (Weatherill et al., 2008). Secondly, a single fracture offers simple enough setting to test different transport theories related to a fracture-matrix system. Thirdly, isolated single fractures exist in real geological settings (Moreno et al., 1988; Raven et al., 1988). Because of its importance, significant effort has been put into conducting tracer transport experiments in single fractures (Brown et al., 1998; Esposito and Thomson, 1999), in addition to the theoretical works that will be briefly reviewed in the following parts.

Transport behaviors in the aquifer-aquitard system have many similarities as those in the single fracture-rock matrix system. The much more permeable aquifer/fracture is distributed in the middle tight layers (aquitards/rock matrix) with very small permeabilities.

Thus, my first goal of this dissertation is to refine and extend the related theory of solute transport in fracture-matrix and aquifer-aquitard systems. Chapter 2 mainly investigates the solute transport in a filled single fracture-rock matrix system under unilateral and radial flows. Then, reactive solute transport in an asymmetrical single fracture system or aquifer-aquitard system are proposed in Chapter 3. Chapter 4 investigates the schemes of possible scale-dependent dispersivity in the aquifer-aquitard system or fracture zone.

On the other hand, the reactive transport modeling can be used to investigate the early diagenesis of carbonate rocks. The transport of chemical elements in the pore fluids are mainly controlled by advection and diffusion. Meanwhile, the chemical elements in the pore fluids are interacted with those in the carbonate solid during diagenesis. Carbonate calcite slowly dissolves after the carbonate is deposited in the ocean. At the same time, secondary calcite is precipitated from the associated pore fluids. In this study, strontium, calcium and sulfate in the carbonate calcite are used as indicators and tracers of carbonate diagenetic processes. Geochemical analysis associated with numerical modeling of strontium, calcium and sulfate in the bulk carbonate and pore fluids gives the quantitative descriptions and fundamental understanding over various diagenetic processes during their deposition and compaction

(Berner, 1980; Fantle and DePaolo, 2006; Richter and Depaolo, 1987, 1988; Richter and Liang, 1993). The results of the chemical exchange as well as advective and diffusive transport within the carbonate sediments and pore fluids are recorded in the chemistry of pore fluids and solids, which can be modeled by the coupled depositional-reactive transport model. Records of trace elements, metal ratios and chemical isotopes measured in the calcium carbonate minerals and fossilized skeletons were carefully examined and compared to simulation results (De La Rocha and DePaolo, 2000; Fantle and DePaolo, 2005; Shackleton, 1967). By matching the chemical profiles in the solids and associated pore fluids, the coupled model could constrain the values of recrystallization rate and reconstruct past record of chemical conditions in the ocean.

Also, the relative importance of chemical compaction and mechanical compaction during the deposition of carbonate sediments are argued (Bathurst, 1970; Chanda et al., 1977; Weller, 1959). Bathurst (1970) indicated that carbonate sediments are not significantly influenced by the mechanical compaction because they undergo early and rapid cementation. However, Chanda et al. (1977) examined the compacted rocks for characteristics and provided evidence of mechanical compaction during lithification by checking the deformation of ooids in the Precambiran Bhander Limestone. By integrating the dissolution rate over its depositional history, this study allows to give a quantitative evaluation of the relative fractions of mechanical compaction and chemical compaction during lithification.

Thus, my second goal for this dissertation is to characterize the carbonate early diagenesis by coupling deposition and reactive transport of chemical elements, which would shed some insight for the quantifying the recrystallization and precipitation during carbonate diagenesis. After calibrating against chemical elements concentrations in the carbonate bulk, this coupled model can produce the record of the chemical conditions in the ocean for the past 40 million years, which is discussed in detail in Chapter 5. Other goals of this study demonstrated in Chapter 6 are to investigate the relationship between the values of recrystallization rate and sedimentation conditions and distinguish the chemical and mechanical compaction during the deposition and compaction.

1.2 Organization

This dissertation is organized as follows: in Chapter 2, the models of reactive transport in a filled single fracture-matrix system are discussed under both unilateral and radial flows. In Chapter 3, reactive solute transport in an asymmetric facture-rock matrix system is discussed. The existence of scale-dependent dispersivity in fracture zones or aquifer-aquitard system is carefully examined in Chapter 4. A coupled depositional and reactive solute transport model is built to explain chemical elements profiles in the porewater and reconstruct the paleo history seawater chemical conditions in the Chapter 5. The discussions of the using such a coupled model to distinguish the chemical compaction and mechanical compaction in the deep-sea carbonate sediments is demonstrated in the Chapter 6. Also, the relations between calcite dissolution rate and sedimentation conditions such as sedimentation rates and carbonate content are also indicated.

2. REACTIVE SOLUTE TRANSPORT IN A FILLED SINGLE FRACTURE-MATRIX SYSTEM UNDER UNILATERAL AND RADIAL FLOWS*

2.1 Introduction

A widely-used analytical solution of contaminant transport in a single fracture system was proposed by Tang et al. (2005). Chen (1986) also derived an approximate solution for radial transport from an injection well into a single fracture. Theoretical studies of transport in a single open fracture have been reported by numerous investigators, including Moreno et al. (1988), and Esposito and Thomson (1999). In the above-mentioned studies, fractures were assumed to be open without infillings.

However, fracture infillings are commonly observed in real applications (Bradner and Murdoch, 2005; Wealthall et al., 2001). Wealthall et al. (2001) conducted an investigation of fractures filled with sediments and compared the preferential flow pathways in such filled fractures to those in an equivalent open (unfilled) fractures. Kemp et al. (2003) evaluated filled fractures in Permo-Triassic sandstones in southwest Scotland and presented a sampling method for such fractures. Bradner and Murdoch (2005) investigated the gas-phase permeability in sand-filled fractures in a soil vapor extraction system.

A filled fracture usually has a different transport behavior from an open one. For instance, Lunati et al. (2003) found that a propagation front was smoother in single

---

* Reprinted with permission from "Reactive solute transport in a filled single fracture-matrix system under unilateral and radial flows" by Zhou, R. J., Zhan, H. B., Chen, K. W. (2017), Advances in Water Resources, 104, 183-194, Copyright [2017] by Elsevier

fractures filled with glass beads at extremely low flow velocity, compared to those in open fractures. The existence of infilling materials often leads to disconnections or dead-end water pockets between pore spaces within a fracture, which can be regarded as immobile domains (Jodar et al., 2009; Qian et al., 2011). Such a problem cannot be dealt with using the advection-dispersion equation (ADE) which is commonly used for dealing with transport in homogeneous porous media or open fractures, as done by Tang et al. (1981) for unilateral flow, and by Chen (1986) for radial flow. Regarding to transport in an open fracture, there is much evidence showing that ADE performs poorly, and cannot explain the so-called non-Fickian transport phenomena such as the early breakthrough and long tailing of the breakthrough curves (BTCs), that can, however, be satisfactorily explained with mobile-immobile models (MIM) as first proposed by van Genuchten and Wierenga (1976).

The objective of this study is to develop new mobile-immobile models for two types of transport problems in a filled single fracture-matrix system, which has not been attempted before. The following transport processes are considered: advection, longitudinal dispersion, first-order reaction, and linear sorption in the fracture; transverse molecular diffusion, first-order reaction, and linear sorption in the rock matrix; first-order mass transfer between the mobile and immobile domains in the filled fracture. The first model concerns a unilateral flow; while the second model concerns a radial flow caused by an injection/pumping well.

2.2 The conceptual model and physical setup

In this study, a filled single fracture is oriented horizontally with a constant aperture 2*b* and extends sufficiently far from the domain of interest. The fracture is bounded by a rock matrix whose permeability is at least several orders of magnitude less than that of the fracture. The rock matrix is wide enough so that the effect of the limit boundary of the rock matrix can be ignored. This is justified, as the primary transport process in the rock matrix is often limited to regions close to the fracture since it is a much slower process.

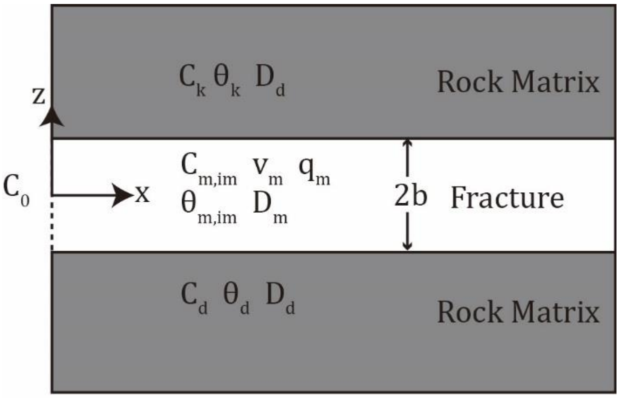

Fig. 2.1 The conceptual model of unilateral flow.

In this model, a constant-rate unilateral flow field from left to right is established (Fig. 2.1). A Cartesian coordinate system is used with the origin at the intercept of the left boundary and the middle of the fracture. The *x*-axis is along the same direction with the unilateral flow, and the *z*-axis is vertically upward. The *y*-axis is perpendicular to the *x*-axis and is horizontal as well. A solute source is located at *x*=0 with a constant concentration C_0 and extends to sufficiently far distance from the domain of interest along the *y*-axis. Thus, the problem can be conceptualized as a two-dimensional (2D) model in the *xz* plane. Such a simple boundary condition at $x = 0$ (constant concentration) can be relaxed later to accommodate more realistic boundary types, such as prescribed time-dependent concentration (first-type), prescribed flux (second-type), or Robin (third-type). Two points are notable. First, the fracture aperture is so small that the vertical mixing throughout the fracture aperture is completed almost instantaneously, thus transverse dispersion in the fracture along the *z*-axis has no discernible effect on transport processes in the fracture-matrix system and is not considered. Roubinet et al. (2012) further reported that longitudinal diffusion in the rock matrix affected solute transport only when the Peclet number was very low (less than 0.01). Rezaei et al. (2016) also investigated the horizontal dispersion in the aquitard (HDA) on reactive solute transport in an aquifer-aquitard system, which is similar to the fracture-matrix system investigated here except that slow water flow (advection) in aquitard was considered by Rezaei et al. (2016) and water flow in matrix is excluded in this study. Rezaei et al. (2016) concluded that HDA was negligible for most practical cases of transport. Therefore, longitudinal diffusion in the rock matrix is neglected in both models of this study. Secondly, despite the fact that the fracture is filled, it could still be very porous and very permeable.

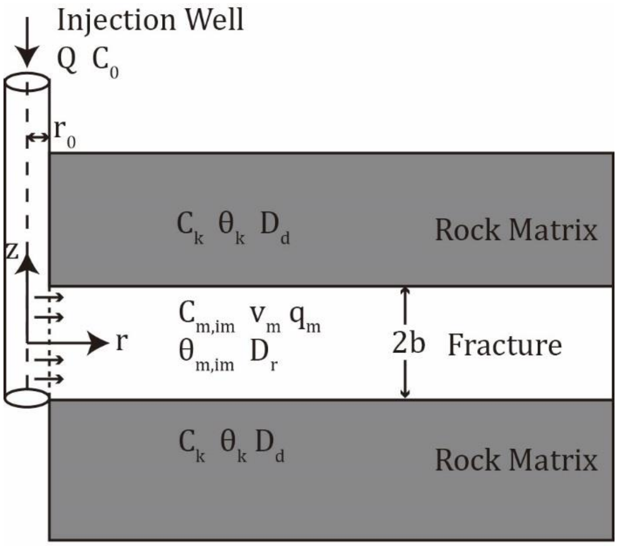

Fig. 2.2 The conceptual model of radial flow.

The conceptual model of radial flow is the same as that of unilateral flow but with the following exceptions (Fig. 2.2). A radial flow field rather than a unilateral flow field is established due to an injection/pumping well with a constant rate *Q* (positive for injection and negative for pumping). Accordingly, a cylindrical coordinate system rather than a Cartesian coordinate system is utilized with the radial *r*-axis horizontally outward while the *z*-axis is vertically upward and along the center of the well, with the origin located at the intercept point of the horizontal symmetry plane of the fracture and the *z*-axis (see Fig. 2.2). Groundwater flow is driven only by the injection/pumping well, without any other regional flow presented for the radial flow model.

2.3 Mathematical models and solutions

Based on the conceptual models described above, one can establish the mathematical models for both unilateral and radial flows. As two different coordinate systems are employed, the mathematical models are quite different. We will start with the unilateral flow model, followed by the radial flow model. Since the investigated system is symmetric which respect to the plane of z=0, we will only discuss the half-plane above z=0 hereinafter.

2.3.1 Mathematical model and solutions of unilateral flow

Reactive solute transport in a filled single fracture and rock matrix system can be described as three governing equations:

$$\theta_m R_1 \frac{\partial C_m}{\partial t} + \theta_{im} R_2 \frac{\partial C_{im}}{\partial t} = \theta_m D_m \frac{\partial^2 C_m}{\partial x^2} - \theta_m v_m \frac{\partial C_m}{\partial x} - \theta_m \lambda_1 R_1 C_m - \theta_{im} \lambda_2 R_2 C_{im} - \frac{q_m}{b} \ , \qquad (2.1)$$

$$\theta_{im} R_2 \frac{\partial C_{im}}{\partial t} = \omega (C_m - C_{im}) - \theta_{im} \lambda_2 R_2 C_{im} \ , \qquad (2.2)$$

$$R_3 \frac{\partial C_k}{\partial t} = D_d \frac{\partial^2 C_k}{\partial z^2} - \lambda_3 R_3 C_k \ . \qquad (2.3)$$

where C_m [M/L^3] and C_{im} [M/L^3] are the concentrations in the mobile and immobile domains in the fracture, respectively; C_k [M/L^3] is the concentration in the rock matrix; b [L] is the fracture half-aperture; v_m [L/T] is the groundwater velocity in the mobile domain, which equals q/θ_m; q [L/T] is the Darcian velocity; λ [1/T] is the decay constant which is defined as ln2/$t_{1/2}$ where $t_{1/2}$ is the half-life of the radionuclide or biodegradable species; θ_m and θ_{im} are the mobile and immobile water contents, respectively, and the sum of θ_m and θ_{im} is the total porosity of the fracture; ω [1/T] is the first-order mass transfer rate between the mobile and immobile domains; R is the retardation factor (constant); the subscripts 1, 2 and 3 of R and λ refer to the mobile domain of the fracture, the immobile domain of the fracture, and the matrix, respectively; D_m [L^2/T] is the longitudinal dispersion coefficient in the fracture, and it can be further expressed as:

$$D_m = \alpha_L v_m + D^* \ , \tag{2.4}$$

where α_L [L] is the longitudinal dispersivity while D^* [L^2/T] is the effective molecular diffusion coefficient in the mobile domain, which is usually much smaller than $\alpha_L v_m$ and can be ignored; D_d [L^2/T] is the effective molecular diffusion coefficient in the rock matrix; q_m [M/L^2T] is the diffusive mass flux between the fracture and the rock matrix, and is expressed based on Fick's law:

$$q_m = -\theta_k D_d \left(\frac{\partial C_k}{\partial z}\right)\bigg|_{z=b} \ , \tag{2.5}$$

where θ_k is the porosity of the rock matrix.

Eqs. (2.1)-(2.3) refer to the governing equations in the mobile domain of the fracture, mass transfer between the mobile and immobile domains of the fracture, and the governing equation in the rock matrix, respectively.

There are a few notable points about Eqs. (2.1)-(2.3). First, different decay constants are used for the mobile and immobile domains, as well as for the rock matrix, which are likely to have different reaction rate constants (Zhu et al., 2016). For example, biodegradation would be affected by water temperature, type and content of organic compounds, oxygen concentration and other factors (Davis et al., 2013; Johnson and Furrer, 2002). Some of these factors could be different in the mobile and immobile domains of a fracture and matrix.

Secondly, the retardation factors in the mobile and immobile domains of a fracture could be different (Parker and Valocchi, 1986; Wierenga and Vangenuchten, 1989). The retardation factors of the mobile and immobile domains are defined as $R_1 = 1 + \rho_m K_m / \theta_m$; $R_2 = 1 + \rho_{im} K_{im} / \theta_{im}$, where ρ_m and ρ_{im} are the partial bulk densities of the mobile and immobile domains, respectively; K_m and K_{im} are the distribution coefficients for each domain and represent the mass of solute absorbed per unit volume of solid divided by the concentration of the solute in the fracture. Since the bulk density, distribution coefficient and porosity in the rock matrix may be different from those in the fracture, the retardation factor of the rock matrix could be very different from that of the fracture.

As multiple parameters are involved in the mathematical models illustrated above, it is necessary to elaborate on the parameter determination process for model application. This will be addressed later.

Experimental and theoretical efforts have been made by many scholars to understand the possible existence of concentration discontinuity at the sharp interface between the fracture and the rock matrix (Berkowitz et al., 2009; Leij et al., 1991). Such a phenomenon may occur if there are possible mass accumulations when solutes cross from one medium to another (Marseguerra and Zoia, 2006). However, no experimental evidence of mass accumulation at the sharp interface is available to support this conjecture (Zhang et al., 2010). Thus, the concentration discontinuity at the fracture-matrix interface is not considered in this study. The above equations are supplemented with a continuity equation at the fracture-matrix interface and initial and boundary conditions to close the system. At any point on the interface between the fracture and rock matrix, the concentration is continuous, thus one has:

$$C_m(x,t) = C_k(x, z = b, t)\,. \tag{2.6}$$

The fracture-matrix system is assumed to be free from solute at the beginning, thus the initial conditions are:

$$C_m(x, t = 0) = C_{im}(x, t = 0) = C_k(z, t = 0) = 0\,. \tag{2.7}$$

The remaining boundary conditions are as follows:

$$C_m(x \to \infty, t) = C_{im}(x \to \infty, t) = 0\,, \tag{2.8}$$

$$C_m(x = 0, t) = C_0\,, \tag{2.9}$$

$$C_k(z \to \infty, t) = 0\,. \tag{2.10}$$

Eqs. (2.8) and (2.10) imply that the fracture is infinitely long and the rock matrix is infinitely thick, which avoid the effect of the finite boundary. Eq. (2.9) defines a constant concentration source in the mobile domain of the fracture at *x*=0.

To solve Eqs. (2.1)-(2.10), the Laplace transform will be used to transform the problems in the real-time domain to those in the Laplace domain. The benefit of this approach is to convert partial differential equations (which are usually difficult to deal with) into ordinary differential equations by removing the time-derivative terms from the equations. After solving the boundary value problems (BVP), one can obtain analytical solutions of the problems in the Laplace domain. After this step, one needs to apply an inverse Laplace transform technique, which has to be numerical for the problems addressed here, to finally obtain solutions in the real-time domain.

Before conducting the Laplace transform, it is helpful to convert the equations into their dimensionless forms that have fewer numbers of independent variables and are more reflective of the systems involved, as commonly done in dynamic analysis (Bear, 1972; Simmons et al., 2001).

The Laplace-domain solutions are obtained as follows while the detailed derivations are provided in Appendix A of the supplementary files:

$$\overline{C_{mD}} = \frac{1}{p}\exp\left(\frac{Pe-\sqrt{Pe^2+4k_1}}{2}x_D\right), \tag{2.11}$$

$$\overline{C_{imD}} = \frac{1}{p}\frac{\omega}{\frac{\theta_{im}R_2 p}{\alpha}+\omega+\lambda_2\theta_{im}R_2}\exp\left(\frac{Pe-\sqrt{Pe^2+4k_1}}{2}x_D\right), \tag{2.12}$$

$$\overline{C_{kD}} = \frac{1}{p}\exp\left(\frac{Pe-\sqrt{Pe^2+4k_1}}{2}x_D+\sqrt{\lambda_3\alpha+p}\left(\sqrt{\frac{R_3D_m}{R_1D_d}}-z_D\right)\right). \tag{2.13}$$

Where the subscript *D* denotes the terms in dimensionless formats hereinafter, the details of dimensionless formats are discussed in Appendix A,

$k_1 = p+\left(p+\lambda_2\alpha\right)\times\theta_1\frac{R_2}{R_1}\times\frac{\omega}{\frac{\theta_{im}R_2 p}{\alpha}+\omega+\lambda_2\theta_{im}R_2}+\lambda_1\alpha+\alpha_1\sqrt{\lambda_3\alpha+p}$, and the Peclet number (*Pe*) and all other terms are explained in the supplementary file.

For some transport problems, it is possible to obtain steady-state solutions that are usually much simpler than the transient solutions. The steady-state solutions will be particularly useful for assessing the long-term transport behavior, thus they are sometimes required for screening and/or designing long-term monitoring and remediation plans.

To obtain the steady-state solutions for the unilateral flow model, one must fulfill the following condition:

$$\frac{\partial C_{mD}}{\partial t_D} = \frac{\partial C_{imD}}{\partial t_D} = \frac{\partial C_{kD}}{\partial t_D} = 0\,. \tag{2.14}$$

Eq. (2.14) indicates that concentrations would no longer change with time any more after reaching steady state, which simplifies Eqs. (2.1) and (2.2) to ordinary differential equations. The steady-state solutions can be reached by substituting Eq. (2.14) into Eqs. (2.1)-(2.3), or taking advantage of the following identity: $f(t_D \to \infty) = \lim_{p \to 0}(pF(p))$, where $F(p)$ is the Laplace transform of $f(t_D)$and $f(t_D \to \infty)$ is the steady-state solution of $f(t_D)$. In this case, $F(p)$ corresponds to the solutions in the Laplace domain (Eqs. (2.11)-(2.13)). Thus, the steady-state solutions of the mobile and immobile domains of the fracture and the matrix are derived by calculating the limitations of $p\overline{C_{mD}}$, $p\overline{C_{\imath mD}}$ and $p\overline{C_{kD}}$ as p approaches 0.

The analytical solutions for C_{mD}, C_{imD} and C_{kD} at steady state can be derived as follows:

$$C_{mD} = exp\left(\frac{Pe - \sqrt{Pe^2 + 4\left(\lambda_2 \theta_1 \alpha \times \frac{R_2}{R_1} \times \frac{\omega}{\omega + \lambda_2 \theta_{im} R_2} + \lambda_1 \alpha + \alpha_1 \sqrt{\alpha \lambda_3} \right)}}{2} x_D \right), \tag{2.15}$$

$$C_{imD} = \frac{\omega}{\omega + \theta_{im} \lambda_2 R_2} exp\left(\frac{Pe - \sqrt{Pe^2 + 4\left(\lambda_2 \theta_1 \alpha \times \frac{R_2}{R_1} \times \frac{\omega}{\omega + \lambda_2 \theta_{im} R_2} + \lambda_1 \alpha + \alpha_1 \sqrt{\alpha \lambda_3} \right)}}{2} x_D \right), \tag{2.16}$$

$$C_{kD} = exp\left(\frac{Pe - \sqrt{Pe^2 + 4\left(\frac{R_2}{R_1} \frac{\lambda_2 \theta_1 \alpha \omega}{\omega + \lambda_2 \theta_{im} R_2} + \lambda_1 \alpha + \alpha_1 \sqrt{\alpha \lambda_3} \right)}}{2} x_D - \sqrt{\lambda_3 \alpha} \left(z_D - \sqrt{\frac{R_3 D_m}{R_1 D_d}} \right) \right). \tag{2.17}$$

It is interesting to point out that the steady-state solutions of Eqs. (2.15)-(2.17) are all exponential decay functions of spatial coordinates, and are closely related to the Peclet number (*Pe*) in the fracture, in addition to other factors.

2.3.2 Mathematical model and solutions of radial flow

In the radial flow model, the solute is discharged into a filled fracture-matrix system from an injection well at a constant rate Q [L^3/T]. r_0 [L] is the radius of the well. The velocity of the background regional groundwater flow is ignored. Thus, the steady-state flow velocity in the mobile zone of the fracture is only caused by the injection well, which is expressed as:

$$v_m = \frac{A}{r}, \tag{2.18}$$

where $A = \frac{Q}{4\pi b\theta_e}$, and θ_e is the effective porosity in the fracture, which equals the mobile water content θ_m in this study.

The flow velocity is steady with time but variable with radial distance from the well. The radial hydrodynamic dispersion coefficient D_r [L^2/T] is expressed as (Bear, 1972):

$$D_r = dv_m = \frac{dA}{r}, \tag{2.19}$$

where d [L] is the radial dispersivity. The governing equations in the mobile and immobile domains of the fracture can be written as follows:

$$\theta_m R_1 \frac{\partial C_m}{\partial t} + \theta_{im} R_2 \frac{\partial C_{im}}{\partial t} = \theta_m D_r \frac{\partial^2 C_m}{\partial r^2} - \theta_m \frac{A}{r}\frac{\partial C_m}{\partial r} - \theta_m \lambda_1 R_1 C_m - \theta_{im} \lambda_2 R_2 C_{im} - \frac{q_m}{b}, \tag{2.20}$$

$$\theta_{im} R_2 \frac{\partial C_{im}}{\partial t} = \omega(C_m - C_{im}) - \theta_{im} \lambda_2 R_2 C_{im} \ , \tag{2.21}$$

where the diffusive flux between the fracture and matrix, q_m, has the same expression as above in Eq. (2.5) in the unilateral flow model and The governing equation for the reactive solute transport in the rock matrix is the same as above in Eq.(2.3). The boundary conditions of the filled fracture-matrix system in the radial flow model are expressed as follows:

$$C_m(r \to \infty, t) = C_{im}(r \to \infty, t) = 0, \tag{2.22}$$

$$C_m(r = r_0, t) = C_0 . \tag{2.23}$$

The boundary condition for the matrix is the same as Eq. (2.10). Eq. (2.22) specifies that the effect of the system boundary is infinite in the *r* axis. The boundary condition given in Eq. (2.23) illustrates that the source concentration at the injection well remains constant C_0. This boundary condition can be replaced with other boundary types such as time-dependent prescribed concentration, flux prescribed (second-type), or Robin (third-type), if needed. The initial conditions for the fracture and rock matrix are the same as Eq. (2.7). At the interface between the fracture and rock matrix, the continuity relationship holds (see Eq. (2.6) in the unilateral flow model).

The solutions in the Laplace domain are obtained as follows while the full derivations are provided in Appendix B of the supplementary files:

$$\overline{C_{mD}} = \frac{1}{p}\exp\left(\frac{1}{2}\left(r_D - r_{0D}\right)\right)\frac{Ai\left[\beta^{1/3}\left(r_D + \left(4\beta\right)^{-1}\right)\right]}{Ai\left[\beta^{1/3}\left(r_{0D} + \left(4\beta\right)^{-1}\right)\right]} , \tag{2.24}$$

$$\overline{C_{imD}} = \frac{1}{p}\frac{\omega}{\frac{\theta_{im} p R_2}{\tau} + \omega + \lambda_2 \theta_{im} R_2}\exp\left(\frac{1}{2}\left(r_D - r_{0D}\right)\right)\frac{Ai\left[\beta^{1/3}\left(r_D + \left(4\beta\right)^{-1}\right)\right]}{Ai\left[\beta^{1/3}\left(r_{0D} + \left(4\beta\right)^{-1}\right)\right]} , \tag{2.25}$$

$$\overline{C_{kD}} = \frac{1}{p}\exp\left(\frac{1}{2}\left(r_D - r_{0D}\right) - \sqrt{\tau\lambda_3 + p}\left(z_D - \frac{b}{d}\sqrt{\frac{R_3 A}{R_1 D_d}}\right)\right)\frac{Ai\left[\beta^{1/3}\left(r_D + \left(4\beta\right)^{-1}\right)\right]}{Ai\left[\beta^{1/3}\left(r_{0D} + \left(4\beta\right)^{-1}\right)\right]} , \tag{2.26}$$

where $\beta = \left(\tau\lambda_1 + \tau_1\sqrt{\tau\lambda_3 + p} + p + \frac{R_2}{R_1} \times \frac{\left(p + \lambda_2\tau\right)\theta_1\omega}{\frac{\theta_{im} pR_2}{\tau} + \omega + \lambda_2\theta_{im}R_2} \right)$, A_i is the so-called Airy function.

Similar to the derivation of the steady-state solutions of the unilateral flow model, to reach the steady state, Eq. (2.14) must be fulfilled. The analytical solutions of the concentration distribution in the mobile domain (Eq. (2.27)), immobile domain (Eq. (2.28)) and rock matrix (Eq. (2.29)) can be obtained in the real-time domain as follows:

$$C_{msD} = \exp\left(\frac{1}{2}\left(r_D - r_{0D}\right)\right) \frac{Ai\left[\beta_1^{1/3}\left(r_D + \left(4\beta_1\right)^{-1}\right)\right]}{Ai\left[\beta_1^{1/3}\left(r_{0D} + \left(4\beta_1\right)^{-1}\right)\right]} \ , \tag{2.27}$$

$$C_{imsD} = \frac{\omega}{\omega + \lambda_2\theta_{im}R_2} \exp\left(\frac{1}{2}\left(r_D - r_{0D}\right)\right) \frac{Ai\left[\beta_1^{1/3}\left(r_D + \left(4\beta_1\right)^{-1}\right)\right]}{Ai\left[\beta_1^{1/3}\left(r_{0D} + \left(4\beta_1\right)^{-1}\right)\right]} \ , \tag{2.28}$$

$$C_{ksD} = \exp\left(\frac{1}{2}\left(r_D - r_{0D}\right) - \sqrt{\tau\lambda_3}\left(z_D - \frac{b}{d}\sqrt{\frac{R_3 A}{R_1 D_d}}\right)\right) \frac{Ai\left[\beta_1^{1/3}\left(r_D + \left(4\beta_1\right)^{-1}\right)\right]}{Ai\left[\beta_1^{1/3}\left(r_{0D} + \left(4\beta_1\right)^{-1}\right)\right]} \ , \tag{2.29}$$

where $\beta_1 = \left(\tau\lambda_1 + \tau_1\sqrt{\tau\lambda_3} + \frac{R_2}{R_1} \times \frac{\lambda_2\tau\theta_1\omega}{\omega + \lambda_2\theta_{im}R_2} \right)$.

2.4 Validation and results

Now all transient solutions for both models are derived in the Laplace domain. Analytical inverse Laplace transforms might result in complex multiple integrations which can only be calculated with numerical methods (Chen, 1986; Tang et al., 1981;

Zhan et al., 2009a). Therefore, a numerical inverse Laplace transform technique is adopted here to compute the spatial-temporal concentration distributions. The de Hoog et al. (1982) algorithm, which has been successfully used in solute transport problems before (Furman and Neuman, 2003; Wang and Zhan, 2015), is selected to conduct the numerical inverse Laplace transform here. It accelerates the convergence of the Fourier series resulting from the inversion integral and ensures the accuracy by reducing errors (De Hoog et al., 1982). The results obtained from the de Hoog algorithm are then tested against other analytical solutions: those from Tang et al. (1981) and Zhu et al. (2016) for unilateral flow, and the other from Chen (1986) for radial flow.

2.4.1 Breakthrough curves (BTCs) analysis

To better illustrate the above derived solutions, an example is used to analyze BTCs of the mobile domain in the fracture. The parameters used in the example are taken from previous studies (Schumer et al., 2003; Tang et al., 1981), which dealt with similar transport problems without considering fracture infillings. The same parameters are used for example calculations of both models:

$2b = 100$ μm; $\theta_k = 0.01$; $t_{1/2} = 12.35$ yrs; $R_1 = 1$; $R_2 = 1$; $R_3 = 1$; $D_d = 1.38 \times 10^{-5}\ \mathrm{m}^2/\mathrm{d}$; $\alpha_L = 0.5$ m; $d = 0.5$ m; $\omega = 0.9/\mathrm{d}$; $\theta_m + \theta_{im} = 0.9$.

In the unilateral flow model, the Darcian velocity (q) of the groundwater in the mobile domain of the fracture is 0.01 m/d, which can be used to calculate the flow velocity of groundwater (v_m). In the radial flow model, the constant injection rate (Q) is 0.001 m^3/d, and the radius of the wellbore (r_0) is 0.11 m. The default mobile/immobile ratio in the following calculation is set to be 10 (or θ_m=0.818 and θ_{im}=0.0818). For computations involving different mobile/immobile ratios, θ_m and θ_{im} will change accordingly with the constraint of constant total porosity (θ_m+θ_{im}=0.9). A sample point of (0.5 m, 0 m) is picked in the fracture for the discussion of BTCs. The selection of such a point is rather arbitrary, thus the results obtained are general in nature.

It is worthwhile to note that some related studies use a fixed dispersion coefficient (D_m) (Tang et al., 1981; Van Genuchten and Wierenga, 1976) while others use a fixed longitudinal dispersivity (α_L) (Chen, 1987; Dronfield and Silliman, 1993) for analyzing the transport process. As Eq. (2.4) shows, the relationship between D_m and α_L can be simplified as $D_m = \alpha_L v_m = \alpha_L q / \theta_m$, if neglecting the molecular diffusion coefficient. Figs. 2.3A and 2.3B respectively show BTCs for the unilateral flow model with a fixed longitudinal dispersivity of 0.5 m and a fixed dispersion coefficient of 0.00611 m^2/d which is computed with α_L=0.5 m, q=0.01 m/d, and θ_m=0.818. Fig. 2.4A shows BTCs for the radial flow model with a radial dispersivity of 0.5 m and an injection rate of Q=0.001 m^3/d. To distinguish curves which are superposed on a linear scale, Fig. 2.4B are plotted on a semi-log scale corresponding to Fig. 2.4A.

It is also useful to know different time scales associated with the problems in order to understand the different transport behavior under unilateral and radial flows. These two models are under different conditions: the unilateral flow model refers to an ambient condition while the radial flow model corresponds to a forced hydraulic condition. The time scale of the radial flow model is about three orders of magnitude smaller than that of the unilateral flow model. For the chosen first-order mass transfer rate of $\omega = 0.9$ day^{-1}, the time scale for the mass transfer between the mobile and immobile domains is around $1/\omega \approx 1.1$ days. Now one looks at the θ_m / θ_{im} ratios of 10, 5, and 1 as used in Figs. 2.3A-B for unilateral flow, when the Darcian velocity is kept at 0.01 m/d and $\theta_m + \theta_{im}$ is kept at 0.9, such three θ_m / θ_{im} ratios will lead to advective transport times to the point of interest (0.5 m, 0 m) to be 40.9 days, 37.5 days, and 22.5 days, respectively. For radial transport shown in Figs. 2.4A-B, the advective transport time needed to a radial distance *r* from a well with an injection rate of *Q* is: $T = 0.5r^2 / A$, where *A* is defined after Eq. (2.19). One then looks at the θ_m / θ_{im} ratios of 10, 5, and 1 as used in Figs. 2.4A-2.4B and finds that the advective transport times to a point of (0.5 m, 0 m) with *Q* of 0.001 m^3/day and $\theta_m + \theta_{im}$ of 0.9 will be 0.0642 days (or 1.54 hrs), 0.0589 days (or 1.41 hrs), and 0.0353 days (or 0.85 hrs), respectively.

The solutions of Tang et al. (1981) (for unilateral flow) and Chen (1986) (for radial flow) can be regarded as special cases of this study by assuming $\theta_m = 1$ and $\theta_{im} = 0$. In other words, there is no immobile domain and the fracture is open with a porosity of 1. The solution of Tang et al. (1981) is included in Figs. 2.3A-B while the solution of Chen (1986) is included in Figs. 2.4A-B. As can be seen from these figures, excellent agreements are reached for both cases when neglecting the immobile domain of the fracture and assigning identical reaction rates and retardation factors for the fracture and the matrix.

In Fig. 2.3A, BTCs in the unilateral flow model are nearly unaffected by the mobile/immobile ratios if the longitudinal dispersivity is fixed. This observation can be explained as follows. Under a fixed longitudinal dispersivity, the flux terms on the right side of Eq. (2.1) become $\alpha_L q \frac{\partial^2 C_m}{\partial x^2} - q \frac{\partial C_m}{\partial x}$, which have no relation with the mobile/immobile ratio that is mainly related to the partition of mass storage change terms on the left side of Eq. (2.1). The advective transport time scales in Fig. 2.3A (in the range of 40.9 days to 22.5 days) are much longer than the mass transfer time scale between the mobile and immobile domains (around 1.1 days). Therefore, concentrations in the mobile and immobile domains have nearly reached equilibrium, i.e., the rates of mobile and immobile concentration changes with time become nearly the same, which renders the left side of Eq. (2.1) $\theta_m \frac{\partial C_m}{\partial t} + \theta_{im} \frac{\partial C_{im}}{\partial t} \approx (\theta_m + \theta_{im}) \frac{\partial C_m}{\partial t} = 0.9 \frac{\partial C_m}{\partial t}$. This implies that Eq. (2.1) is now essentially insensitive to the mobile/immobile ratio under these conditions. However, one has to be aware that the assumption of a fixed longitudinal dispersivity may not always hold if the mobile/immobile ratio is changing. This is because a change in the mobile/immobile ratio will inevitably change the pore structure and velocity variation which control the longitudinal dispersivity. It suggests that the fixed longitudinal dispersivity assumption under various mobile/immobile ratios can only be regarded as a simplification of actual problems.

In Fig. 2.3B, the BTCs are plotted with a fixed dispersion coefficient but with different mobile/immobile ratios in unilateral flow. In contrast to Fig. 2.3A, one can see that the BTCs are moderately sensitive to the mobile/immobile ratios. Since D_m equals $\alpha_L q / \theta_m$ when neglecting the molecular diffusion, thus a fixed D_m is equivalent to state that longitudinal dispersivity (α_L) is proportional to the mobile water content (θ_m). This is understandable because a greater mobile water content might mean a greater velocity variation in the mobile domain, which leads to a larger longitudinal dispersivity. However, the proportionality of α_L versus θ_m is rather idealized and is better treated as a simplification of actual problems.

It is also interesting to compare the influence of the mobile/immobile ratio on the BTCs in Fig. 2.3B and Figs. 2.4A-2.4B. Fig. 2.3B shows that the solute moves slower under a smaller mobile/immobile ratio in unilateral flow while Figs. 2.4A-2.4B indicate that it travels faster with a smaller mobile/immobile ratio in radial flow. The results of Figs. 2.3B and 2.4A-B shed light on different perspectives of transport in unilateral flow as well as radial flow, and they can be explained as follows. First, from above time scale calculation, one can see that for Fig. 2.3B, the time of advective transport to the point of interest (0.5 m, 0 m) is much longer than the time scale of mobile/immobile mass transfer, thus the mass partition between the mobile and immobile domains has nearly reached equilibrium. Therefore, a smaller mobile/immobile ratio simply means a greater portion of mass stored in the immobile domain and a larger retardation effect over the transport in the mobile domain, which is clearly manifested in Fig. 2.3B. Secondly, quite different from Fig. 2.3B, the time of advective transport to the point of interest (0.5 m, 0 m) in Figs. 2.4A-B is considerably smaller than the mass transfer time scale. In other words, the mass transfer between the mobile and immobile domains has not yet had enough time to reach equilibrium. Therefore, a smaller mobile/immobile ratio means a smaller percentage of mass being transferred to the immobile domain, which results in a greater concentration in the mobile domain, as demonstrated in Figs. 2.4A-B. Furthermore, as the advective transport time for three different mobile/immobile ratios is not much different from each other in radial flow (varying between 1.54 hours to 0.85 hours) in respect to the mass transfer time scale (around 1.1 days), the results for the three θ_m / θ_{im} ratios in Figs. 2.4A-B are clustered quite closely.

Special attention should be paid to Fig. 2.5 for the comparison with Zhu et al. (2016), which essentially ignores longitudinal dispersion in the fracture under the unilateral flow scenario, in addition to assigning identical reaction rates and retardation factors for the fracture and the matrix. Fig. 2.5 clearly shows that a special case of our model without longitudinal dispersion coefficient in the fracture yields the same result as the analytical solution of Zhu et al. (2016). Furthermore, our model with non-zero fracture longitudinal dispersion coefficients produces BTCs that are very different from the BTCs produced from Zhu et al. (2016). This suggests that the fracture longitudinal dispersion has a significant influence on solute transport in a single fracture-matrix system, thus should not be neglected. As seen in Fig. 2.5, a greater fracture longitudinal dispersion allows the contaminant solute to migrate faster in the mobile domain of the fracture.

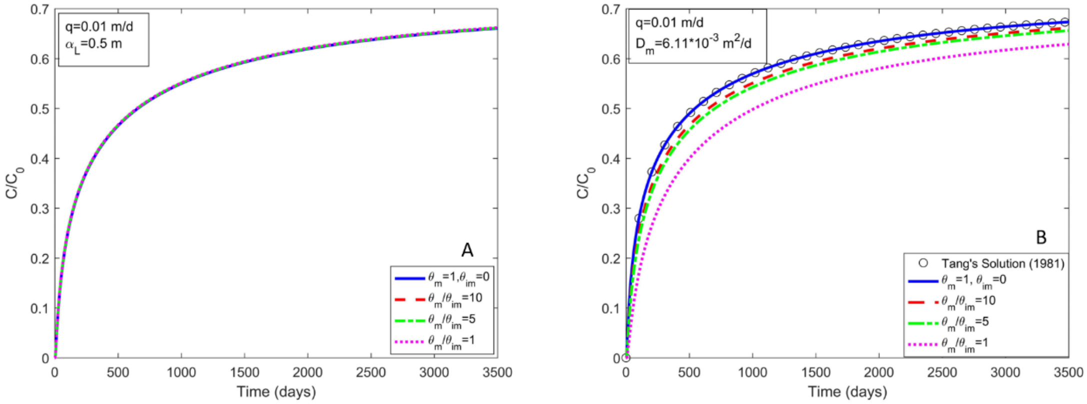

Fig. 2.3A&B BTCs in the mobile domain of the fracture (0.5 m, 0 m) with a fixed Darcian velocity of 0.01m/d in the unilateral flow model (A: fixed dispersivity; B:fixed dispersion coefficient).

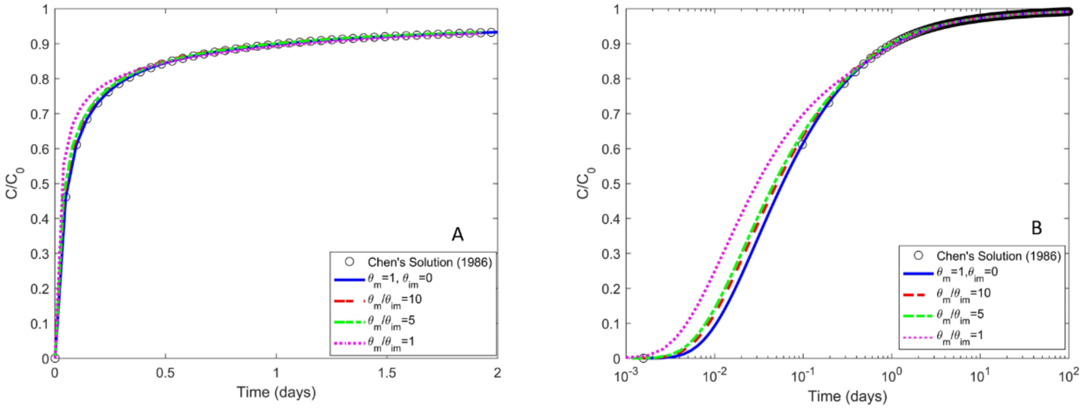

Fig. 2.4A&B BTCs in the mobile domain of the fracture (0.5 m, 0 m) with a fixed radial dispersivity of 0.5 m and mass transfer rate of 0.9 /d in the radial flow model (A. linear scale; B. semi-log scale).

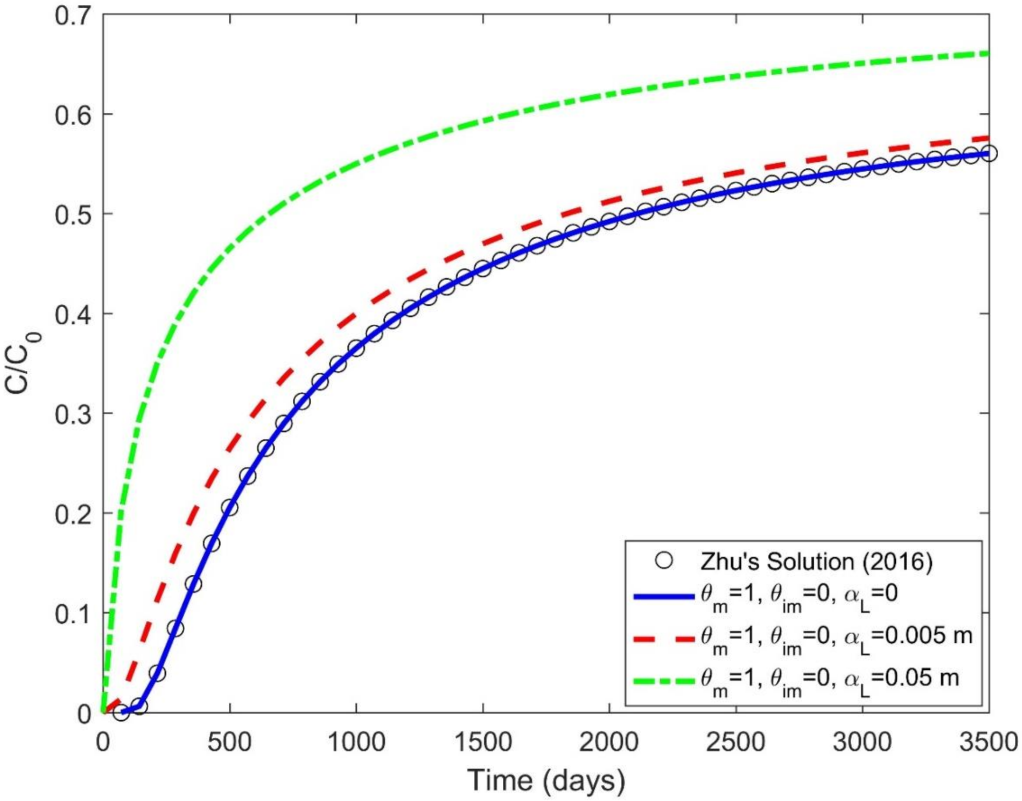

Fig 2.5 BTCs in the mobile domain of the fracture with/without longitudinal dispersivity in the unilateral flow model.

2.4.2 Stored mass calculation

As an important indicator of long-term impacts of solute transport in a fracture-matrix system, solute mass stored in each domain (fracture or matrix) provides very useful information. To understand the solute mass transported and stored in each domain under the unilateral flow scenario, the following equations are given:

$$M'_{fm} = \int_0^{\infty} 2b \times C_m \times \theta_m dx \ , \tag{2.30}$$

$$M'_{fim} = \int_0^{\infty} 2b \times C_{im} \times \theta_{im} dx \ , \tag{2.31}$$

$$M'_k = \int_b^{\infty}\int_0^{\infty} 2 \times C_k \times \theta_k dxdz \ , \tag{2.32}$$

where M'_{fm}, M'_{fim} and M'_k are the mass stored per unit width in the mobile and immobile domains of the fracture and rock matrix, respectively. The actual mass stored in the mobile and immobile domains of the fracture and rock matrix over a width of W can be easily computed as: $M_{fm}=M'_{fm}W$; $M_{fim}=M'_{fim}W$; $M_k=M'_kW$.

Similarly, the mass stored in each domain under the radial flow scenario is given as Eqs. (2.33)-(2.35):

$$M_{fm} = \int_{r_o}^{\infty} 2\pi r \times 2b \times C_m \times \theta_m dr \ , \tag{2.33}$$

$$M_{fim} = \int_{r_o}^{\infty} 2\pi r \times 2b \times C_{im} \times \theta_{im} dr \ , \tag{2.34}$$

$$M_k = \int_b^{\infty}\int_{r_0}^{\infty} 4\pi r \times C_k \times \theta_k drdz \ , \tag{2.35}$$

where M_{fm}, M_{fim} and M_k are the mass stored in the mobile and immobile domains of the fracture and rock matrix, respectively, and 2b in Eqs. (2.30), (2.31), (2.33) and (2.34) is the fracture aperture. Eqs. (2.32) and (2.35) consider the mass stored in the upper and lower rock matrix altogether. The calculation details are included in the supplementary files, and all the mass stored ratio figures are plotted under a fixed dispersivity of 0.5 m.

The following Figs. 2.6-2.8 exhibit different aspects of the stored mass. In particular, Figs. 2.6A-2.6B show the mass stored ratios in the matrix ($M_k / \left(M_{fm} + M_{fim} + M_k\right)$) under different fracture apertures for both models. Figs.

2.7A-2.7B and 2.8A-2.8B are the mass stored ratios in the immobile domain of the fracture ($M_{fim} / \left(M_{fm} + M_{fim} + M_k \right)$) under different mobile/immobile ratios and first-order mass transfer rates for both models, respectively.

Figs. 2.6A-2.6B indicate that the influence of the fracture aperture is similar in both models: the ratio of mass stored in the matrix increases sharply at the beginning, and then approaches an asymptotic limit. A smaller fracture aperture corresponds to a higher ratio of mass stored in the matrix. The observations from Figs. 2.6A-2.6B can be understood as follows. At the beginning of transport, the rock matrix is free of solute, thus there is a significant (or nearly infinite) concentration gradient across the fracture-matrix interface behind the transport front in the fracture, leading to significant diffusive mass transport from the fracture to the rock matrix and a relatively rapid increase of mass in the rock matrix. When time goes longer, such a concentration gradient across the fracture-matrix interface becomes less, resulting in less diffusive mass transport to the matrix, thus a slower rate of increase of mass stored in the matrix. A smaller fracture aperture means a smaller fracture volume, thus a greater ratio of mass stored in the matrix.

In Figs. 2.7A-2.7B, the ratio of mass stored in the immobile domain surges first, after reaching a peak value, it starts to drop slowly and finally approaches an asymptotic limit. The mobile/immobile ratio is a key factor for the mass stored in the immobile domain of the fracture: a higher mobile/immobile ratio results in a lower ratio of mass stored in the immobile domain of the fracture. Those observations are also understandable.

First of all, one can check the characteristic time scales for mobile-immobile mass transfer in the fracture and diffusive transport to the rock matrix. With the use of a mobile-immobile mass transfer rate of $\omega = 0.9\,\mathrm{d}^{-1}$, the characteristic time for mass transfer between the mobile and immobile domains will be $1/\omega = 1.1$ d. Using Eq. (19) in Zhu et al. (2016), one can estimate the solute penetration depth into the rock matrix L to be about 2.7 m, based on D_d of 1.38×10^{-5} m^2/d, a retardation factor of 1, a half-life of 12.34 years, and a four orders of magnitude of concentration reduction in the rock matrix ($\varphi = C_k / C_0 = 0.01\%$). Therefore, the characteristic time for diffusive transport into the rock matrix can be estimated to be $L^2/(2D_d) = 2.6\times10^5$ d. One can easily see that the time scale for diffusive transport to the rock matrix is five orders of magnitude longer than the time scale needed for mass transfer between the mobile and immobile domains of the fracture.

At the beginning of transport, the immobile domain of the fracture is free of solute, thus mass transfer from the mobile domain to the immobile domain in the fracture is rapid, resulting in a quick rise of the ratio of mass stored in the immobile domain, as shown in Figs. 2.7A-2.7B. When time is greater than the characteristic time of mobile-immobile mass transfer (about 1.1 d), mass partition between the mobile and immobile domains of the fracture approaches an equilibrium state, and the ratio of mass stored in the immobile domain will reach a peak value at a time similar to the characteristic time of mobile-immobile mass transfer. This is found to be true. For instance, the times corresponding to three peaks in Fig. 2.7A are 0.41 d, 0.63 d, and 1.24 d, respectively, which are in the same order of magnitude as the characteristic time of mobile-immobile mass transfer of 1.1 d.

Beyond the peak value time, both mobile and immobile domains of the fracture will gradually lose mass due to the diffusive transport to the rock matrix. Such mass loss will result in the decline of the ratio of mass stored in the immobile domain of the fracture. The decline rate of the ratio of mass stored in the immobile domain of the fracture becomes smaller with time because the rate of diffusive transport of mass to the rock matrix drops with time as well. This is evident in Figs. 2.7A-2.7B. In respect to different mobile/immobile ratios, the one with a less mobile/immobile ratio means a greater portion of the immobile domain of the fracture, thus a greater ratio of mass stored in the immobile domain of the fracture as well, which is clearly the case in Figs. 2.7A-2.7B.

Figs. 2.8A-2.8B show the similar patterns of an increasing limb at the beginning, followed by a decreasing limb at the later time for the ratio of mass stored in the immobile domain, as those in Figs. 2.7A-2.7B, with the same reasons explained above. A minor point to note is that much larger time scales are used in Fig. 2.8A (100 d) and Fig. 2.8B (50 d) than those in Figs. 2.7A-2.7B (10 d), thus the plots of Figs. 2.8A-2.8B appear differently from Figs. 2.7A-2.7B. Furthermore, as Figs. 2.8A-2.8B demonstrate, a greater mass transfer rate will lead to significantly greater mass stored in the immobile domain at early time. However, as time increases, mass partition among different domains will reach a nearly equilibrium state, thus the concentration distributions in all domains will remain stable (or at quasi-steady state). Under such a quasi-steady state condition, the mass distributions among different domains are no longer affected by the mass transfer rate, which only plays a role in the transient (or pre-equilibrium) mass transfer processes between the mobile and immobile domains. This is the reason why the curves for different mass transfer rates in Figs. 2.8A-2.8B merge after a sufficiently long time of transport.

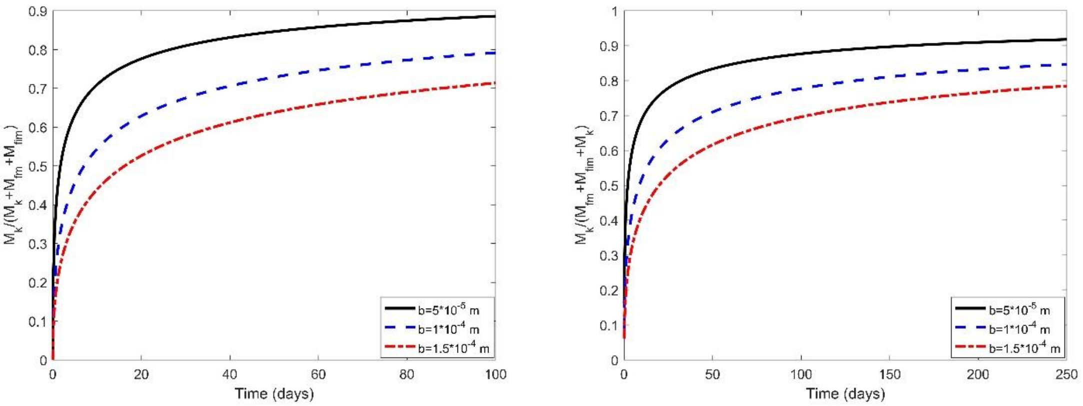

Fig. 2.6A&B The mass stored ratio curves of the rock matrix under different half-apertures of the fracture with a fixed mobile/immobile ratio of 10 and mass transfer rate of 0.9 /d in the unilateral flow model (left, 2.6A) and the radial flow model (right, 2.6B).

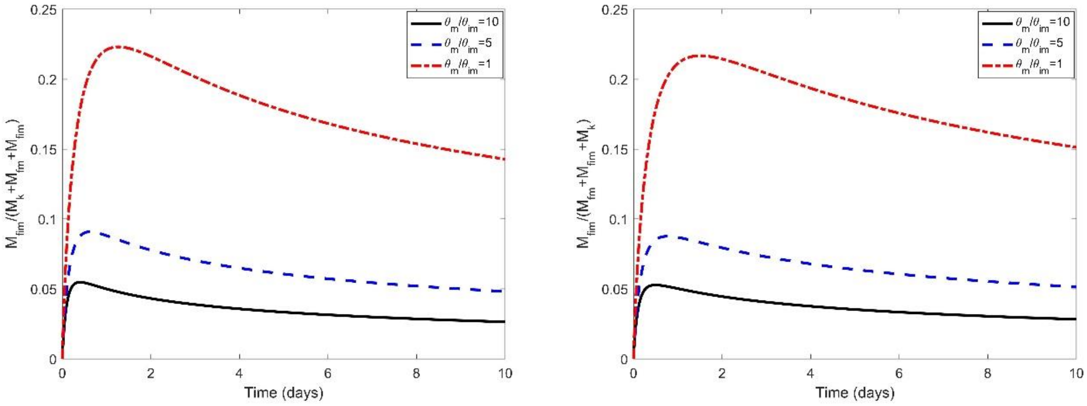

Fig. 2.7A&B The mass stored ratio curves of the immobile domain of the fracture under different mobile/immobile ratios with a fixed half-aperture of 5×10^{-5} m and mass transfer rate of 0.9 /d in the unilateral flow model (left, 2.7A) and the radial flow model (right, 2.7B).

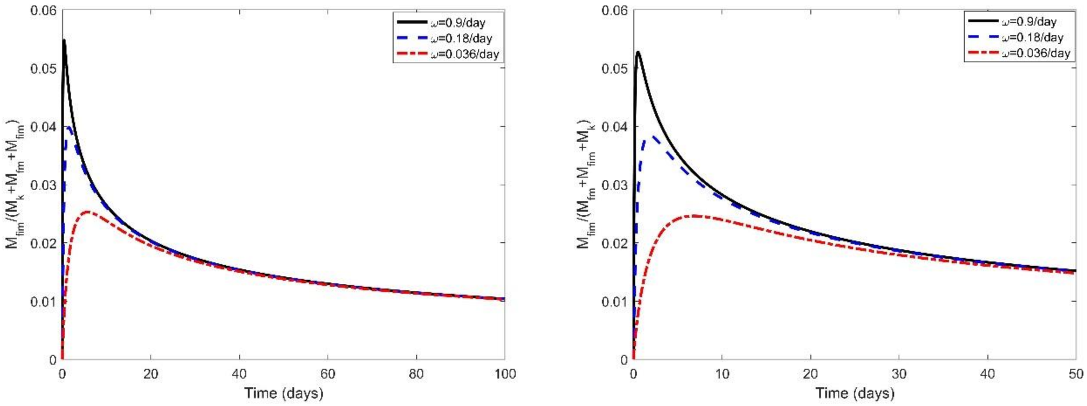

Fig. 2.8A&B The mass stored ratio curves of the immobile domain of the fracture under different mass transfer rates with a fixed half-aperture of 5×10^{-5} m and mobile/immobile ratio of 10 in the unilateral flow model (left, 2.8A) and the radial flow model (right, 2.8B).

2.5 Sensitivity analysis

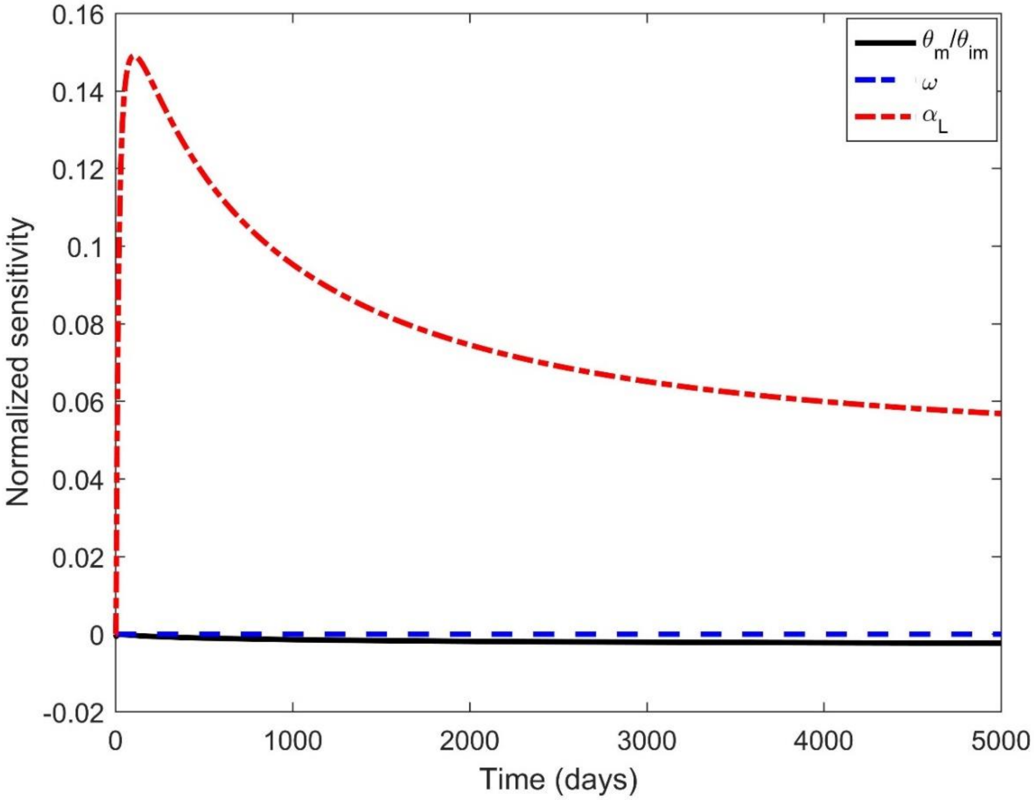

Fig. 2.9 The normalized sensitivity in the mobile domain of the fracture at (0.5 m, 0 m) in the unilateral flow model.

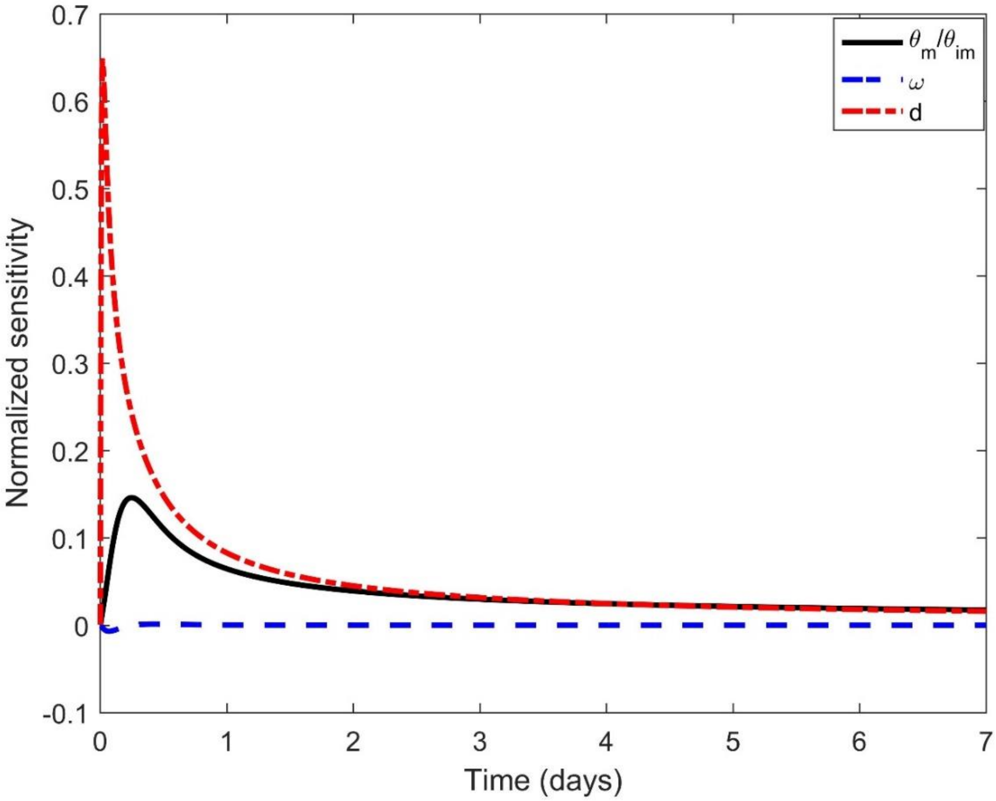

Fig. 2.10 The normalized sensitivity in the mobile domain of the fracture at (0.5 m, 0 m) in the radial flow model.

The normalized sensitivity analysis proposed by Huang and Yeh (2007) and Kabala (2001) is a useful tool to analyze the influence of the input parameters on the output results. The main reason to analyze the sensitivity is to understand the relative impact on the output results due to small increments of the input parameters. Normalized sensitivity coefficients of the mobile-domain concentration in response to the relative changes of the given parameters are expressed as:

$$K_{i,j} = X_j \frac{\partial R_i}{\partial X_j} , \tag{2.36}$$

where $K_{i,j}$ is the normalized coefficient for the j-th input parameter X at the i-th time step. The parameter R is a function of the input parameters X_j and t. The partial derivative in the above equation is approximated by a forward differencing equation as follows:

$$\frac{\partial R_i}{\partial X_j} = \frac{R_i\left(X_j + \Delta X_j\right) - R_i(X_j)}{\Delta X_j} \ , \tag{2.37}$$

where ΔX_j is a small positive increment of the parameter value. In this study, one can assume $\Delta X_j = 10^{-2} \times X_j$.

Several observations can be made from Figs. 2.9 and 2.10. First, as shown in Fig. 2.9 for unilateral flow, the concentration in the mobile domain of the fracture is most sensitive to the longitudinal dispersivity, and nearly insensitive to the first-order mass transfer rate and the mobile/immobile ratio. As shown in Fig. 2.10 for radial flow, the concentration in the mobile domain of the fracture is most sensitive to the radial dispersivity, less sensitive to the mobile/immobile ratio, and least sensitive to the first-order mass transfer rate. Secondly, the normalized sensitivity curves in both models are time dependent: they sharply increase at the beginning; after reaching peak values, they decline with time and eventually approach their equilibrium state. Based on the sensitivity analysis, it is recommended that great effort should be put on determining the dispersivity value for both unilateral and radial flows as the concentration is most sensitive to this parameter.

2.6 Discussion and conclusions

Two different models are proposed to study reactive solute transport in a filled fracture-rock matrix system: one for unilateral flow and one for radial flow. Diffusion to the rock matrix is taken into consideration for both models, in addition to other processes such as radioactive decay, retardation associated with a linear sorption isotherm, advection and longitudinal dispersion. The investigated system involves coupling of transport in three domains: a mobile domain and an immobile domain for characterizing the filled fracture, and a rock matrix domain serves as the solute sink. Both models are solved using a Laplace transform technique. The developed solutions are proven to be robust and accurate and can be used as benchmarks against numerical simulations of transport in a coupled three-domain system involving a filled single fracture-matrix system.

BTCs in unilateral flow are nearly unaffected by the mobile/immobile ratio if the longitudinal dispersivity is fixed and the dispersion coefficient is inversely proportional to the mobile water content (see Fig. 2.3A) while they are moderately affected by the mobile/immobile ratio if the dispersion coefficient is fixed and the longitudinal dispersivity varies proportionally with the mobile water content (see Fig.2.3B).

The comparison of the unilateral flow model of this study with the previous study of Zhu et al. (2016) suggests that the fracture longitudinal dispersion has a significant influence on solute transport in a single fracture-matrix system, thus should not be neglected (see Fig. 2.5).

For both models, the relative masses stored in the immobile domain of the fracture increase first with time to reach maximum values and then slowly decline with time to approach equilibrium, which depends on the mobile/immobile ratios (see Fig. 2.7) but appear to be independent of the first-order mass transfer rates (see Fig. 2.8).

Based on the sensitivity analysis of both models (see Figs. 2.9-2.10), it is recommended that great effort should be put on determining the dispersivity value for both unilateral and radial flows as the concentration is most sensitive to this parameter.

3. REACTIVE SOLUTE TRANSPORT IN AN ASYMMETRICAL FRACTURE-ROCK MATRIX SYSTEM*

3.1 Introduction

The first widely used analytical model of solute transport in a single fracture-rock matrix was proposed by Tang et al. (1981), who compared the solutions with and without the fracture dispersion. This analytical model provided valuable insight into the mechanism of solute transport in a single fracture-rock matrix system. Sudicky and Frind (1982) then extended the solutions of Tang et al. (1981) to a fracture-matrix system with identically parallel fractures. They also concluded that it was necessary to consider the longitudinal dispersion of the fracture in assessing the long-term fate of solute transport. Maloszewski and Zuber (1990) argued that the influence of rock matrix diffusion cannot be negligible and concluded that the matrix diffusion can even be the dominant process in some cases. Bodin et al. (2003) reviewed the laboratory experiments and theoretical studies over last three decades to emphasize the advection, hydrodynamic dispersion, channel effects, matrix diffusion and sorption reactions as fundamental processes which should be integrated together. Roubinet et al. (2012) developed a two-dimensional model for the transport of a conservative solute in a single fracture-rock matrix system. They concluded that the impact of transverse dispersion in the fracture and longitudinal

---

* Reprinted with permission from "Reactive solute transport in an asymmetrical fracture–rock matrix system" by Zhou, R. J., Zhan, H. B. (2018), Advances in Water Resources, 112, 224-234, Copyright [2018] by Elsevier

diffusion in the rock matrix can be neglected in standard models of a single fracture-rock matrix.

All the studies mentioned-above about the fracture-rock matrix system are based on the assumption that the rock matrix has identical transport properties on both sides of the fracture. For a single fracture with parallel and flat surfaces, the problem becomes symmetric in respect to the middle plane of the fracture, thus can be simplified to a half-plane problem (Zhou et al., 2017; Zhu et al., 2016). However, if the rock matrixes on both sides of the fracture have different transport properties such as molecular diffusion coefficient and porosities (Carrera et al., 1998; Xu et al., 2001), they cannot be simplified into a half-plane problem and must be considered as three coupled domains including the fracture and two rock matrixes with different transport properties. For example, the unconformity can be considered as a preferential pathway with high permeability and porosity like a fracture (Zimmerman and Sassen, 1993). The rock formations above and below the unconformity could be formed under very different environments at different ages, thus have different transport properties and should be treated separately. Cipollari and Cosentino (1995) investigated Miocene unconformities in the Central Apennines area. Their field-based observations suggested that the angular unconformity between Middle Miocene and Upper Miocene separated the lower shallow-water limestone, and upper glauconitic arenaceous marls, which was condensed deposition. Thus, the upper and lower layers have significantly different transport parameters and would not be treated as a symmetric case. Also, Caine et al. (1996) proposed that a brittle fault zone was lithological heterogeneity and would act as a conduit for fluid flow and solute transport. The rock blocks on two sides of the fault would have different lithology due to the fault movement. Similar field observations were also reported by Chester and Logan (1986) at Punchbowl fault zone at the juncture of San Gabriel Mountains and the Mojave Desert. The Punchbowl fault zone is located between the Punchbowl Formation and basement with sharp and distinct contacts. The Punchbowl Formation is mainly composed of conglomerate, sandstone, and siltstone. Meanwhile, the basement is primary composed of igneous rocks that are rich of felsic minerals with some thin mafic-mineral layers inside. In summary, the assumption of the symmetric distribution of transport parameters could not stand in above-mentioned examples, and an asymmetric model of the fracture-rock matrix system is required.

It is also important to note that solute transport in an asymmetric fracture-rock matrix system has a broad scope of applications and the results obtained in this study can be applied to dealing with many other mass or heat transport problems in the subsurface. For instance, the system investigated here can be directly applied to solute and/or heat transport in a thin aquifer bounded by two aquitards deposited under different geological times with different sedimentary environments, thus very likely to have very different physical and chemical properties (Zhan et al., 2009a; 2009b). Therefore, one has to use the asymmetric model of this study to deal with such an aquifer-aquitard system. Similarly, solute and/or heat transport in vadose zone-aquifer-underlying materials often time requests an asymmetric model as well. For example, when studying the thermal effect of climate change on groundwater-fed ecosystems in volcanic Medicine Lake highlands in California, USA, Burns et al. (2017) pointed out that an asymmetric heat transport model was inevitable because thermal properties can differ distinctively between the vadose zone, aquifer, and underlying materials.

The main goal of this study is to develop a new analytical model for reactive solute transport in a fracture-rock matrix system with asymmetric distribution of transport parameters of the rock matrix. A finite-element numerical simulation is also developed with COMSOL Multiphysics (COMSOL Inc., Burlington, MA, USA) for the comparison with our solutions. The results under the first-type (constant concentration) and the third-type (constant mass flux) boundary conditions at the fracture inlet are compared. Both tracer flushing and water flushing processes are investigated. With the obtained solutions, one could compute the dynamic partition of mass at three coupled domains, and the matrix diffusion and back-diffusion issues are specifically taken into consideration. The analysis of mass partition would be very helpful for risk and environment impact assessments of contaminant transport in a fracture-matrix system with asymmetric transport properties of rock matrix. The problem can be applied to deal with transport in an unconformity straightforwardly.

3.2 Conceptual model and physical setup

In this study, we consider a thin fracture (or an unconformity) situated horizontally with a constant aperture $2b$. The rock matrixes with different properties are distributed above and below the fracture. Use of a horizontal fracture here is simply for the sake of illustration. In fact, the fracture can be in any orientation as the gravity is not a concern here. The permeability values of the surrounding rock matrixes are several orders of magnitude less than that of the fracture, which is assumed to extend sufficiently far from the domain of interest. The rock matrixes are wide enough in the horizontal direction perpendicularly to the groundwater flow direction in the fracture, thus the problem can be simplified as a two-dimensional one. The matrixes are also assumed to be sufficiently thick, thus the rock matrix boundaries away from the fracture will not affect the transport process and can be regarded as infinitely far.

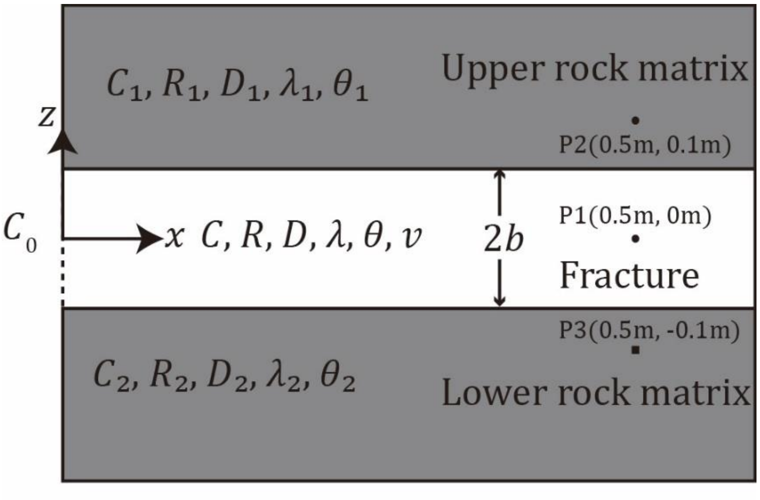

Fig. 3.1 The conceptual model of the single fracture-rock matrix system.

A schematic diagram of three coupled domains including an upper rock matrix, a fracture, and a lower rock matrix is shown in Fig. 3.1. A two-dimensional Cartesian coordinate system is established with the origin at the crossing point of the left boundary and the middle of the fracture (Fig. 3.1). The *x*-axis is from left to right while the *z*-axis is vertically upward. The groundwater flow only occurs in the fracture from left to right and has a constant velocity. Groundwater in the upper and lower rock matrixes is immobile. A contaminant source exists at the origin of the fracture, and the system is free from contamination at the start of transport. Two boundary conditions at $x = 0$ are considered separately: first-type (Dirichlet or constant concentration) and third-type (Robin or constant mass flux) boundary conditions.

Several assumptions about the geometry and transport properties of the system are made as follows. Firstly, the fracture has a very small aperture, which allows the transverse mixing throughout the fracture aperture to occur almost instantaneously. Therefore, the influence of transverse dispersion in the fracture is not taken into consideration. Also, Rezaei et al. (2016) investigated longitudinal dispersion in the rock matrix and concluded that longitudinal dispersion in the rock matrix can be ignored for most practical cases. Secondly, the permeability values of the upper and lower rock matrixes are so small that transport in the rock matrix is dominated by molecular diffusion. These two assumptions provide the basis that the mass flux direction in the rock matrix is perpendicular to the fracture-matrix interface. The following processes are considered: Advection, longitudinal dispersion, molecular diffusion, adsorption and radioactive decay in the fracture; transverse molecular diffusion, adsorption and radioactive decay in the upper and lower rock matrixes.

3.3 Mathematical models and solutions under first-type boundary condition and third-type boundary conditions

Reactive solute transport in the fracture-rock matrix system can be described as the following governing equations:

$$\theta R\frac{\partial C}{\partial t}=\theta\frac{\partial}{\partial x}\left[D\frac{\partial C}{\partial x}\right]-\theta v\frac{\partial C}{\partial x}-\theta\lambda RC-\frac{q_1}{2b}-\frac{q_2}{2b}\ , \tag{3.1}$$

$$R_1\frac{\partial C_1}{\partial t}=D_1\frac{\partial^2 C_1}{\partial z^2}-\lambda_1 R_1 C_1, \tag{3.2}$$

$$R_2 \frac{\partial C_2}{\partial t} = D_2 \frac{\partial^2 C_2}{\partial z^2} - \lambda_2 R_2 C_2 , \tag{3.3}$$

where the subscripts 1 and 2 represent the upper and lower rock matrixes, respectively. The symbol without subscript represents the fracture hereinafter. C [M/L^3] is concentration; b [L] is the fracture's half-aperture; t [T] is the time; R is the constant retardation factor; v [L/T] is the groundwater velocity in the fracture; λ [1/T] is the decay constant which can be further expressed as (ln2)/$t_{1/2}$ where $t_{1/2}$ is the half-life time; θ is the porosity; D [L^2/T] is the longitudinal dispersion coefficient in the fracture, which equals $D = \alpha_L v + D^*$ where α_L [L] is the longitudinal dispersivity, D^* [L^2/T] is the molecular diffusion coefficient in the fracture; D_1 [L^2/T] and D_2 [L^2/T] are the transverse molecular diffusion coefficients in the upper and lower rock matrixes, respectively; q_1 and q_2 [M/L^{2}T] are the diffusive mass fluxes across the fracture-rock matrix interfaces, and can be further expressed as:

$$q_1 = -\theta_1 D_1 \left. \frac{\partial C_1}{\partial z} \right|_{z=b} , \tag{3.4}$$

$$q_2 = \theta_2 D_2 \left. \frac{\partial C_2}{\partial z} \right|_{z=-b} . \tag{3.5}$$

The concentration gradients $\partial C_1 / \partial z$ and $\partial C_2 / \partial z$ at both interfaces are obtained from Eqs. (3.2) and (3.3). A minor point to note is that negative and positive signs are used in Eqs. (3.4) and (3.5), respectively, as positive $\partial C_1 / \partial z$ and $\partial C_2 / \partial z$ will result in downward and upward mass fluxes across the upper and lower fracture-matrix interfaces, respectively.

The existence of possible mass accumulations at the sharp interface between the fracture and rock matrix has been reported in a number of investigations before (Berkowitz et al., 2009; Leij et al., 1991; Marseguerra and Zoia, 2006), which could cause concentration discontinuity across the interface. Such concentration discontinuity is not considered here as this issue is still debatable and has not been widely accepted because of a lack of convincing experimental evidence. Therefore, we assume the concentration continuity at the fracture-matrix interface in this study, as commonly done in numerous previous investigations of flow and transport in a fracture-matrix system (Zhang et al., 2010). Bearing this in mind, above governing equations are supplemented with the following conditions:

$$C_1(x, z = b, t) = C(x, t)\,, \tag{3.6}$$

$$C_2(x, z = -b, t) = C(x, t)\,. \tag{3.7}$$

It is worthwhile to point out that besides the continuity of concentration at the fracture-matrix interface, the continuity of vertical mass flux across the fracture-matrix interface is also honored here. However, the continuity of vertical concentration gradient at the fracture-rock matrix interface is not maintained here because the essence of the governing equations such as Eq. (3.1) is mass balance, not the concentration gradient balance. The continuity of vertical mass flux is done through the use of two flux terms of q_1 and q_2 in Eq. (3.1) above. Since the fracture aperture is usually so small as compared with the scale of transport in the fracture, the mass flux entering the fracture from the matrix is assumed to be uniformly distributed over the entire aperture of $2b$ instantaneously. That is why the terms $q_1/2b$ and $q_2/2b$ are incorporated into Eq. (3.1), instead of being treated as a boundary condition at the fracture-matrix interface. Such an instantaneously-mixed model has been used as a standard approach for numerous studies in flow and transport in fracture-matrix systems (Sudicky and Frind, 1982; Tang et al., 1981) and/or aquifer-aquitard systems (Zhan and Bian, 2006) because it simplifies the governing equation in the fracture and/or aquifer by reducing a two-dimensional problem into a one-dimensional problem. This approach is proven to be robust and sufficiently accurate for fracture-matrix systems owing to the very small apertures as compared to the scales of transport. However, for transport in an aquifer-aquitard system where the aquifer thickness is not sufficiently thin as compared to the scale of transport, the instantaneously-mixed model may be problematic, as documented by some previous investigations (Zhan et al., 2009a; 2009b), because the mass flux into the aquifer from the aquitard cannot be mixed across the entire aquifer thickness quickly. For such a case, one cannot use the above Eq. (3.1) to deal with the transport in the aquifer anymore. Instead, one has to consider both longitudinal and vertical dispersions in the aquifer and specifically honors both the continuities of concentration and vertical mass flux at the aquifer-aquitard interface (Zhan et al., 2009a; 2009b). Nevertheless, the mathematical treatment is much more complex for doing so. Being aware that continuity of mass flux at the aquifer-aquitard interface even for this non-instantaneously-mixed case will not lead to the continuity of vertical concentration gradient at the aquifer-aquitard interface because the vertical hydrodynamic dispersion coefficients in the aquifer and aquitard are usually very different from each other. In summary, regardless of using an instantaneously-mixed model or a non-instantaneously-mixed model, continuities of concentration and mass flux at the fracture-matrix or aquifer-aquitard interface are always maintained, but the continuity of vertical concentration gradient at such an interface is not a concern.

The entire system is assumed to be free of solute at $t = 0$, thus the initial conditions are:

$$C(x,t=0) = C_1(x,z,t=0) = C_2(x,z,t=0) = 0\,. \tag{3.8}$$

The fracture is assumed to be infinitely long, and the rock matrix is infinitely thick, thus one has:

$$C(x \to \infty, t) = C_1(x, z \to \infty, t) = C_2(x, z \to -\infty, t) = 0\,. \tag{3.9}$$

In this study, two different boundary conditions at the fracture inlet are considered separately: the first-type and third-type boundary conditions. For the first-type boundary condition, the concentration at fracture at $x = 0$ keeps constant at C_0:

$$C(x=0,t) = C_0\,. \tag{3.10}$$

The first-type boundary condition assumes that the concentration cross the inlet boundary continuously. Its validity stands if the entrance reservoir is directly connected to the fracture. However, it is not practical for the tracer experiments where the solute is added at a specified rate (Vangenuchten and Parker, 1984).

The third-type boundary condition has also been used frequently, which can be expressed as:

$$\left(vC - D\frac{\partial C}{\partial x} \right)\Bigg|_{x=0^+} = vC_0\,, \tag{3.11}$$

where $x = 0^+$ indicates that the estimation is built for the inside profile of the inlet boundary. The Robin boundary condition stands valid for the following case: the fracture is connected to an entrance contaminant source and the molecular diffusion and dispersion in the fore section ($x < 0$) is ignored (Vangenuchten and Parker, 1984).

The solute convective-dispersive flux component along the *x* direction is given as follow (Batu and Vangenuchten, 1990; Freeze and Cherry, 1979):

$$F_x = \theta v C - \theta D \frac{\partial C}{\partial x}. \tag{3.12}$$

In Fig. 3.2, the convective-dispersive flux components for the first-type and third-type boundary conditions are plotted at $x = 0$. The results clearly indicate that the flux for the first-type boundary condition (F_x) drops over time and approaches steady state at the value of $\theta C_0 v$. However, the convective-dispersive flux for the third-type boundary condition at the inlet boundary keeps constant at $F_x\ /(\theta C_0) = v$ all the time. After a couple of days, both convective-dispersive flux components reach the same value.

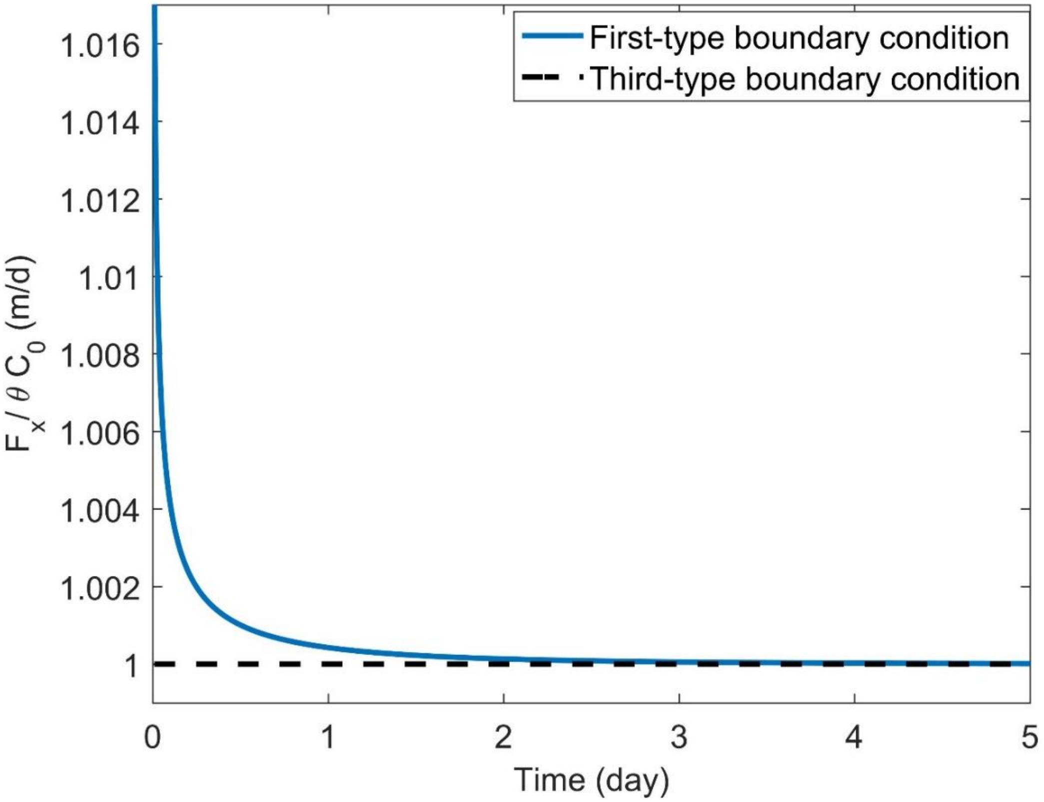

Fig. 3.2 The temporal distribution of $F_x/\theta C_0$ at x = 0 m for the first-type and third-type boundary conditions.

Converting the equations into their dimensionless forms is usually helpful because of fewer independent variables left and more reflective of the systems involved, as some previous studies have demonstrated (Bear, 1972; Simmons et al., 2001). All the definitions of the dimensionless variables are listed in Appendix C of the supplemental files. Besides that, Laplace transform is adopted to transform the problem from real-time domain to Laplace domain for Eqs. (3.1)-(3.11). Thus, the analytical solutions under both boundary conditions can be derived in Laplace domain.

Under the first-type boundary condition, the analytical solutions of the fracture and the upper and lower rock matrixes in Laplace domain are obtained as follows. More details of derivations are provided in Appendix C of the supplementary files.

$$\overline{C_D} = \frac{1}{p}\exp\left(\frac{Pe-\sqrt{Pe^2+4k_1}}{2}x_D\right), \tag{3.13}$$

$$\overline{C_{1D}} = \frac{1}{p}\exp\left[\frac{Pe-\sqrt{Pe^2+4k_1}}{2}x_D - \sqrt{\frac{R_1}{R_2}\left(p+\lambda_1\alpha\right)}\left(z_D - \sqrt{\frac{R_2 D}{RD_1}}\right)\right], \tag{3.14}$$

$$\overline{C_{2D}} = \frac{1}{p}\exp\left[\frac{Pe-\sqrt{Pe^2+4k_1}}{2}x_D + \sqrt{\frac{D_1}{D_2}\left(p+\lambda_2\alpha\right)}\left(z_D + \sqrt{\frac{R_2 D}{RD_1}}\right)\right], \tag{3.15}$$

where the overbar stands for terms in Laplace domain, and the subscript *D* stands for dimensionless terms, *p* is the Laplace transform parameter, *Pe* is Peclet number (see Appendix C of the supplementary files for its definition), and

$$k_1 = \lambda\alpha + p + \frac{\theta_1}{2\theta}\sqrt{\frac{R_1 D_1}{RD}\left(p+\lambda_1\alpha\right)} + \frac{\theta_2}{2\theta}\sqrt{\frac{R_2 D_2}{RD}\left(p+\lambda_2\alpha\right)}.$$

The analytical solutions of the fracture, the upper and lower rock matrixes under the third-type boundary condition in Laplace domain are obtained as follows as well:

$$\overline{C_D} = \frac{1}{p}\times\frac{2}{1+\sqrt{1+4k_1/Pe^2}}\exp\left(\frac{Pe-\sqrt{Pe^2+4k_1}}{2}x_D\right), \tag{3.16}$$

$$\overline{C_{1D}} = \frac{1}{p}\times\frac{2}{1+\sqrt{1+4k_1/Pe^2}}\exp\left[\frac{Pe-\sqrt{Pe^2+4k_1}}{2}x_D - \sqrt{\frac{R_1}{R_2}\left(p+\lambda_1\alpha\right)}\left(z_D - \sqrt{\frac{R_2 D}{RD_1}}\right)\right], \tag{3.17}$$

$$\overline{C_{2D}} = \frac{1}{p} \times \frac{2}{1+\sqrt{1+4k_1/Pe^2}} \exp\left[\frac{Pe - \sqrt{Pe^2+4k_1}}{2} x_D + \sqrt{\frac{D_1}{D_2}\left(p+\lambda_2\alpha\right)}\left(z_D + \sqrt{\frac{R_2 D}{R D_1}} \right) \right].$$

(3.18)

As shown in Eqs.(3.13)-(3.18), the solutions under the third-type boundary condition differ from those under the first-type boundary condition by multiplying a factor of $2/(1+\sqrt{1+\frac{4k_1}{Pe^2}})$. A larger Peclet number (*Pe*) will lead to a smaller difference between those two solutions.

The steady-state solutions are particularly helpful for addressing the long-term estimations. Also, they are usually much simpler than the transient solutions. Thus, the steady-state solutions are widely used for estimating the long-term effect and for designing the remediation plans. To fulfill the requirements of the steady-state solutions, one must meet the following equation:

$$\frac{\partial C_D}{\partial t} = \frac{\partial C_{1D}}{\partial t} = \frac{\partial C_{2D}}{\partial t} = 0. \qquad (3.19)$$

As indicated in Eq. (3.19), after reaching steady state, the concentration in the system would reach equilibrium and no longer change with time. The steady-state solutions can be derived by using the following equation: $f(t_D \to \infty) = \lim_{p\to 0}(pF(p))$, where $F(p)$ refers to the solution in Laplace domain. Thus, the steady-state solutions can be easily derived by calculating the limitations of $p\overline{C_D}$, $p\overline{C_{1D}}$, $p\overline{C_{2D}}$ as p approaches 0 from Eqs. (3.13)-(3.18). The analytical steady-state solutions under the first-type boundary condition are obtained as follows:

$$C_{sD} = \exp\left[\frac{Pe - \sqrt{Pe^2 + 4k_{1s}}}{2} x_D\right], \tag{3.20}$$

$$C_{1sD} = \exp\left[\frac{Pe - \sqrt{Pe^2 + 4k_{1s}}}{2} x_D - \sqrt{\frac{R_1\lambda_1\alpha}{R_2}}\left(z_D - \sqrt{\frac{R_2 D}{RD_1}}\right)\right], \tag{3.21}$$

$$C_{2sD} = \exp\left[\frac{Pe - \sqrt{Pe^2 + 4k_{1s}}}{2} x_D + \sqrt{\frac{D_1\lambda_2\alpha}{D_2}}\left(z_D + \sqrt{\frac{R_2 D}{RD_1}}\right)\right], \tag{3.22}$$

where the subscript *D* implies steady-state dimensionless terms, and

$$k_{1s} = \lambda\alpha + \frac{\theta_1}{2\theta}\sqrt{\frac{R_1 D_1 \lambda_1 \alpha}{RD}} + \frac{\theta_2}{2\theta}\sqrt{\frac{R_2 D_2 \lambda_2 \alpha}{RD}} \ .$$

The analytical steady-state solutions under the third-type boundary condition are as follows:

$$C_{sD} = \frac{2}{1 + \sqrt{1 + 4k_{1s} / Pe^2}} \exp\left(\frac{Pe - \sqrt{Pe^2 + 4k_{1s}}}{2} x_D\right), \tag{3.23}$$

$$C_{1sD} = \frac{2}{1 + \sqrt{1 + 4k_{1s} / Pe^2}} \exp\left[\frac{Pe - \sqrt{Pe^2 + 4k_{1s}}}{2} x_D - \sqrt{\frac{R_1\lambda_1\alpha}{R_2}}\left(z_D - \sqrt{\frac{R_2 D}{RD_1}}\right)\right], \tag{3.24}$$

$$C_{2sD} = \frac{2}{1 + \sqrt{1 + 4k_{1s} / Pe^2}} \exp\left[\frac{Pe - \sqrt{Pe^2 + 4k_{1s}}}{2} x_D + \sqrt{\frac{D_1\lambda_2\alpha}{D_2}}\left(z_D + \sqrt{\frac{R_2 D}{RD_1}}\right)\right]. \tag{3.25}$$

3.4 Results and validations

The transient solutions are now derived analytically in Laplace domain. To obtain the final solutions in real-time domain, the technique of inverse Laplace transform will be applied. Specifically, the method of de Hoog numerical inverse Laplace transform (De Hoog et al., 1982) is selected here for addressing the spatial-temporal concentration distribution, which has been used in other similar studies (Wang and Zhan, 2015; Zhou et al., 2017). This numerical method successfully accelerates the convergence of the Fourier series obtained from the inversion integral using the trapezoidal rule. The results are then tested against the two-dimensional finite element models built by COMSOL Multiphysics and proven to be robust and accurate.

3.4.1 Penetration depth

Estimating the final plume size is useful to evaluate the long-term environment impact and risk assessment. This could be done with the help of analytical steady-state solutions developed above. For a concentration reduction φ or $C/C_0=\varphi$, where φ is much less than 1 (such as 10^{-3} or 10^{-4}), the penetration depth is defined as L_φ for the maximum horizontal penetration depth in the fracture, and $L_{1\varphi}$ and $L_{2\varphi}$ for the maximum vertical penetration depths in the upper and lower rock matrixes, respectively. L_φ refers to the farthest horizontal distance between the origin to the point where the concentration is φC_0, while $L_{1\varphi}$ and $L_{2\varphi}$ demonstrate the farthest vertical distances between the original to the point where the concentration is φC_0 in the upper and lower rock matrixes, respectively. A sufficiently small value of φ refers to the scenario that the concentration has dropped to a negligible level, for instance, $\varphi=10^{-4}$ as used in many studies (Tang et al., 1981). Substituting the definition of φ into Eqs. (3.20)-(3.25), one can obtain the penetration depths L_φ, $L_{1\varphi}$ and $L_{2\varphi}$. For the first-type boundary condition, the penetration depths are:

$$L_\varphi=\frac{2\ln\varphi}{Pe-\sqrt{Pe^2+4k_{1s}}}, \tag{3.26}$$

$$L_{1\varphi} = \sqrt{\frac{R_2 D}{R D_1}} - \ln\varphi \sqrt{\frac{R_2}{R_1 \lambda_1 \alpha}}\ , \tag{3.27}$$

$$L_{2\varphi} = \sqrt{\frac{D_2}{D_1 \lambda_2 \alpha}} \ln\varphi - \sqrt{\frac{R_2 D}{R D_1}}\ . \tag{3.28}$$

The penetration depths L_φ, $L_{1\varphi}$ and $L_{2\varphi}$ for the third-type boundary condition are:

$$L_\varphi = \frac{2\ln\left(\frac{1+\sqrt{1+4k_{1s}/Pe^2}}{2}\varphi\right)}{Pe-\sqrt{Pe^2+4k_{1s}}}\ , \tag{3.29}$$

$$L_{1\varphi} = \sqrt{\frac{R_2 D}{R D_1}} - \frac{\ln\left(\frac{1+\sqrt{1+4k_{1s}/Pe^2}}{2}\varphi\right)}{\sqrt{\frac{R_1\lambda_1\alpha}{R_2}}}\ , \tag{3.30}$$

$$L_{2\varphi} = \frac{\ln\left(\frac{1+\sqrt{1+4k_{1s}/Pe^2}}{2}\varphi\right)}{\sqrt{\frac{D_1\lambda_2\alpha}{D_2}}} - \sqrt{\frac{R_2 D}{R D_1}}\ . \tag{3.31}$$

3.4.2 Breakthrough Curves (BTCs) and concentration distribution analysis

The following values of parameters are used in the example study:

v=1 m/d; b=0.005 m; $\theta_1=\theta_2$=0.01; θ=1; $\lambda=\lambda_1=\lambda_2=1.54\times10^{-4}$ 1/d; $R=R_1=R_2$=1; D=0.5 m^2/d; $D_1=D_2=1.38\times10^{-5}$ m^2/d. It is worthwhile to point out that transport parameters in the upper and lower rock matrixes are given the identical values as a symmetric reference case. After that, we will run the model with asymmetric distribution of diffusion coefficients.

In the finite-element method with COMSOL, a two-dimensional model with a domain of 15 meters wide and 6 meters deep is developed to compare with the semi-analytical solutions of this study. The depth and width of the system is large enough to ignore the effect of limit boundaries during the time periods of interest. Fig. 3.3 shows the segments of mesh used in the numerical simulation. There are 30,928 triangular elements generated in COMSOL, which automatically refines the elements within the fracture and near the interfaces. The maximum and minimum element sizes are 1.01 m and 0.0045 m, respectively. The time step increases linearly with a total simulation time of 500 days.

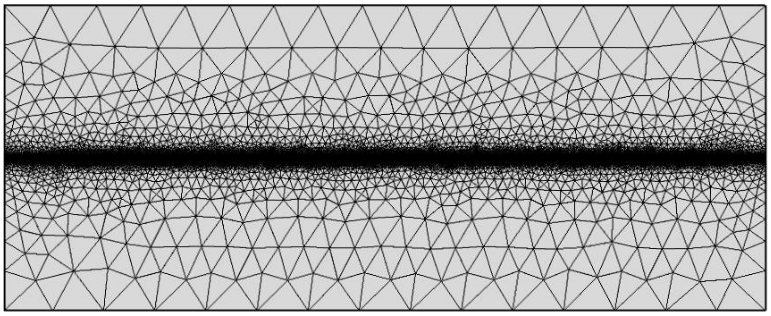

Fig. 3.3 The grid mesh of the fracture-rock matrix system with the finite-element method in COMSOL Multiphysics program.

Without losing generality, three observation points are picked arbitrarily to analyze BTCs of the system (shown in Fig. 3.1): P1 (0.5 m, 0 m) in the fracture, P2 (0.5 m, 0.1 m) in the upper rock matrix and P3 (0.5 m, -0.1 m) in the lower rock matrix, respectively. BTCs at P1 (0.5 m, 0 m) under the first-type and third-type boundary conditions are plotted in Fig. 3.4. The solid lines represent the semi-analytical solutions derived in this study. The dashed lines in the figure represent the numerical solutions of COMSOL. As can be seen, excellent agreements are reached for both boundary conditions between the semi-analytical solutions and finite-element results. It is worthwhile to point out that the difference between solute transport under the first-type and the third-type boundary conditions are obvious at early time. After that, it becomes smaller when approaching steady states. This is primarily because the first-type boundary condition refers to a situation that the solute flux at the inlet boundary decreases with time while the solute flux for the third-type boundary condition remains constant as shown in Fig. 3.2. Since the solute flux for the first-type boundary condition is larger than that for the third-type boundary condition at early time, greater solute mass enters the fracture for this kind of boundary condition, which is clearly indicated in Fig. 3.4. When approaching their steady states, the first-type and the third-type boundary conditions have about the same flux value, leading to nearly the same results after a lapse of enough time.

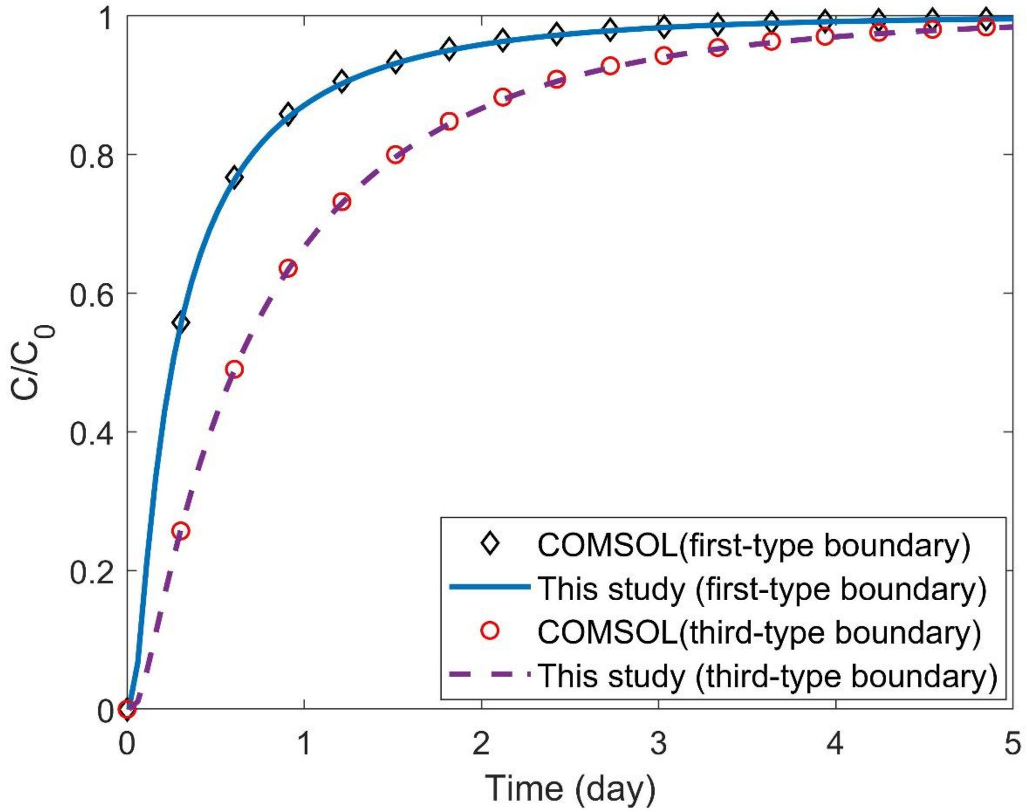

Fig. 3.4 BTCs at P1 (0.5 m, 0 m) comparison between the semi-analytical solutions and numerical solutions under the first-type and third-type boundary conditions.

Fig. 3.5 shows the effects of transverse molecular diffusion coefficients on BTCs. BTCs at P2 (0.5 m, 0.1 m) in the upper rock matrix and P3 (0.5 m, -0.1 m) in the lower rock matrix are plotted as black lines with the same value of transverse molecular diffusion coefficient at 1.38×10^{-5} m^2/d. After relative adjusting the values of transverse molecular diffusion coefficients at $D_1 : D_2 = 10 : 1$ and 50:1 without changing the sum of $D_1 + D_2$, BTCs at P2 (0.5 m, 0.1m) and P3 (0.5 m, -0.1 m) are plotted with blue and red dash lines, respectively. Those two molecular diffusion coefficient ratios are selected arbitrarily to represent the geological media with different transport properties in the upper and lower rock bodies. A lower transverse molecular diffusion coefficient in the upper rock matrix means a lower diffusion term ($D_1 \frac{\partial^2 C_1}{\partial z^2}$) on the right-hand side of Eq.(3.2) and a weaker diffusive effect. Since diffusion is the dominating transport process in the rock matrix, the concentration at P2 (0.5 m, 0.1 m) is less than the concentration at P3 (0.5 m, -0.1 m).

The effects of diffusion coefficient in the rock matrix are further discussed in Fig. 3.6A. BTCs of P3 (0.5 m, -0.1 m) in the lower rock matrix with variable diffusion coefficients in the lower rock matrix are plotted with a fixed value of diffusion coefficient in the upper rock matrix ($D_1 = 1.38 \times 10^{-5}$m^2/d). The values of diffusion coefficients are representatives of some geological media (Golubev and Garibyants, 1971) from relatively unconsolidated sediments to more consolidated sediments. Similar to the results in Fig. 3.5, a lower diffusion coefficient corresponds to a slower diffusive transport process and less concentration in the rock matrix. Fig. 3.6B shows the effects of retardation factor on solute transport in the rock matrix. The retardation factor of the upper rock matrix is fixed at 1 for all cases, which indicates no sorption involved. BTCs at P3 (0.5 m, -0.1 m) in the lower rock matrix under different values of retardation factors are plotted. A greater value of retardation factor in the lower rock matrix means more sorption happened, which will decrease the concentration in the aqueous phase there. Changing the retardation factor in the lower rock matrix will not significantly affect solute transport in the upper rock matrix.

The concentration profiles alone the *z*-axis are indicated in Fig. 3.7. The solid lines in Fig. 3.7 refer to the cases of symmetric distribution of transport parameters for 50 and 500 days, which lead to symmetric distributions of concentration alone the *z*-axis.

With a higher molecular diffusion coefficient in the upper rock matrix, the solute migrates further than that in the lower rock matrix.

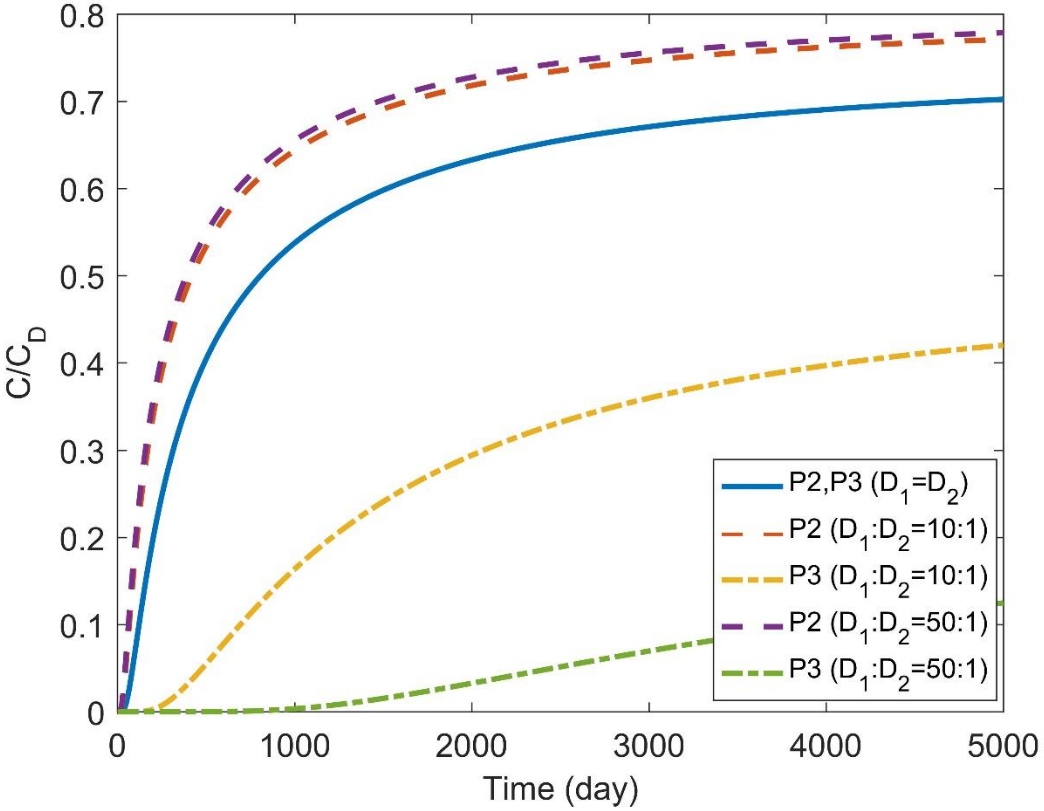

Fig. 3.5 BTCs at P2 (0.5 m, 0.1 m) and P3 (0.5 m, -0.1 m) in the rock matrix with variations of transverse molecular diffusion coefficients under the first-type boundary condition ($D_1 + D_2$= constant).

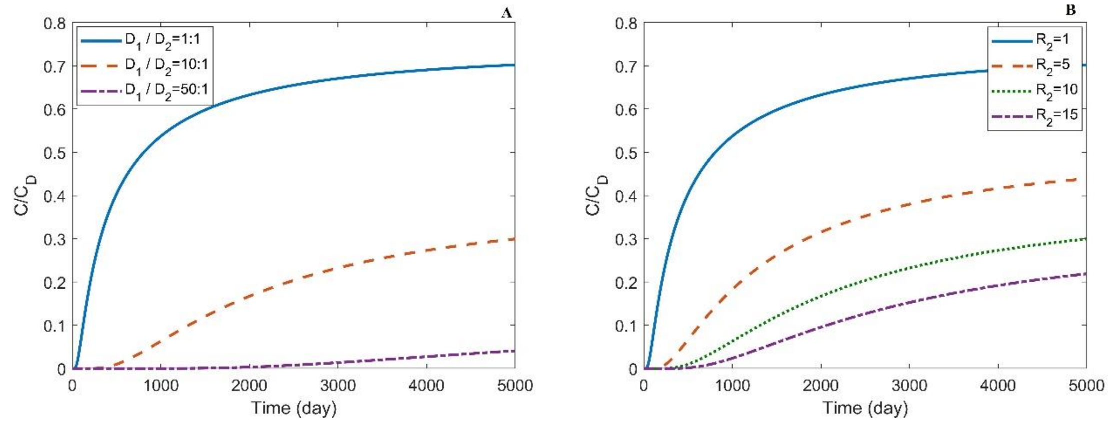

Fig. 3.6A&B BTCs at P3 (0.5 m, -0.1 m) in the lower rock matrix under the first-type boundary condition: A. with variations of molecular diffusion coefficients in the lower rock matrix (D_1=1.38×10^{-5} m^2/d). B. with variations of retardation factors in the lower rock matrix (R_1=1).

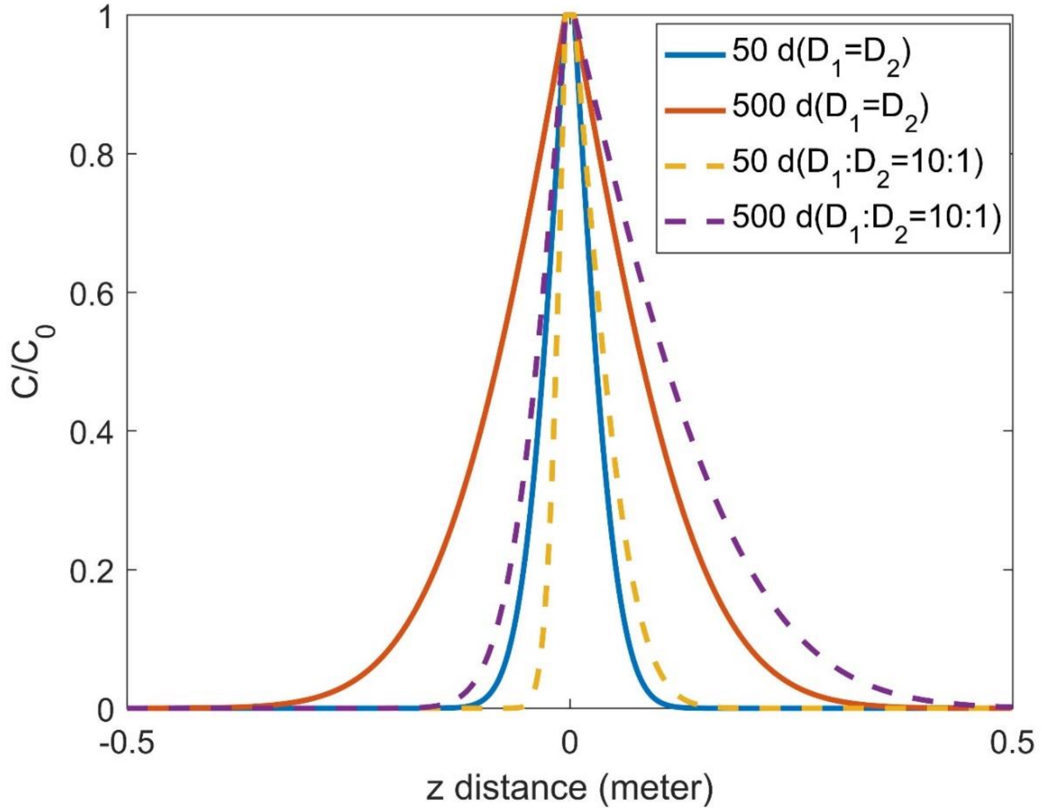

Fig. 3.7 The concentration distribution alone the *z*-axis with symmetric and asymmetric distribution of effective molecular diffusion coefficients.

3.4.3 Back diffusion of mass by water flushing

To study the back diffusion of contaminant mass in the rock matrix, a water flushing phase (with a zero-contaminant mass concentration) is imposed on the inlet boundary of the system after a certain time (t_0) of tracer flushing. The back diffusion from the upper and lower rock matrixes (where concentrations are higher) into the fracture (where concentrations are lower) would occur during the water flushing process. Mathematically, water flushing is done by assuming another contaminant source with a concentration of $-C_0$ at the inlet boundary of the fracture after time t_0 while keeping the original source with a concentration of C_0 undisturbed. We have tested this mathematical approximation rigorously through extensive numerical exercises and conclude that the overall consequence is nearly the same as that of water flushing with some negligible differences at a very short period of time immediately after t_0.

The results of semi-analytical solutions derived in this study at different points are compared with the solutions with the finite-element method in COMSOL for the water flushing phase starts at after t_0 of 2 days (Fig. 3.8). An excellent agreement is reached between these two solutions, confirming the accuracy and robustness of the new solution. The plotted curves in Fig. 3.8 refer to BTCs at the points of (0.5 m, 0 m), (2 m, 0 m), and (4 m, 0 m), respectively. The point (0.5 m, 0 m) is the closest to the inlet boundary, thus experiencing immediate concentration changes after the water flushing. In Fig. 3.8, the advective front of solute just reaches the point (2 m, 0 m) when the water flushing starts. As a result, the concentration at point (2 m, 0 m) still increases with time for a short period even though the tracer flushing has stopped and the water flushing has started. When the water flushing starts, the concentration at point (4 m, 0 m) is still at a relatively low level because this point is still way ahead of the tracer advective front. The peak concentration is observed at about 4 days. Since there is extra time for the mixture of solute and water (or dispersion) before reaching this point, the concentration drops at a slower rate at this point than at other two points.

By comparing BTCs among various locations, several points are notable. Firstly, dilution caused by water flushing will affect the concentration peak value, meaning that the point further down-gradient from the entrance will has a lower peak concentration. Secondly, dispersion (or mixture of solute and water) before reaching the point of interest will slow down the decreasing rate after the peak value. If the point of interest is further away from the entrance, it will take longer time to reach the peak value and decrease slower after that.

Compared to solute transport in the fracture, transport in the rock matrix has a time lag after water flushing. The characteristic time for diffusive transport into the rock matrix is inversely proportional to the effective molecular diffusion coefficient. In Fig. 3.9, the blue solid lines refer to BTCs at points P2 and P3 with identical molecular diffusion coefficient (symmetric case). For the asymmetric case of $D_1 : D_2 = 10 : 1$ and 50:1 while keeping the summation of D_1 and D_2 the same as the symmetric case, the solute reaches point P2 faster than before.

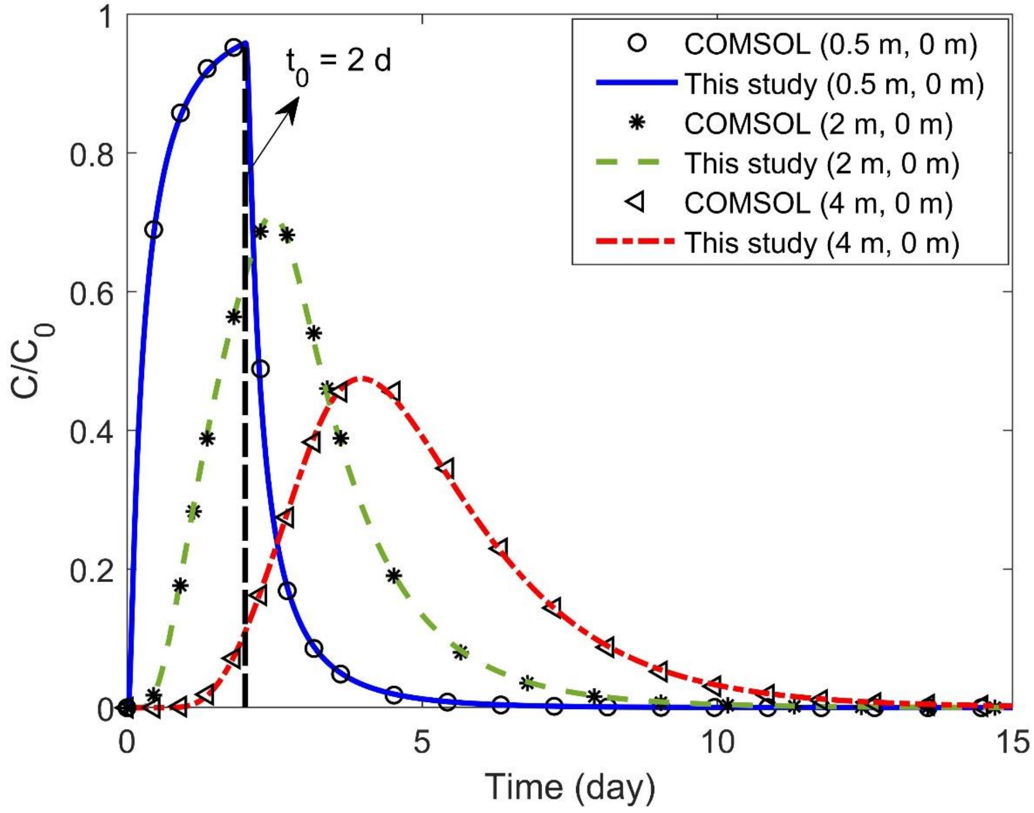

Fig. 3.8 BTCs at points (0.5 m, 0 m), (2 m, 0 m) and (4 m, 0 m) with the semi-analytical solution and finite-element method (water flashing starts at $t_0 = 2$ days).

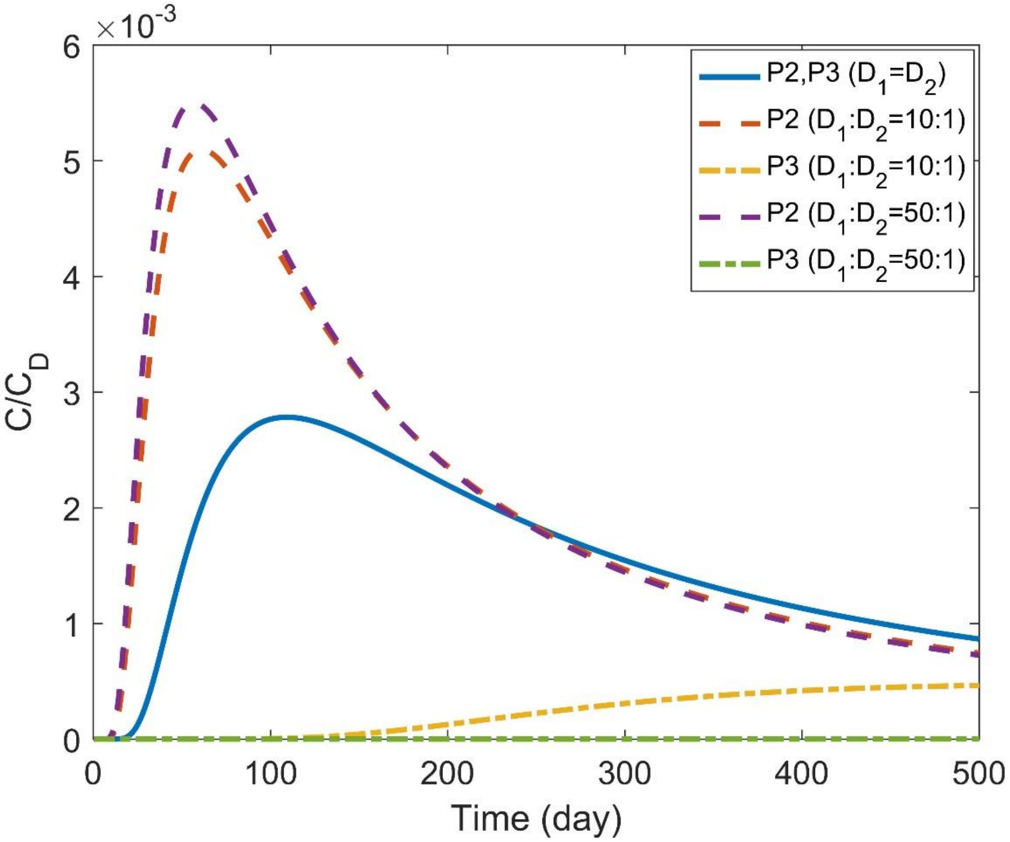

Fig. 3.9 BTCs at P2 (0.5 m, 0.1 m) and P3 (0.5 m, -0.1m) in the upper and lower rock matrixes with the identical and different molecular diffusive coefficients (water flashing starts at t_0 = 2 days).

3.4.4 Diffusive mass exchange between the fracture and matrix

The diffusive mass exchange terms q_1 and q_2 in Eqs. (3.4)-(3.5) refer to the mass fluxes crossing the interfaces of the fracture and the upper and lower rock matrixes, respectively. The influence of asymmetric distribution of transport parameters is investigated in this section. During the tracer flushing phase, mass is diffused from the fracture into the rock matrix while during the water flushing phase, mass is diffused back from the rock matrix into the fracture, except for a very short period of time right after the water flushing.

Fig. 3.10 shows that the diffusive mass exchange between the fracture and the rock matrix have similar patterns and characteristic distances at which the diffusive mass exchange term equals to zero are about the same for all the sceneries of concern. The positive value represents the diffusive mass transport from the fracture toward the rock matrix and vice versa. The diffusive mass exchange term sharply increases and reaches its positive peak value, and then starts to decrease. After water flushing starts, the diffusive exchange term sharply drops to negative and reaches its negative peak value. After that, the back-diffusion rate slowly decreases and approaches zero after a long time. To explain this pattern, one needs to understand that the diffusive mass exchange is directly determined by the concentration gradient crossing the fracture/rock interfaces. A greater concentration difference (or gradient) between the fracture and rock matrix would lead to a greater diffusive mass exchange. In this case, the contaminant solute migrates to 0.5 meters mainly by advection for about 0.5 days, which corresponds to the maximum vertical concentration gradient and the greatest positive diffusive mass exchange at the advection front. With the increasing of solute concentration in the rock matrix, the diffusive mass exchange decreases as the result of declining concentration gradient across the fracture/matrix interface. If water flushing time is sufficiently long, the concentrations of the fracture and the rock matrix would be very close to each other and the solute diffusion between the fracture and rock matrix would be close to zero.

The profile of diffusive mass exchange versus the *x* coordinate is also useful to understand the solute exchange between the fracture and the rock matrix during the water flushing process. In Fig. 3.11, the curves of the diffusive mass exchange along the *x*-axis toward the upper matrix under different time are plotted. It is interesting to check the characteristic distance which is the location at which the concentration in the fracture equals to that in the rock matrix, thus the diffusive mass exchange stops. Without consideration of dispersion, the advection front of water flushing is $(t - t_0)$, which is also the characteristic distance for this hypothetical case. There are two factors which would affect the characteristic distance shifting from the advection front of water flushing to a new location: the longitudinal dispersion in the fracture and the transverse diffusion in the rock matrix. As the diffusion coefficient is several orders of magnitude smaller than the dispersion coefficient, the dispersion plays a more important role here for the shifting of characteristic distance. Thus, the characteristic distance is not sensitive to the asymmetric distribution of diffusion coefficients. After 10 days, the zero value of diffusive mass exchange occurs at 7.9 meters down gradient from the inlet boundary (*x*=7.9 m), which is very close to the advective front of 8 meters. After 30 days, the zero value of diffusive mass exchange term is about *x*=26 m, which is slightly shorter than the advective front of water flushing at *x*=28 m. At $t = 50$ days, the zero value of diffusive mass exchange is about *x*=44 m, while the advective front of flushing water is at *x*=48 m. From above analysis, one can see that a longer time allows for more dispersion, especially at the contact area, thus results in a shorter characteristic distance (or the location of zero diffusive mass exchange) than those without the consideration of dispersion.

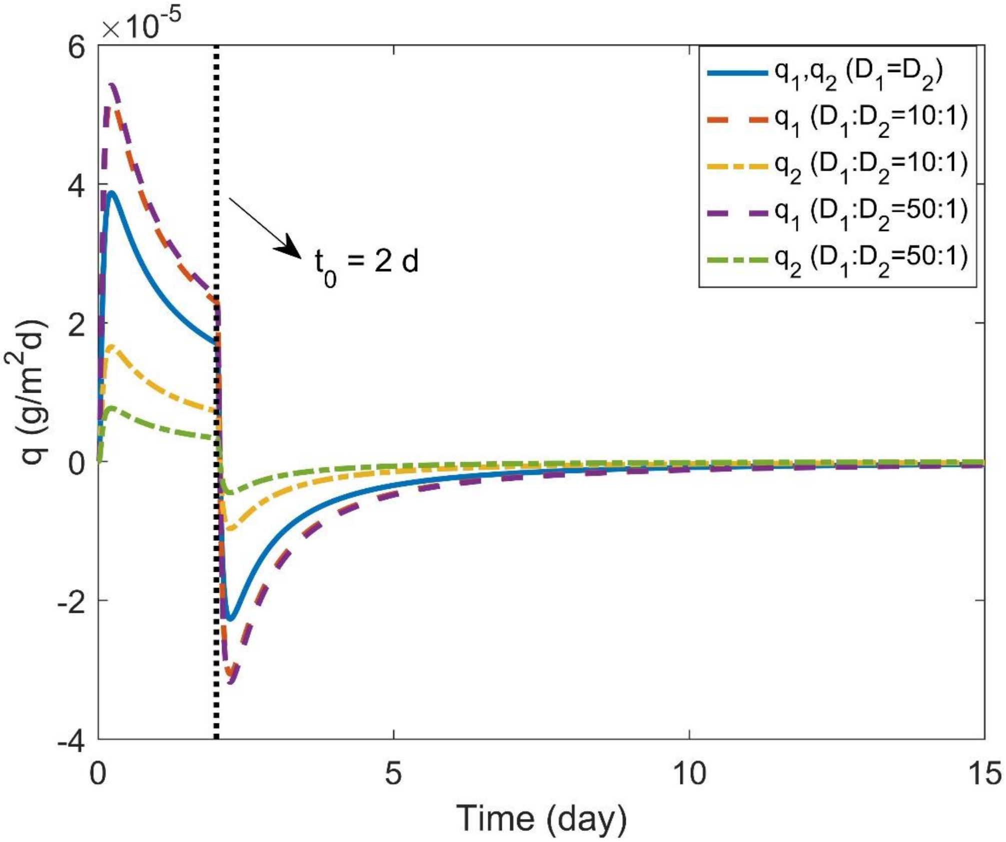

Fig. 3.10 The relationship between q_1, q_2 with the time at x = 0.5 m (water flushing starts at t_0=2 days).

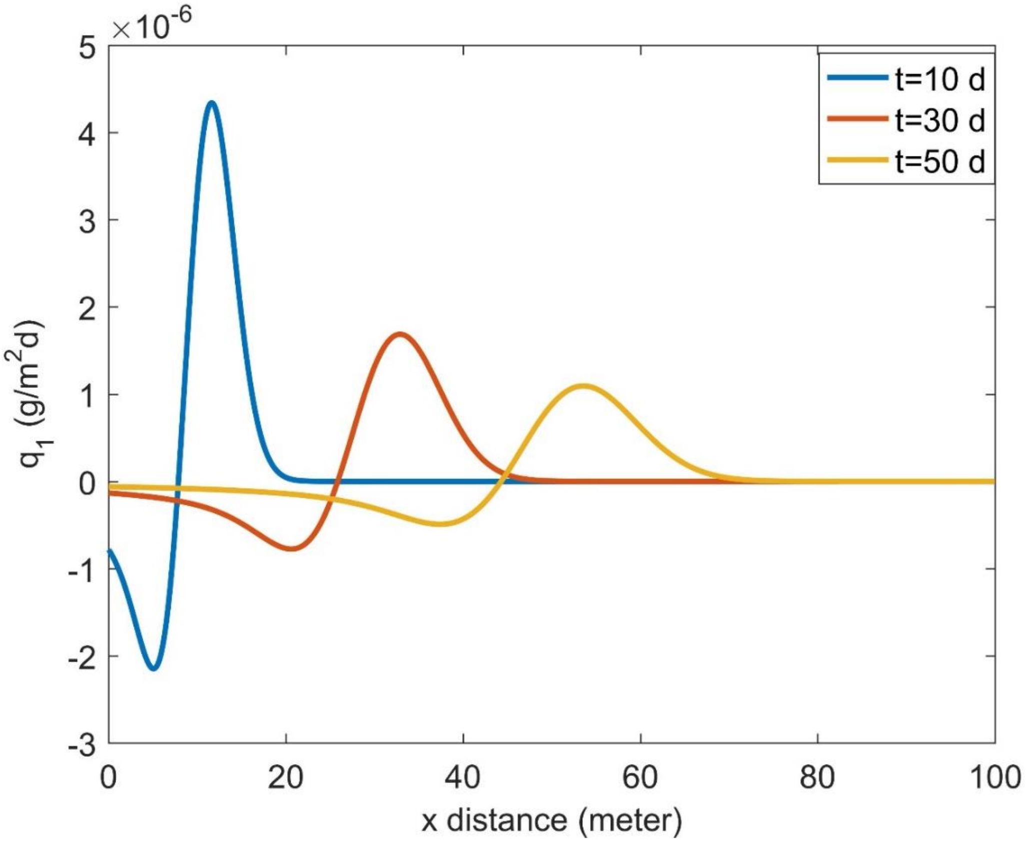

Fig. 3.11 The q_1 distribution alone *x*-axis at various time with symmetric distribution of effective molecular diffusion coefficient (water flushing starts at t_0=2 days).

3.4.5 Mass stored calculation

The amount of mass stored in each domain of the system provides vital information for the long-term influence of solute transport. The following equations are used to calculate the mass stored in each domain:

$$M = \int_0^\infty 2b \times C \times \theta dx, \tag{3.32}$$

$$M_1 = \int_b^\infty \int_0^\infty C_1 \times \theta_1 dxdz, \tag{3.33}$$

$$M_2 = \int_{-\infty}^{-b} \int_0^\infty C_2 \times \theta_2 dxdz, \tag{3.34}$$

where M, M_1 and M_2 are the masses stored per unit width in the fracture, the upper rock matrix and the lower rock matrix, respectively.

As an example, the calculations of mass stored ratios are under the first-type boundary condition (see Appendix C of supplementary materials for details of calculation), where the mass stored ratios are calculated by dividing the mass stored in each domain over the peak value of mass stored in the entire system, which corresponds to the mass stored in the system just before water flushing. In Fig. 3.12, the curves of the mass stored ratios in the fracture and the rock matrix are plotted for the cases of symmetric versus asymmetric diffusion coefficients. Both cases indicate a similar pattern: the mass stored in the fracture is the major part of the total mass and it is more sensitive to water flushing. After 2 days, the mass stored in the fracture decreases sharply. However, the mass stored in the rock matrix continues to increase but at a slower rate even after the stop of tracer flushing or start of water flushing. The mass stored in the fracture is only slightly affected by the diffusion coefficient of the rock matrix, as can be seen from comparing Fig. 3.12A (symmetric case) and Fig. 3.12B (asymmetric case). With a greater diffusion coefficient, the upper rock matrix is able to store more mass, and the difference between the masses stored in the upper and lower rock matrixes becomes larger over time.

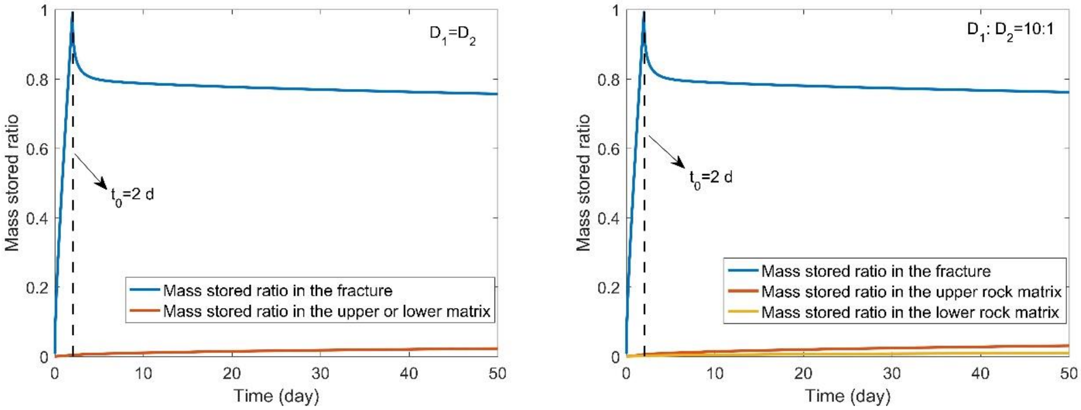

Fig. 3.12A&B Mass stored ratio in the fracture and rock matrixes in the system with symmetric (left: 3.11A) and asymmetric (right: 3.11B) transport parameters.

3.5 Discussion and conclusions

A striking aspect of this study is that it honors the asymmetric nature of diffusion in the upper and lower portions of the rock matrixes. This new advancement over the classical symmetric model makes it possible to deal with transport in fissures separating different rock types or unconformity. However, this study also has its limitations that require further attention. Firstly, in this study, all the parameters are assumed to be independent of scale and time. In reality, the dispersivity or dispersion coefficient could be scale-dependent (Gao et al., 2010; Logan, 1996; Pickens and Grisak, 1981a). The fracture apertures and dispersion can even be time-dependent if the stress-strain condition of the fracture-matrix is a concern. Secondly, this study relies on a presumption that advection-dispersion equation (ADE) is the correct governing equation of transport in the fracture and diffusion equation is the correct governing equation of transport in the matrix. Such governing equations may be subject to debate as some other investigators have adopted different types of approaches such mobile-immobile model

(Zhou et al., 2017), fractional ADE (Benson et al., 2000a; Benson et al., 2000b) or continuous time random walk (CTRW) (Berkowitz and Scher, 1997, 1998) to study transport in the fracture. If flow in the matrix is also a concern, then the diffusion equation of transport in the matrix also must be revised to accommodate the advective transport in the matrix (Rezaei et al., 2016; Zhan et al., 2009a). Thirdly, the study is focused on a single, idealized fracture. It may be extended to multiple paralleled fractures, following the procedures used by Zhu et al. (2016) for symmetric cases. However, if the single fracture has a torturous and irregular trajectory, one may need to either use a totally different approach or to substantially revise the present model of this study. In general, the problem becomes a three-dimensional rather than a two-dimensional for a torturous and irregular fracture. Fourthly, the possible complexity at the fracture-matrix interface is not considered. Such complexity may include the discontinuity of concentration at such an interface, among other factors.

One problem of this study is that there is no direct field data to validate the proposed model, despite the obvious importance of studying asymmetric fracture-rock matrixes and/or aquifer-aquitard systems, as documented by abundant evidences present in the introduction. Lack of experimental studies on the subject may come from a host of reasons. Firstly, it is usually much more difficult to obtain concentration and mass information directly from rock matrixes and/or aquitards, rather than from fractures and aquifers which are much more permeable. In the future, innovative experimental designs have to be devised to measure, preferably non-invasively, concentration and mass in the rock matrixes and/or aquitards. Secondly, for a long time, hydrologists have focused their attention on studying flow and transport in permeable media such as fractures and aquifers, and have tried to avoid less permeable media such as rock matrixes and aquitards. Such a mindset has resulted in much less attention paid to designing instrumentations specifically targeting the rock matrixes and aquitards over many decades. Thirdly, because of the lack of theoretical models on asymmetric systems, models of symmetric systems have been routinely used to interpret data for transport in aquifer-aquitard systems without knowing that whether the systems investigated are truly symmetric or not. It is our hope that the theoretical study of this work may help reinvigorate the interests of experimental study of rock matrixes and aquitards for mass and heat transport in the fracture-matrix and aquifer-aquitard systems.

In summary, general solutions have been developed for reactive solute transport in a fracture-rock matrix system with asymmetric transport properties in the upper and lower rock matrixes. Advection and dispersion along the single fracture, diffusion in the rock matrix and radioactive decay and adsorption in the entire system are considered in this model. The corresponding steady-state solutions and penetration depth are also provided for the long-term evaluation of environment impact. A comparison between the first-type and the third-type boundary conditions are made and explained in terms of solute flux from the entrance source. The following conclusions can be made:

1). The case studies indicate that the asymmetric case would cause a very different solute distribution in the rock matrix as compared to the symmetric case. However, reactive solute transport in the fracture seems to be less affected by the asymmetry of diffusion in the rock matrix (see Figs. 3.5-3.7).

2). During the water flushing phase which occurs sometime later after the tracer flushing, the flushed water significantly dilutes the contaminant in the fracture, leading to a sharp drop of concentration in the fracture. However, the rock matrix responses to water flushing in a much slower fashion. The characteristic time of the peak concentration in the rock matrix is inversely proportional to the effective molecular diffusion coefficient.

3). The patterns of diffusive mass exchange between the fracture and rock matrix are also studies. During the water flushing phase, solute in the fracture is quickly diluted and the back diffusion happens from the rock matrix to the fracture. With more dispersion involved, there would be greater difference between the characteristic distance (with dispersion) and the characteristic distance for the hypothetical case (without dispersion), where the characteristic distance is defined as the distance at which the diffusive mass exchange between the fracture and the rock matrix becomes zero.

The relative amount of mass stored in each domain is studied, and the mass stored in the fracture is the major part of the total mass, which is more sensitive to water flushing. A greater diffusion coefficient in the rock matrix means the ability to store more mass within the same time.

4. REACTIVE SOLUTE TRANSPORT IN A FULLY COUPLED ASYMMETRIC STRATIFIED SYSTEM: COMPARISON OF SCALE DEPENDENT AND INDEPENDENT DISPERSION SCHEMES

4.1 **Introduction**

Since fractures and porous strata such as sand layers are much more permeable than the matrix, they are usually treated as effective conduits in systems for transporting water and solutes (Maloszewski and Zuber, 1993; Sudicky and Frind, 1982). For this reason, the transport problems in the fracture zones or stratified layers could be conceptualized as a similar system: advection and dispersion in the more permeable conduit (fracture or porous layer) and diffusion between more permeable and less permeable domains.

However, all studies above believe that a single value of the dispersivity parameter for an entire porous media is accurate enough to characterize the transport process, which may not be true. Gelhar et al. (1979) analyzed the dispersive process in a stratified heterogeneous porous medium with stochastic techniques. The results showed that the scale-dependent dispersivity problem was associated with the vertical variances of hydraulic conductivity in a horizontally stratified system, confirmed by field-measured hydraulic conductivity profile. In particular, the large values of longitudinal Macrodispersivity were caused by nonuniformities in the hydraulic conductivity profile persisting over long distances. Furthermore, Guven et al. (1984) derived analytical solutions of solute transport in a stratified aquifer with several idealized hydraulic conductivity profiles (parabolic, linear, step function, and cosine profiles), the simulation results indicated that the variation of longitudinal macrodispersivity throughout the transient processes was time-dependent. Gelhar (1986) summarized the stochastic analysis of subsurface flow and transport, considering a heterogenous porous media that can be described by an autocorrelated hydraulic conductivity field, and he further provided a review of field-scale dispersion in aquifers collected from the observations of 59 different field sites and developed a series of classical plots (Gelhar et al., 1992). Now it is generally accepted that the scale-dependent dispersion may prevail over a wide range of scales because of the natural heterogeneities. The data from field tracer tests indicated an overall increasing trend of longitudinal dispersivity (Gelhar et al., 1992; Pickens and Grisak, 1981a, b). The empirical relationships between travel distance and dispersivity have been summarized by Pickens and Grisak (1981a) as linear, exponential, parabolic, and asymptotic functions. These relationships can be directly incorporated into advection-dispersion equation (ADE) for simulation and prediction purpose, and they have been tested by both laboratory and field experiments (Gelhar et al., 1992; Neuman, 1990; Pang and Hunt, 2001; Vanderborght and Vereecken, 2007). On the basis of above mentioned scale-dependent dispersivity functions, many analytical models have been proposed. For example, Yate (1990, 1992) derived analytical solutions for one-dimensional solute transport with linear and exponential functions.

Schulze-Makuch (2005) tested and compared the longitudinal dispersivity data compiled from 109 authors for various types of porous media. He proposed a relationship between longitudinal dispersivity and travel distance using a regression line with the equation for unconsolidated media and stated that this universal scale law could be used to describe transport behavior of any given porous media at any scale. You and Zhan (2013) developed new models for solute transport in a finite column with consideration of dispersivity as both scale-dependent and time-dependent parameters. Gao et al. (2010) incorporated distance-dependent dispersivity into a mobile-immobile model to reinterpret the tracer tests in two 12.5 m long columns, which were documented in detail by Huang et al. (1995). Zech et al. (2015) have revisited the analysis of Gelhar et al. (1992) by carefully reexamining the reliability of the 59 datasets included in Gelhar et al. (1992), and also included the nearly reported tracer test results since Gelhar et al. (1992). Their results indicated that transport in heterogenous porous media was formation-specific, and cannot be relegated by a unique scaling law, as acclaimed by Neuman (1990) and others. Instead, transport requires characterization of aquifer properties such as spatial distribution of hydraulic conductivity, and macrodispersivity of a specific heterogeneous aquifer exhibits its own constant asymptotic value. It is evidence that despite many decades of research, intensive debate still exist on the issue of scale-dependency of transport, as can be seen from the vastly different findings of Zech et al. (2015) and Neuman (1990), Gelhar et al. (1992), and others.

Despite the numerous studies on scale-dependent dispersion, disputes and sometimes counter arguments on the issue of scale-dependency of dispersion are also broadly reported. For instance, Jury et al. (1982) found no apparent increase in dispersivity with depth to 1.8 m in their bromide tracer tests. In a different set of experiments, Butters and Jury (1989) observed that dispersivities at 1.2 m and 1.8 m in depth were even less than that measured at 0.9 m. They also reported that dispersivity at travel distance of 4.5 m was less than those at 0.9 m, 1.8 m and 3.0 m. Porro et al. (1993) did a set of experiments on solute transport through large uniform soil columns. Their results displayed no clear relationship between the dispersivity and scale of the experiments. Bromly et al. (2007) examined the relationship between soil physical parameters, experimental parameters and dispersivity from 291 saturated laboratory column experiments reported in the literature by multiple stepwise regression analysis. Their results indicated that dispersivity was sensitive to the clay content and column diameter. No apparent scale effect of the dispersivity was observed in those tracer tests.

In addition to above mentioned experimental evidences, some theoreticians argued that the so-called scale-dependency of dispersion was merely an artifact of using the Fickian-based local transport theory such as ADE (Morales-Casique et al., 2006). Instead, many transport theories are proposed. The classical dual-porosity modeling for the solute transport in fractured rocks was first proposed by Barenblatt and Zheltov (1960). Van Genuchten and Wierenga (1976) further divided the liquid phase of chemical in the porous media into two phases: mobile and immobile phases. The advection process only happened in the mobile phase. The mass was transferred from mobile region to immobile region by diffusion only, which was proportional to the concentration difference between mobile and immobile phases. Cvetkovic et al. (1999) investigated the reactive tracer transport in a single fracture by developing a Lagrangian probabilistic model. In their model, the advection and diffusion transport processes were related in a dynamic manner with the assumption of two Lagrangian random variables.

Berkowitz and Scher (1995) pointed out the intrinsic inadequacy of imbedding a time-dependent dispersivity into the conventional ADE function. Instead, Berkowitz et al. (2001) proposed the Continuous Time Random Walk (CTRW) method to analyze the tracer tests and proposed solutions that could be used for a variety of dispersive behaviors for conservative tracer tests.

In this study, we will examine whether dispersion in the permeable layer is scale-dependent or not, using a newly reported tracer test data set in a 4-m long box as reported by Swami et al. (2014) and Swami et al. (2016). Furthermore, we will examine whether the molecular diffusions into the less permeable layers are independent of time or not over the time scale of transport. As far as we know, such issues have never been explored for transport in an asymmetric stratified system before.

4.2 Mathematical models and solutions

Similar to the model in Chapter 3, reactive solute transport in the fracture-matrix system can be characterized by Eqs. (3.1)-(3.3). The model is governed by the same initial and boundary conditions as Eqs. (3.8)-(3.9). The difference here is longitudinal dispersivity (α) in the middle permeable layer is no longer a constant. Dispersion coefficient is a function of dispersivity: $D = \alpha(x)v + D_0$, where $\alpha(x)$ [L] is dispersivity and D_0 [L^2/T] is the molecular dispersion coefficient.

The scale dependency of dispersivity is usually considered as linear or exponential function of travel distance. The linear distance-dependent dispersivity coefficient is:

$$\alpha(x) = kx, \tag{4.1}$$

where k represents the slope of the dispersivity-distance relationship, which is a dimensionless parameter. The exponential distance-dependent dispersivity coefficient is expressed as:

$$\alpha(x) = a(1 - e^{-k_1 x}), \tag{4.2}$$

where a [L] is the asymptotic dispersivity value at infinity, k_1 [1/L] is a constant reflecting the rate of dispersivity approaching its asymptotic value.

The limitation of the linear scale-dependent dispersivity model is obvious, as it assumes that dispersivity will keep increasing with the travel distance without an upper bound. The linear or nonlinear increase of dispersivity with scale without bounds has been proposed in some previous studies such as Wheatcraft and Tyler (1988) and Neuman (1990), particularly in so-called self-similar (fractal) hierarchy heterogeneous systems. The field data collected by Gelhar et al. (1992) and Vanderborght and Vereecken (2007) also indicated the increasing trend of longitudinal dispersivity with observation scale. However, such a simple scale-dependent dispersivity model is probably not likely to hold in some field applications (Pickens and Grisak, 1981a). In contrast to such a scale-dependent model without an upper bound, the dispersivity is likely to increase with scale and eventually reaches an asymptotic value at a sufficiently large scale. This is the rationale of using the exponential scale-dependent dispersivity model.

Similarly, the technique of Laplace transform will be adopted to convert the problem to Laplace domain by removing the time-derivative terms and converting the partial differential equations to ordinary differential equations. Supplementing with the boundary and initial conditions, the analytical solutions under the exponential distance-dependent dispersion coefficients could be derived in Laplace domain. The detailed derivations and definitions of the dimensionless variables are provided in the supplementary document.

For the case with the linear distance-dependent dispersivity, the analytical solutions of solute concentrations in an asymmetric stratified system are derived in Laplace domain as follows:

$$\overline{C} = \xi_1^{\gamma} \frac{1}{p} \frac{C_0}{\left(\sqrt{D_0}\right)^{\gamma} K_{\gamma}(\delta\sqrt{D_0})} K_{\gamma}(\delta\xi_1) , \tag{4.3}$$

$$\overline{C_1} = \xi_1^{\gamma} \frac{1}{p} \frac{C_0}{\left(\sqrt{D_0}\right)^{\gamma} K_{\gamma}(\delta\sqrt{D_0})} K_{\gamma}(\delta\xi_1) \times \exp\left[-\sqrt{\frac{pR_1 + \lambda_1 R_1}{D_1}}(z-b)\right], \tag{4.4}$$

$$\overline{C_2} = \xi_1^{\gamma} \frac{1}{p} \frac{C_0}{\left(\sqrt{D_0}\right)^{\gamma} K_{\gamma}(\delta\sqrt{D_0})} K_{\gamma}(\delta\xi_1) \times \exp\left[\sqrt{\frac{pR_2 + \lambda_2 R_2}{D_2}}(z+b)\right], \tag{4.5}$$

where $\xi_1 = \sqrt{kvx + D_0}$, $\gamma = \frac{1}{k}$, $\delta = \frac{2}{kv}\sqrt{\Psi}$,

$\Psi = pR + \lambda R + \frac{\theta_1}{2b\theta}\sqrt{(p+\lambda_1)R_1 D_1} + \frac{\theta_2}{2b\theta}\sqrt{(p+\lambda_2)R_2 D_2}$, $K_{\gamma}(x)$ is the second kind of modified Bessel functions with the order γ , p is the Laplace transform parameter, and the over bar implies the term in Laplace domain hereinafter.

For the case with the exponential distance-dependent dispersivity, the analytical solutions of solute concentrations in an asymmetric stratified system are derived in Laplace domain as follows:

$$\overline{C} = \frac{C_0\left(1+\frac{D_0}{av}\right)^m \xi_2^{-m} F\left(m, m+1; m-n+1; \xi_2^{-1}\right)}{pF\left(m, m+1; m-n+1; \left(1+\frac{D_0}{av}\right)^{-1}\right)}, \tag{4.6}$$

$$\overline{C_1} = \frac{C_0\left(1+\frac{D_0}{av}\right)^m \xi_2^{-m} F\left(m, m+1; m-n+1; \xi_2^{-1}\right)}{pF\left(m, m+1; m-n+1; \left(1+\frac{D_0}{av}\right)^{-1}\right)} \times \exp\left[-\sqrt{\frac{pR_1+\lambda_1 R_1}{D_1}}(z-b)\right], \tag{4.7}$$

$$\overline{C_2} = \frac{C_0\left(1+\frac{D_0}{av}\right)^m \xi_2^{-m} F\left(m, m+1; m-n+1; \xi_2^{-1}\right)}{pF\left(m, m+1; m-n+1; \left(1+\frac{D_0}{av}\right)^{-1}\right)} \times \exp\left[\sqrt{\frac{pR_2+\lambda_2 R_2}{D_2}}(z+b)\right], \tag{4.8}$$

Where $\xi_2 = He^{k_1 x}$, $H = 1 + D_0/(av)$, $m = \frac{1}{2ak_1 H}\left[-1+\sqrt{1+\frac{4aH}{v}\psi}\right]$,

$n = \frac{1}{2ak_1 H}\left[-1-\sqrt{1+\frac{4aH}{v}\psi}\right]$, $F\left(m, m+1; m-n+1; \xi_2^{-1}\right)$ is the Gauss hypergeometric function.

As shown in Eqs.(4.3)-(4.8), the upper and lower less permeable layers are considered separately as they might have different transport properties. All solutions are now successfully derived analytically in Laplace domain. The technique of the numerical inverse Laplace transform is employed to obtain solutions in real-time domain. Specifically, the de Hoog's numerical inverse Laplace algorithm (De Hoog et al., 1982) is used in this study. This algorithm has been widely used in other similar studies to obtain accurate spatiotemporal concentration distributions (Wang and Zhan, 2015; Zhou et al., 2017). It provides better results in accuracy and computational speed than many other methods by accelerating the Fourier series' convergence.

Above solutions are for the phase of injection of a continuous source with a constant concentration at the $x = 0$. If necessary, these solutions can be used to develop the solutions for the phase of leaching when the source is terminated after a finite duration of source injection, T. This is done straightforwardly using the following relationship of $C^L(t) = C^I(t) - C^I(t-T)$, when $t > T$, where C^L and C^I are the concentrations in either the middle, or upper, or lower layer for the leaching phase and injection phase, respectively. In the experiment of Swami et al. (2016), the duration of solute injection T is set to be 2880 minutes. Both solute injection and leaching phases are included in the following analysis in Sections 3 and 4. More detailed discussion about the leaching phase can be found from Zhou and Zhan (2018).

4.3 Validation against previous solutions

The newly derived solutions are then compared to Zhu et al. (2016) and Zhou and Zhan (2018) for validation purpose, which could be regarded as special cases of this study. A closed-form analytical solution for solute transport in the fracture-rock matrix system proposed by Zhu et al. (2016) did not consider dispersive process in the fracture, while the investigation from Zhou and Zhan (2018) about reactive solute transport in an asymmetrical fracture-rock matrix assumes a constant dispersivity in the fracture.

For the case of exponential scale-dependent dispersivity, when the value of k_1 is large enough, $e^{-k_1 x}$ will approach zero even at a small travel distance, which makes the value of dispersion coefficient very close to a constant at $av + D_0$. Therefore, by assuming k_1 at a large value (equals to 1000 /cm in this study), the newly derived solutions should yield the same results of constant dispersivity as the former studies.

We compare the new solution of exponential scale-dependent dispersivity when k_1 = 1000 /cm and a = 0 cm to solution of Zhu et al. (2016). The solution with k_1 = 1000 /cm and a = 38 cm is also compared to solution of Zhou and Zhan (2018) with a constant dispersion coefficient at 4.6 cm^2/min ($av + D_0$). The excellent agreements in Fig. 4.1 for both cases show that the new solutions of this study are robust and reliable, at least for these two special circumstances. One point to note is that BTCs analyzed in the rest paper use the dimensionless concentration (normalized by the source concentration C_0) for the sake of illustration.

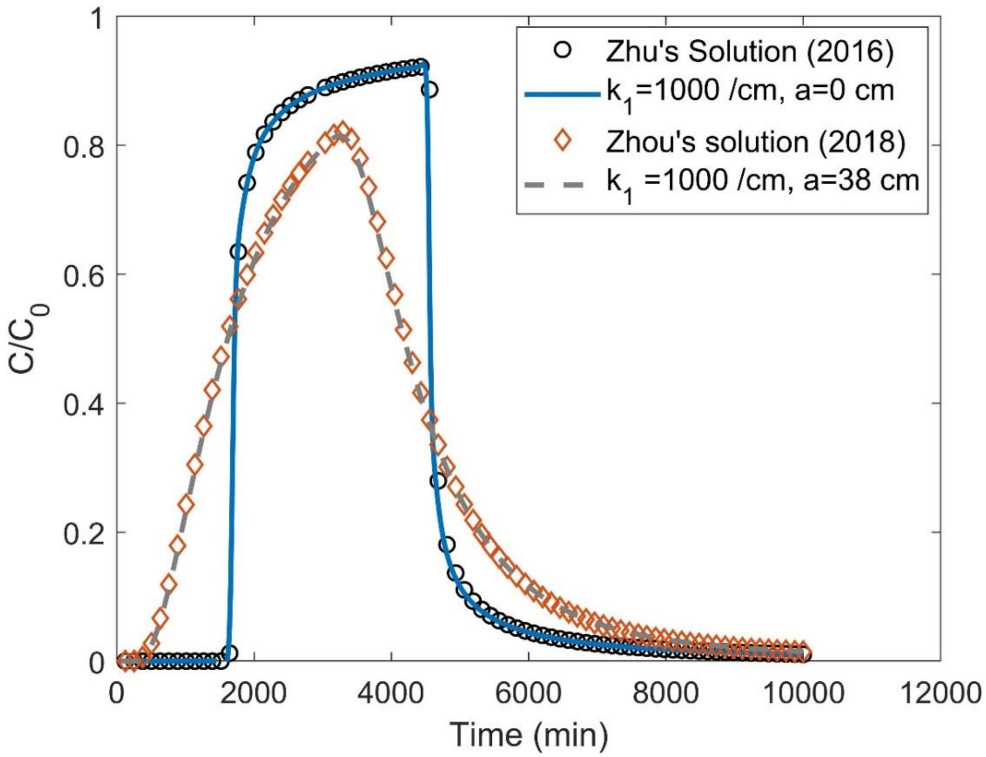

Fig.4.1 BTCs at a travel distance of 200 cm by different methods.

4.4 Result analysis

4.4.1 The diffusive mass exchange between layers and its impact on transport

The mass exchanges between the middle permeable layer and its surrounding less permeable layers could be important mechanisms of retarding the solute transport in the permeable layer. This study builds a fully coupled model of the entire stratified system with the consideration of mass exchanges by diffusive transport among different layers. The simulation results with various values of effective diffusion coefficients and observed results at different travel distances as reported by Swami et al. (2016) are plotted in Figs. 4.2-4.4. When $D_1 = D_2 = 0$, there is no mass exchange among layers, and solute would only migrate within the middle permeable layer. This is a special case and serves as a reference to examine the impact of different diffusions in the upper and lower layers. Since diffusions in the upper and lower layers are the major factors of the mass loss in the middle layer, higher values of diffusion coefficients in those layers will result in lower peak concentration values in the middle layer. During the leaching phase, diffusions in the upper and lower layers are the main factors that control the amount of mass which diffuses back toward the middle permeable layer. Thus, high diffusion coefficients in those layers correspond to higher concentrations in the middle layer in the leaching phase.

As shown in Figs. 4.2-4.4, the effect of diffusions in the upper and lower layers is more obvious in a larger scale of transport, manifested by greater concentration gaps among the cases of different diffusion coefficients. Specifically, the difference of dimensionless peak concentrations between the cases without diffusion and with $D_1 = D_2$

= 5 × 10^{-4} cm^2/min is 0.05 at 50 cm, and such a difference increases to almost 0.4 at 400 cm. All simulated and observed results indicate that the diffusions in the upper and lower layers have significant impact on the concentration distribution in the stratified system, which should not be ignored.

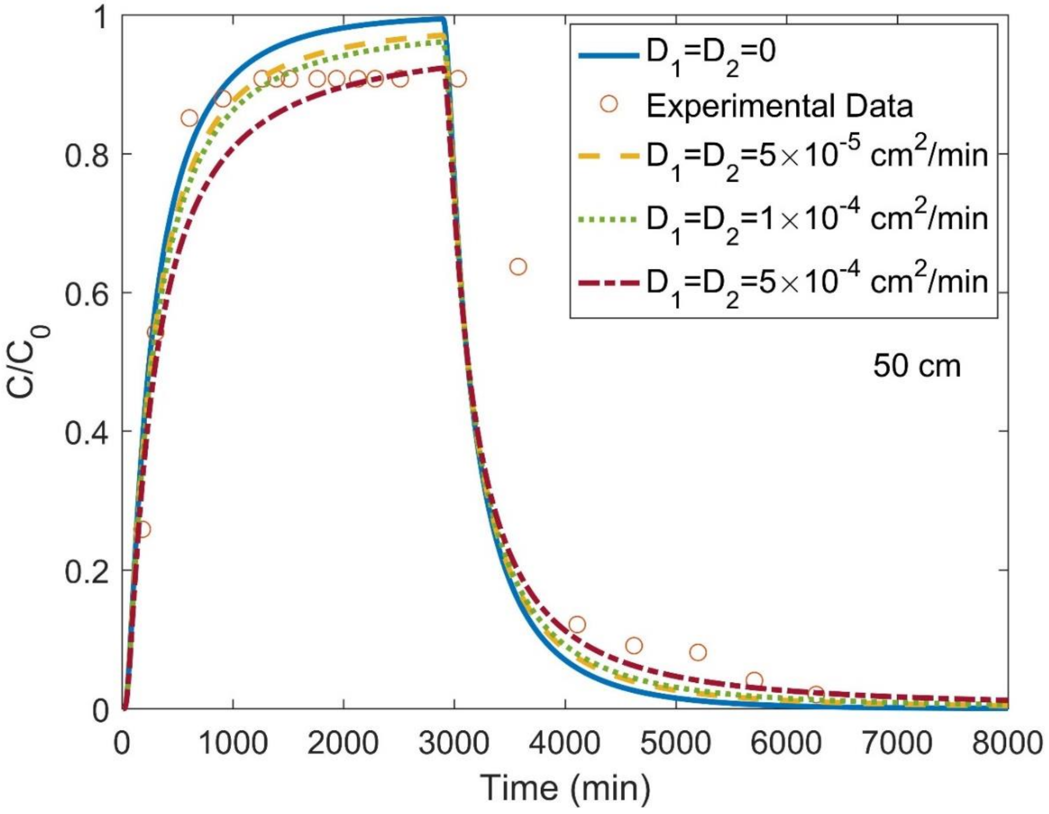

Fig. 4.2 The comparison of the cases with various values of effective diffusion coefficients in less permeable layers at 50 cm.

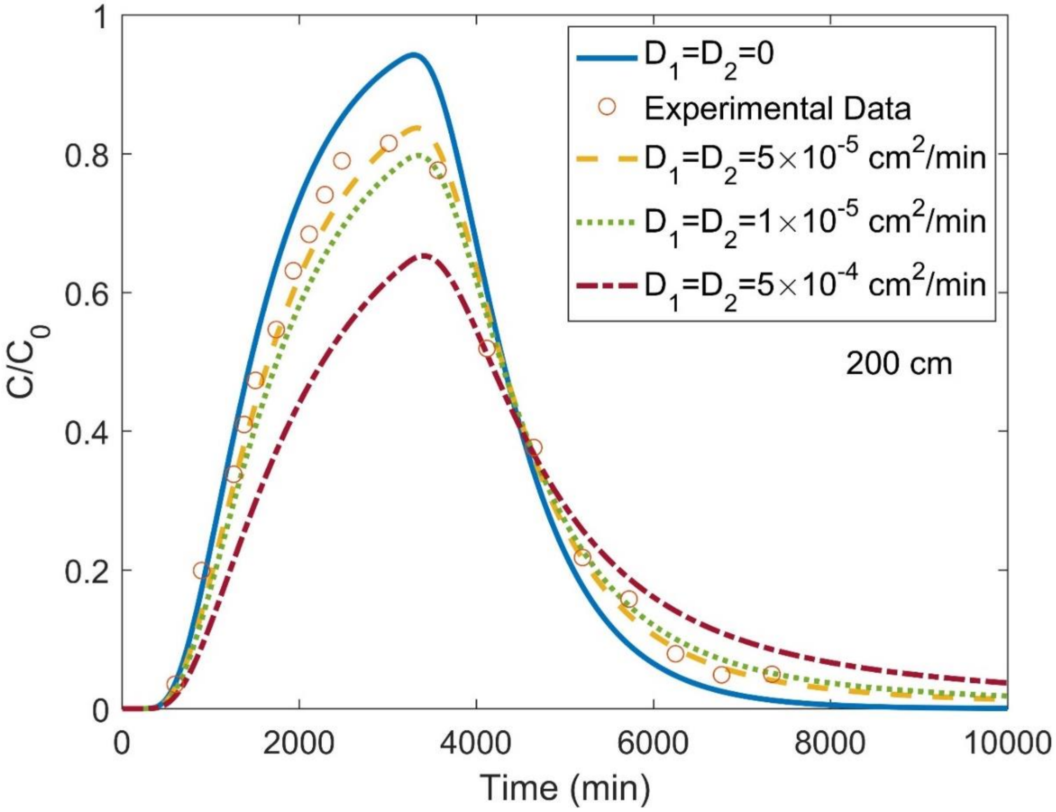

Fig. 4.3 The comparison of the cases with various values of effective diffusion coefficients in less permeable layers at 200 cm.

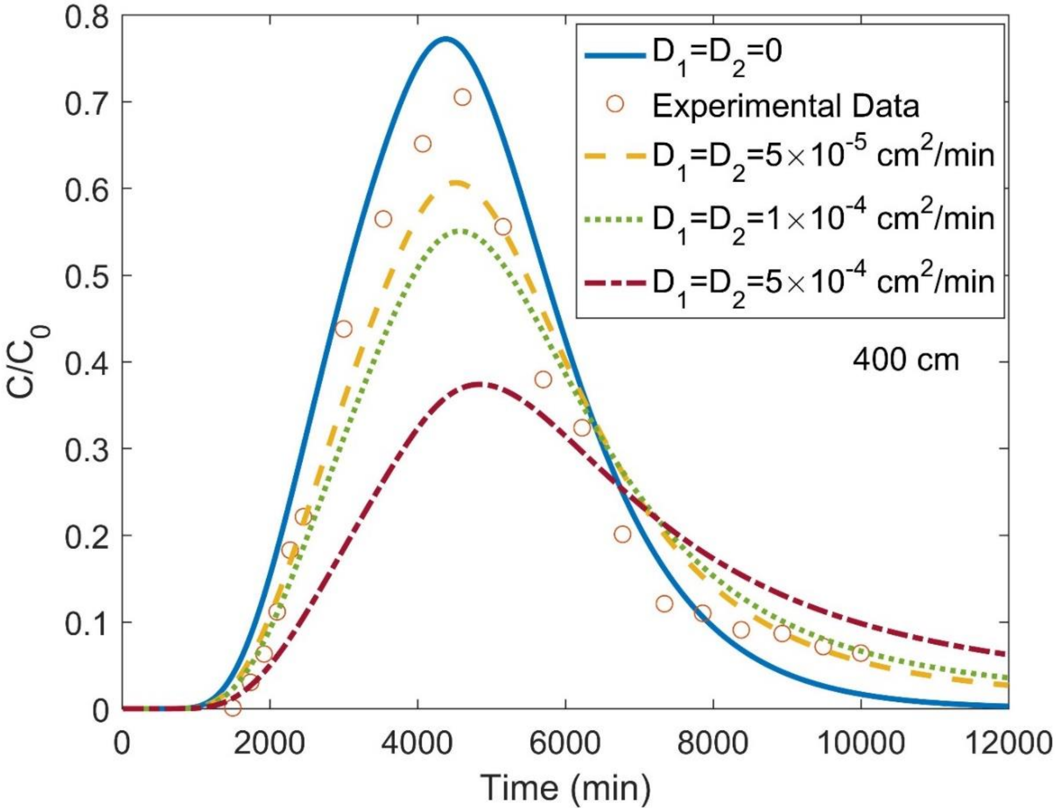

Fig. 4.4 The comparison of the cases with various values of effective diffusion coefficients in less permeable layers at 400 cm.

4.4.2 Impact of scale-dependent dispersivity on transport

In this section, we will examine the impact of scale-dependent dispersivity on transport. The linear function of scale-dependent dispersivity uses a constant coefficient *k* to characterize the increasing rate of dispersivity with travel distance. A larger value of *k* responds to a larger value of dispersivity. As shown in Fig. 4.5, the concentration distribution will spread out over a wider range with a lower peak value at a larger *k* value. Also, the concentration is higher at a given early time and its peak value arrives earlier with a larger *k* value. This is caused by the greater dispersive process due to a greater value of *k*. The exponential function of scale-dependent dispersivity uses constant coefficients *a* and k_1 to characterize the increasing rate of dispersivity with travel distance. The effects of parameters *a* and k_1 in case of the exponential scale-dependent dispersivity are demonstrated in Figs. 4.6A-4.6B. Increasing *a* and k_1 will lead to greater dispersivities. Similarly, BTCs spread out more widely with lower peak values, and the peaks arrive earlier when *a* and k_1 are greater.

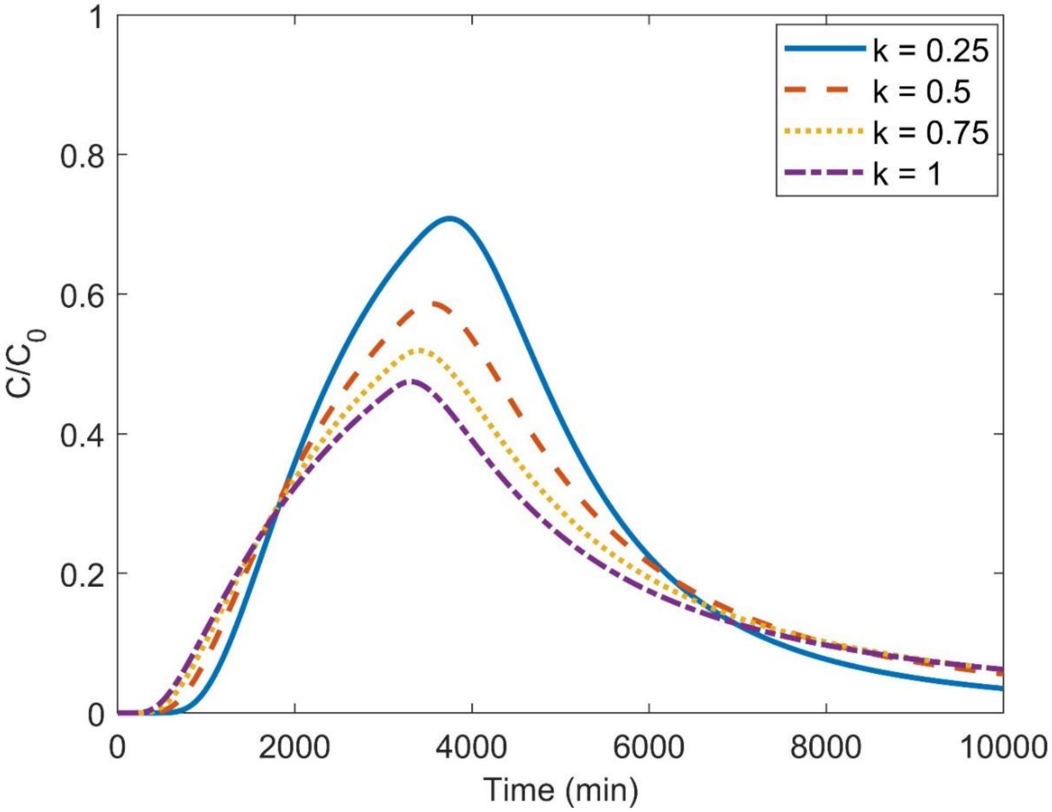

Fig.4.5 BTCs of linear scale-dependent dispersivity with various *k* values at 200 cm.

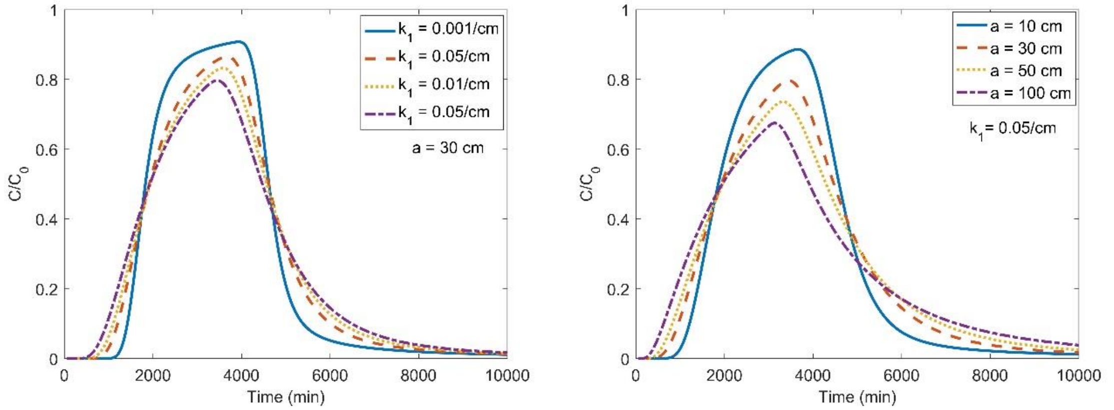

Fig. 4.6A&B BTCs of exponential scale-dependent dispersivity with various k_1 values at 200 cm (a = 30 cm) on the left (4.6A) and with various a values at 200 cm (k_1 = 0.05/cm) on the right (4.6B).

4.4.3 Validate against laboratory tracer test in a stratified system

Swami et al. (2016) conducted a laboratory tracer test for a stratified porous media. Comparing to previous laboratory tracer tests for a stratified system, such as the conservative trace test by Sudicky et al. (1985) and the reactive tracer test by Starr et al. (1985), the scale of test in Swami et al. (2016) is much greater (4 m) than those of Sudicky et al. (1985) and Starr et al. (1985) (1 m). The large scale of test in Swami et al. (2016) makes it particularly suitable for examining the scale-dependent transport theories in which sufficient distance can be encompassed by the solute plume to fully reveal the possible scale-dependency of dispersion, if it truly exists.

In the experimental setup of Swami et al. (2014) and Swami et al. (2016), a thin sand layer is placed in the middle and two thick layers of natural soil are packed as the upper and lower layers. The hydraulic conductivity of natural soil is at an order of 10^{-6} m/day, which is 5 orders of magnitude less than that of sand. A much higher hydraulic conductivity allows easier fluid flow within the sand layer. Therefore, the sand layer is treated as an effective conduit of solute transport in the system while the soil layers are regarded as immobile domains. A chemical source is placed at the inlet boundary of the thin permeable layer. Sampling points at different distances in the sand layer are picked at 50 cm, 200 cm and 400 cm in the direction of flow. The whole experimental system has 4 m in length, and 1 m in width and depth. Each natural soil layer is set to be 48 cm in width, while the middle sand layer is 4 cm in width. The natural soil is obtained from different sites with a mean grain size of 0.055 mm. The fine sand is collected from the upper bank of river Ganga with a mean grain size of 0.75 mm. Both natural soil and sand media are free of any contaminant and well-sorted. The input physical parameters are measured experimentally: the natural soil and sand have porosities of 0.4 and 0.32, respectively. The seepage velocity is 0.121 cm/min.

A solute leaching phase continues after the 2880 min solute injection phase. The effective diffusion coefficients of the upper and lower layers are estimated as 5×10^{-5} cm^2/min by curve-fitting the peaks of the breakthrough curves (BTCs) at the travel distance of 200 cm by the investigators of this study. The theoretical coupled model proposed above is able to address the transport problems with asymmetric distribution of transport parameters. Since the experiments of Swami et al. (2016) used the same material for the upper and lower soil layers, identical values of D_1 and D_2 are adopted in this section. The values of other transport parameters were obtained by Swami et al. (2016) who fitted the observed BTCs of their experiments. The values of the transport parameters are summarized in Table 4-1.

Table 4-1 Values of transport parameters in the tracer test.

Parameter	Symbol	Value
Half-thickness of the permeable layer	b	2 cm
Flow velocity in the permeable layer	v	0.121 cm/min
Porosity in the permeable layer	θ	0.32
Porosity in the upper layer	θ_1	0.4
Porosity in the lower layer	θ_2	0.4
Effective diffusion coefficient of the upper layer	D_1	5×10^{-5} cm^2/min
Effective diffusion coefficient of the lower layer	D_2	5×10^{-5} cm^2/min
Retardation factor of the permeable layer	R	1.2
Retardation factor of the upper layer	R_1	1
Retardation factor of the lower layer	R_2	1
First-order reaction rate constant in the permeable layer	λ	0
First-order reaction rate constant in the upper layer	λ_1	0
First-order reaction rate constant in the lower layer	λ_2	0
Duration of solute injection time	T	2880 min

In this experiment, the stratified system is saturated with water and free of solute at first. After fully saturated, the tracer (fluoride) starts to enter the system through the sand layer only. As a much more permeable layer, the sand layer provides advection and dispersion zones for solute transport in the entire system. As the upper and lower soil layers are treated as immobile domains, the mass exchanges among the middle sand layer and two soil layers are conducted by transverse diffusion. To prevent the influence from direct sunlight, samples are kept in air-tight bottles after labeling and testing. The SPADNS method is used to measure concentrations by a spectrophotometer. The SPADNS method is based on the reaction between fluoride and a zirconium-dye pool, which dissociates a portion of it into a colorless complex anion (ZrF_6^{2-}).

For the simulation, the dispersivity related parameters are calibrated by the best fitting of the root-mean-square-error (RMSE) at 200 cm, and RMSE is expressed as

$RMSE = \sqrt{\frac{1}{N}\sum_{i=1}^{N}(C_{io} - C_{ie})^2}$, where C_{io} and C_{ie} are the observed and estimated dimensionless concentrations from experiment and simulation, respectively. N is the number of observed data points. A smaller value of RMSE represents a better fitting between the theoretical model and the experimental data.

Using the measured BTCs at 200 cm, the value of best fitted constant dispersivity is 35.8 cm, which yields RMSE of 0.0237. The linear scale-dependent dispersivity reaches RMSE of 0.1287 at k = 0.1843. When a = 39.24 cm and k_1 = 1.69 /cm, RMSE of the exponential scale-dependent dispersivity model is 0.0282. Since such a dispersivity value is about one order of magnitude greater than the local dispersivity value of a strictly homogeneous sand layer with similar grain sizes (which is usually around 0.1 to 1 cm), it implies that the sand layer used in the experiments of Swami et al. (2016) is likely to include minor or moderate degrees of heterogeneity. However, such an issue has not been explicitly stated in Swami et al. (2016) .

The best-fitted parameters simulated from BTCs at 200 cm are then used to predict BTCs at an upstream location of 50 cm and a downstream location of 400 cm. Such theoretically calculated BTCs are then tested against the experimentally obtained BTCs at those two locations. The rationale to choose an upstream point and a downstream point is to examine whether the obtained parameter values are robust or not for predicting the concentration at a downstream location and hindcasting the concentration at an upstream location. The results are plotted in Figs. 4.7-4.9, and the corresponding RMSE values are listed in Table 4-2.

As shown in Table 4-2 and Figs. 4.7-4.9, the linear distance-dependent dispersivity model has the worst prediction performance. It tends to shift BTCs to the right and overestimates the dispersive effect. This analysis somewhat disapproves the use of the linear scale-dependent model for the experimental data discussed here. Clearly, RMSE for the constant and exponential scale-dependent dispersivity models are comparable with each other and they are considerably smaller than that of the linear scale-dependent dispersivity model. Meanwhile, Figs. 4.7 and 4.9 indicate that the performances of the constant dispersivity model and the exponential scale-dependent dispersivity model are very similar to each other. The characteristic of exponential dispersion function depends on its constants k_1 and a. There may be non-unique solutions for the similar effective dispersion coefficient, as pointed out by Joshi et al. (2015). This may be one of the reasons why it is difficult to differentiate exponential dispersion and constant dispersion schemes. In summary, the constant dispersivity model, albeit simpler than the exponential scale-dependent dispersivity model, works reasonably well here for best fitting the experimental BTCs.

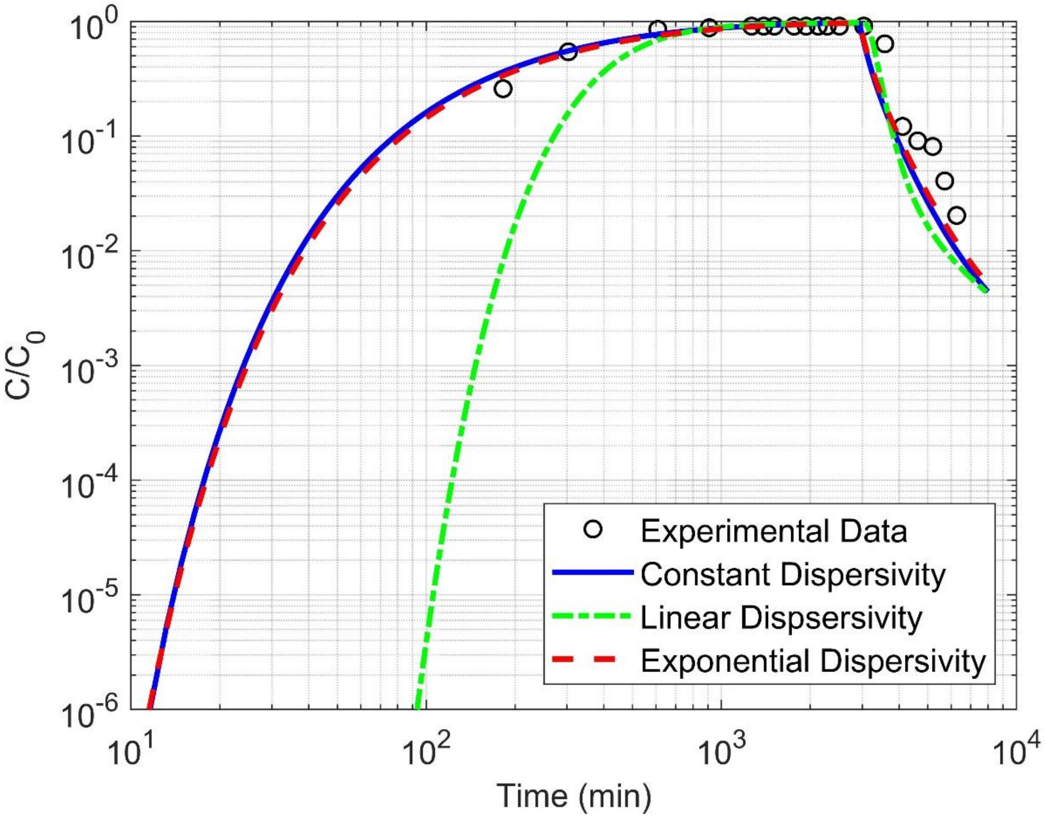

Fig. 4.7 BTCs with constant dispersivity, linear scale-dependent dispersivity, and exponential scale-dependent dispersivity in log-log scale at 50 cm.

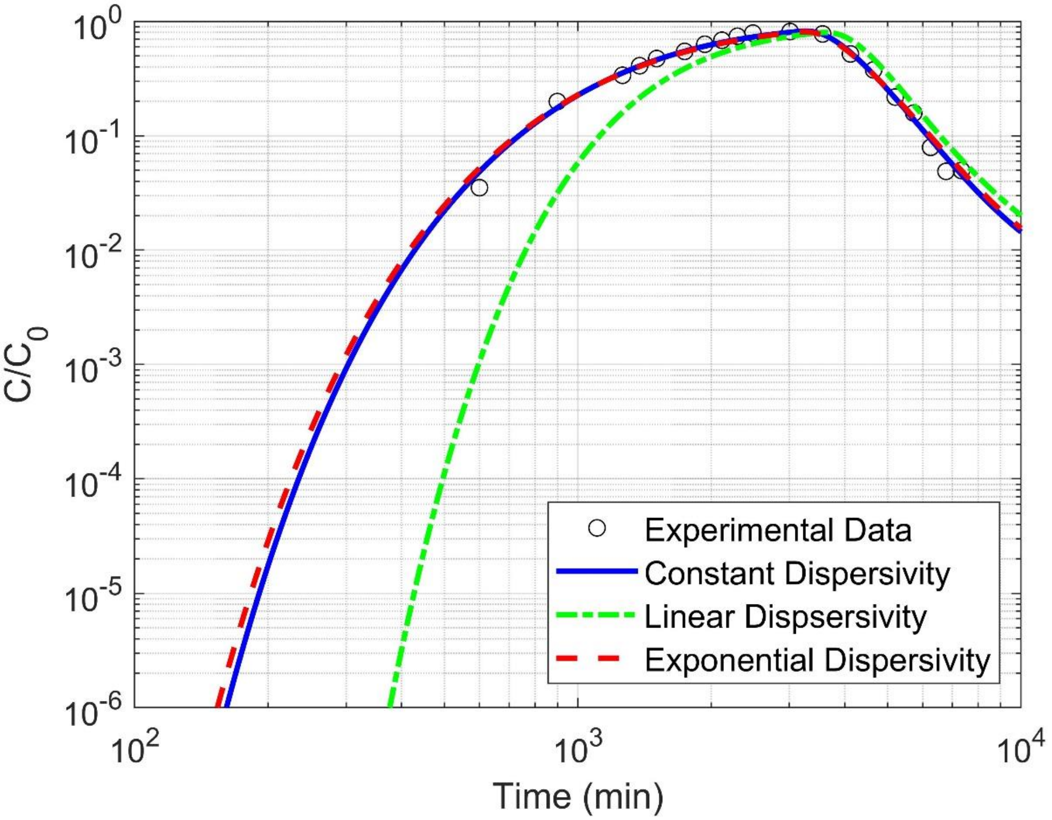

Fig. 4.8 BTCs with constant dispersivity, linear scale-dependent dispersivity, and exponential scale-dependent dispersivity in log-log scale at 200 cm.

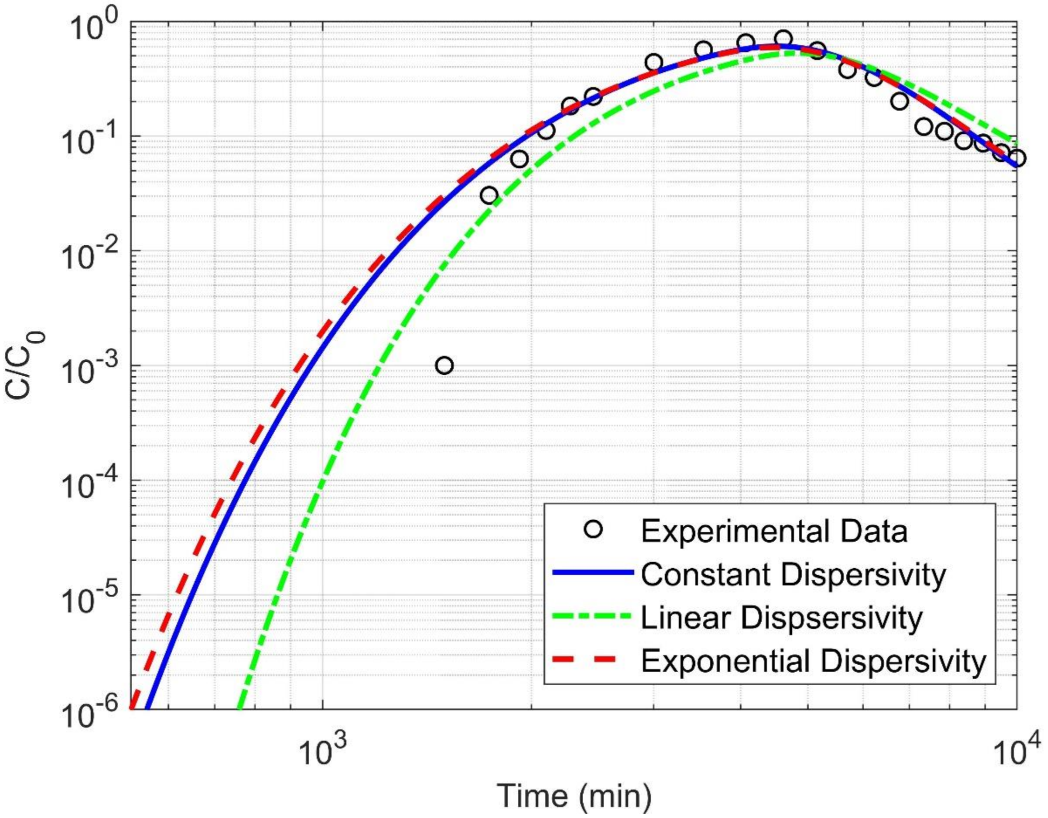

Fig. 4.9 BTCs with constant dispersivity, linear scale-dependent dispersivity, and exponential scale-dependent dispersivity in log-log scale at 400 cm.

Table 4-2 Simulated results at 50 cm, 200 cm and 400 cm.

Sampling distance	50 cm	200 cm	400 cm
Constant dispersivity (*d*=35.8 cm)	RMSE=0.1265	RMSE=0.0237	RMSE=0.0517
Linear scale-dependent dispersivity (*k*=0.1843)	RMSE=0.1547	RMSE=0.1287	RMSE=0.1047
Exponential scale-dependent dispersivity (*a*=39.25 cm, k_1=1.69 /cm)	RMSE=0.1218	RMSE=0.0282	RMSE=0.0542

To further examine the effect of scale-dependent dispersivity in a stratified porous media, the observed BTCs at 50 cm, 200 cm and 400 cm are best fitted individually using the constant dispersivity model, and the results are shown in Fig. 4.10. The best fitting results between the experimental and simulated BTCs demonstrate that the mean values of dispersivity at 50 cm, 200 cm, and 400 cm are 21.5 cm, 38.5 cm, and 35 cm, respectively. One striking feature is that the best fitted dispersivity at 400 cm is slightly less (instead greater) than that at 200 cm with roughly 10% discrepancy. The simulated BTCs at 50 cm and 400 cm perform less satisfactorily as compared against the experimental BTCs in several aspects, as shown in Fig. 4.10. First, the predicted peak concentration at 50 cm is higher than the observed one, while the predicted peak concentration at 400 cm is lower than the observed one. Second, the predicted BTC at 400 cm during the injection phase is lower than the observed BTC, while the predicted BTC at the same location of 400 cm during the leaching phase is higher than the observed BTC.

Based on above observation and analysis, the effect of scale-dependent dispersivity does not appear to be evident in this set of experiments in a stratified porous media.

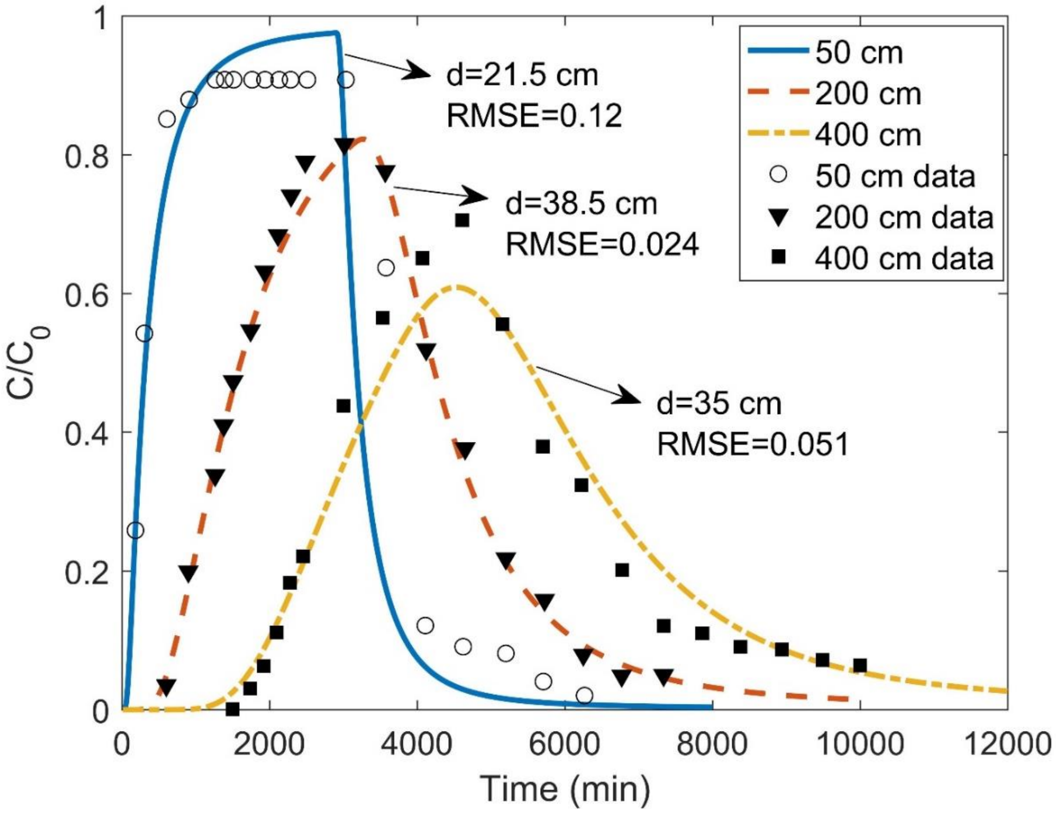

Fig. 4.10 Predicted BTCs with best fitting of dispersivities and observed data at 50 cm, 200 cm, and 400 cm (D_1=D_2=5×10^{-5} cm^2/min).

4.4.4 Evidence of dynamic molecular diffusions in the less permeable layers

As the simulated peak values failed to fit the observed data in Fig.4.10, this study also conducts the best fitting of diffusion coefficients for the less permeable (soil) layers, based on the observed BTCs at 50 cm, 200 cm and 400 cm in the sand layer. The constant dispersivity model is used in this section with a fixed dispersivity value of 38.5 cm. Since the upper and lower soil layers are packed with the same type of porous media, these two layers are assumed to have identical diffusion coefficients. However, one must be aware that although the upper and lower layers consist of the same type of porous media, they may still exhibit different physical properties such as permeability and diffusion, if the packing of these two layers does not follow the same procedure. Nevertheless, without any further information about the packing provided, it is reasonable to assume that these two soil layers have the identical properties including diffusion coefficients.

As the results shown in Fig. 4.11, allowing the diffusion coefficients of the surrounding layers to be fitting parameter can significantly improve the fitting results for both injection and leaching phases. The diffusion coefficient in either soil layer is simulated as 8.4×10^{-5} cm^2/min using observed BTC at 50 cm with RMSE of 0.126. If using observed BTC at 200 cm, the best-fitted diffusion coefficient in either soil layer is 3.2×10^{-5} cm^2/min with RMSE of 0.019. To obtain the best fitting of observed BTC at 400 cm, the diffusion coefficient in either soil layer is 1.7×10^{-5} cm^2/min with RMSE of 0.041. Above analysis suggests that with the increasing of travel distance, the best-fitted diffusion coefficient in either soil layer drops from 8.4×10^{-5} cm^2/min at 50 cm to 3.2×10^{-5} cm^2/min at 200 cm, and then further decreases to 1.7×10^{-5} cm^2/min at 400 cm. When the advective velocity keeps constant, a larger travel distance corresponds to a longer advective time, which corresponds to a lower value of diffusion coefficient.

One may recall that the diffusion coefficient in the soil layer can be express as: $D_1 = \tau D_0$, where D_0 is free-water diffusion coefficient, τ is a tortuosity factor, which is ranged from 0 to 1 and depends on how well the pores are connected to each other. An increasing tortuous pathway for diffusion corresponds to a smaller value of tortuosity factor, which would lead to a lower diffusion coefficient. Therefore, the simulated result in Fig. 4.11 appears to suggest that the “apparent” diffusion coefficient in the soil layer could be dependent on the advective time in the permeable layer, or more specifically, it decreases with such an advective time. The diffusive transport in the soil layer has to take place in more tortuous pathways at late times, as the easy (or convenient) pathways and large pores have been taken and occupied by solutes through diffusive transport at the early times.

We must point out that above speculation has not been tested in a rigorous theoretical sense, thus can only be regarded as a possible explanation of the observed phenomenon discovered in the best fitting exercises. The instantaneous mixing assumption used in this study may be partially responsible for the observation of such an apparent diffusion coefficient, an issue that deserves further scrutiny in the future. A Multi-Rate Mass Transfer (MRMT) model or mass transfer approach may justify the tailing of BTCs better, especially in one-dimensional system. However, using these models would induce new parameters, which are not always easy to quantify for practical work.

Interesting enough, above hypothesis about the existence of a dynamic (or advective time-dependent) diffusion in the less permeable layer is not without evidence from investigations in other disciplines in which diffusion is of concern. For instance, Latour et al. (1994) observed that time-dependent diffusion of water occurred in biological model systems, such as biological tissues. Sen (2004) provided a tutorial to obtain the information such as fluid type, surface relativity and macro-length by investigating the time-dependent diffusion coefficient at short and long times. Olayinka and Ioannidis (2004) used a random-walk simulation to study the relationship between surface-enhanced relaxation and time-dependent diffusion with a three-dimensional stochastic model. They used this model to recover the tortuosity of pore space and analyze the average pore surface-to-volume ratio. However, as far as we know, the physics of dynamic or time-dependent diffusion in porous media is still poorly understood (Reynaud, 2017), thus requires some great attentions in the future studies.

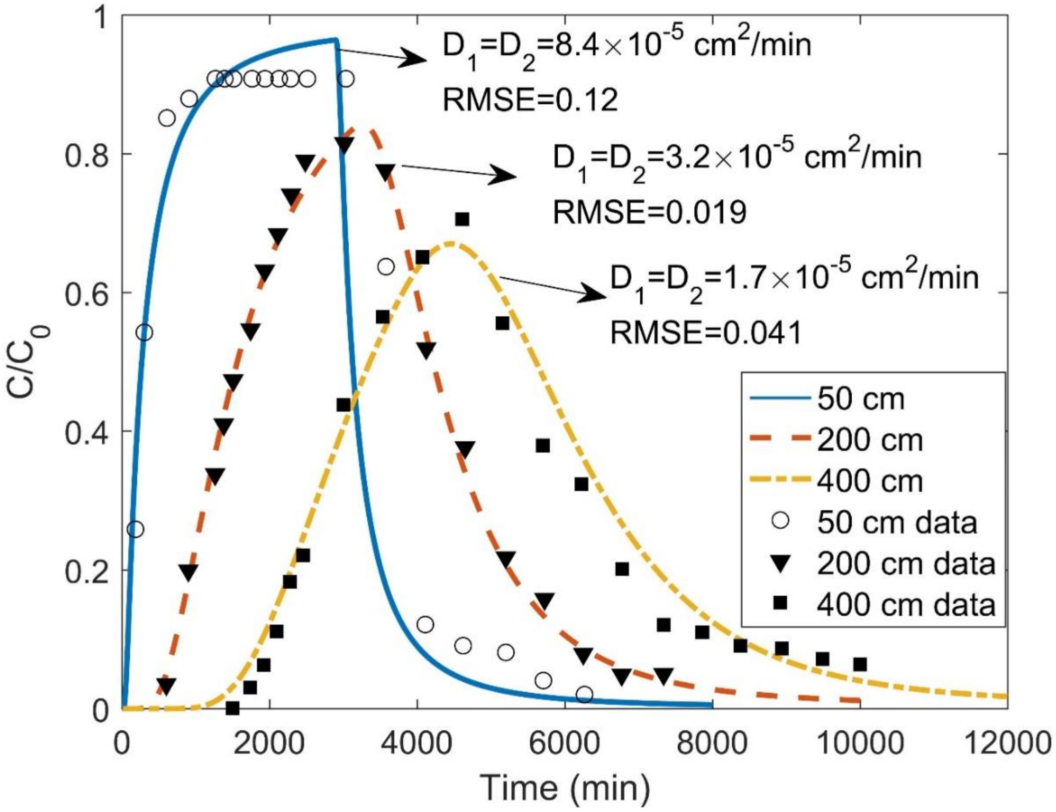

Fig. 4.11 Predicted BTCs with best fitting of effective diffusion coefficients and observed data at 50 cm, 200 cm, and 400 cm (D = 4.66 cm^2/min).

4.5 Discussion and conclusions

Solute transport in a stratified system is a classical problem in subsurface hydrology. The system investigated in this study includes a much permeable layer (such as a fracture or an aquifer) bounded by two much less permeable layers (such as rock matrixes or aquitards). Transport in an asymmetric stratified system is a fully coupled three-domain problem. The scale dependency of dispersion in such a system has never been examined before. This study constructs new transport models to describe reactive solute transport in such a stratified system and rigorously derives the semi-analytical solutions of these models. Furthermore, with the help of the new transport models and recently reported experiments conducted by Swami et al. (2016), we want to find out if the scale-dependent dispersion has to be considered or not. The following conclusions can be drawn from this study. In addition, the possible existence of dynamic or time-dependent diffusion in the less permeable layers is discussed with the support of experimental data and simulation results. Given the similarity of solute and heat transport in the subsurface, the newly established models can be applied to study heat transport in a stratified system by simply replacing the solute transport properties with the corresponding heat transport properties. The potential applications of this study include risk assessment of high-level nuclear waste disposal and the development of hot-dry-rock geothermal energy, among others.

The comparisons between the cases with and without transverse diffusions in the less permeable layers (Figs. 4.2-4.4) demonstrated the importance of diffusive processes in those layers for redistributing the mass of solute among different layers. Thus, diffusions in the less permeable layers should not be ignored for transport in a stratified system, especially at the later times. Without considering mass exchanges among different layers, BTCs will be overestimated considerably and fail to fit the transport parameters in the permeable layer accurately.

The linear scale-dependent dispersivity model is not a good choice for the stratified system due to its own limitations. The constant dispersivity model works almost equally well as the exponential scale-dependent dispersivity model, based on the tracer test experiments reported by Swami et al. (2016). Thus, we conclude that there is no obvious scale-effect of dispersivity for solute transport in the stratified porous media in Swami et al. (2016).

The diffusion coefficients in the less permeable layers appear to be dependent on the advective time in the permeable layer. More specifically, such diffusion coefficients decline with the advective time when the dispersivity of the permeable layer is assumed to be a constant. Further theoretical and experimental works are required to explain this phenomenon.

However, this study has some limitations that need discussion and further research. First, although the existence of dynamic (or time-dependent) diffusions in the less permeable layers appears to be convincing, one has to be aware that the evidence comes from the best fitting exercises only. To confirm this finding, further experiments specially designed to tackle this issue must be carried out. In addition, physically based theoretical works are also necessary to understand why such a phenomenon exists in a stratified system.

Second, despite the fact that this study acknowledges the possible scale-dependency of longitudinal dispersion in the permeable layer, this work assumes instantaneous mixing of solute in the vertical direction in the permeable layer. Therefore, the results obtained here are only suitable for a stratified system when the thickness of the permeable layer is a few orders of magnitude smaller than the scale of transport (such as a single fracture or a thin aquifer). The vertical dispersion in the permeable layer should be taken into consideration if the well-mixing concept cannot be used (when the thickness of the permeable layer is comparable with the scale of transport).

Third, groundwater in the less permeable layer is assumed to be immobile in this study, which is only true when the hydraulic conductivity of the less permeable layer is at least two orders of magnitude smaller than that of the permeable layer, and cross-formation flow is not a concern. If this is not true, advective and mechanically dispersive transports in the less permeable layer must be considered, in addition to the diffusive transport there.

Fourth, concentration continuity is maintained at the interfaces among different layers in this study. The possible complexity and concentration discontinuity at the interfaces may be investigated in the future.

Fifth, the bottom line of the approach here is the validation of ADE, a Fickian based local transport theory. It will be valuable to investigate the same experimental data set (Swami et al., 2016; Swami et al., 2014) using other non-local transport theories such FADE and CTWR, and to compare the results of different theories to gain new insights of transport in a stratified system.

5. DEPOSITIONAL AND REACTIVE TRANSPORT COUPLED MODEL FOR CARBONATE DIAGENESIS

5.1 Introduction

As a rich natural laboratory, the deep-sea sediments are usually used for the study of early marine diagenetic processes. The chemical records of sediments and associated pore fluids are the results of the balance between supply and removal (Coggon et al., 2010). As the result, the chemical interactions such as dissolution and precipitation of certain minerals are captured by the chemical composition of the sediments and pore fluids. Many factors would impact seawater chemistry, such as tectonic activities, biological and depositional activities. Those activities are thought to affect global climate by influencing the carbon dioxide in atmosphere (Elderfield and Schultz, 1996; Wilkinson and Algeo, 1989). Thus, reconstructing the records of ocean chemistry in the past will be helpful to achieve better understanding of such biogeochemical carbon cycle processes and their influence on global climate changes.

Strontium (Sr) and calcium (Ca) are conservative chemical species in the ocean. Their concentrations in seawater are uniform anywhere at any one time. Several main geological processes would control the concentrations of Sr and Ca in seawater. The major supplier of Ca in the ocean includes the dissolve river input, the weathering of continents and the hydrothermal exchange at mid-ocean ridge. The consumption of Ca in the ocean is mainly caused by calcium carbonate deposition. Sr has similar fluxes into the ocean: 1). Sr is carried to the ocean by rivers from continents; 2). Sr is supplied by hydrothermal alteration of seafloor basalt; 3). Sr is affected diagenesis of carbonate sediments in the ocean.

Since the Sr fraction in pore fluids is much smaller than that in calcite sediment, a small amount of calcite recrystallization would cause a significant change of Sr concentration in the pore water (Baker et al., 1982; Delaney, 1989). The partition coefficient of Sr between calcite solid and porewater is considered to be directly related to Ca in the form of strontium calcium (Sr/Ca) ratio (Morse and Bender, 1990; Richter, 1996). By this means, the strontium calcium ratio is widely used as a proxy for investigating the diagenesis and determining the paleo records of seawater conditions (Coggon and Teagle, 2011; Hampt and Delaney, 1997). Many efforts have been made to study the diagenetic processes and calcite recrystallization by using the Sr/Ca ratios of bulk carbonate and pore fluids as geochemical tracers (Fantle and DePaolo, 2006; Richter, 1993, 1996; Richter and Depaolo, 1987, 1988). Specifically, Richter and Depaolo (1987) applied the Sr budget model to Deep Sea Drilling Project (DSDP) Site 590B and concluded that the exchange rate decreases dramatically over depth. The near surface value of exchange rate at DSDP Site 590B was about 10% per million years. However, this rate dropped to 1% per million years below 200 m. Richter (1996) further considered the influence of sulfate whenever the pore fluids were saturated with celestite and provided an newly improved model by coupling strontium and sulfate budget models. Fantle and DePaolo (2006) evaluated the calcite recrystallization rate for Ocean Drilling Program (ODP) Site 807 and provided an evidence of the rapid rise of Magnesium (Mg) concentration in seawater over the last 10 million years. Many these studies also pointed out that the calcite recrystallization rate is an exponential function of age or depth of sediments (Fantle and DePaolo, 2006; Richter, 1996; Turchyn and DePaolo, 2011). The recrystallization rate is large at the top of sediments but rapidly decreases over age or depth of sediments.

Efforts also have been made to reconstruct past seawater chemical conditions in multiple methods: Graham et al. (1982) and Delaney et al. (1985) attempted to reconstruct the strontium calcium ratios with planktonic foraminifera. Their results showed high variations and considerable scatter because of vital effects. Elderfield et al. (2000) analyzed the strontium calcium ratios on eight planktonic foraminifera species, which were collected from a core top transect of North Atlantic. The measured results from different species indicated significant differences. Lear et al. (2003) used the samples of benthic foraminifera preserved in the deep-ocean core samples from various sites of DSDP and ODP core data to construct the Cenozoic seawater Sr/Ca ratios. Other than experimental methods, Stoll and Schrag (1998) analyzed the variations of Sr and Ca concentrations at shelf carbonates over Quaternary sea level cycles with a simple box model. Their model predicts that Sr/Ca ratios in the ocean varied 1 to 2 percent over Quaternary sea level changes. Coggon et al. (2010) estimated past oceanic Mg/Ca and Sr/Ca ratios from the Mid-Ocean calcite carbonate veins that precipitated in both cool and warm ocean ridge flank basalts. However, their constructions underestimated the chemical concentration in history and indicated a large discrepancy against with experimental measurements.

In this study, we developed a coupled numerical model with the consideration of advection, diffusion, and the recrystallization (dissolution and precipitation) between bulk carbonate and pore fluids in the processes of deposition and compaction. By matching the chemical records of pore water, we are able to quantitatively estimate the recrystallization rates and analyze the diagenetic processes during the carbonate deposition. Furthermore, comparing the simulation results with Sr/Ca ratios allows us to reconstruct the past chemical conditions in the ocean.

5.2 Geological background and site descriptions

The Sites 803 (3410 m), 805 (3188 m), 806 (2520 m) and 807 (2805 m) are selected for this study to provide a nearly continuous record of calcareous pelagic sediments deposited at different water depths on the Ontong Java Plateau, which is a broad, shallow and mid-oceanic submarine plateau and located in the western equatorial pacific (Kroenke et al., 1991). Leg 130 (Sites 803-807) was drilled into the basement on the northeaster margin of the Ontong Java Plateau (3°36.42´N, 156°37.49´E). It covers a complete record of Neogene, Paleogene and Late Cretaceous history (Fantle and DePaolo, 2006).

For these four sites, the carbonate sections are deposited on 113 to 117 Ma oceanic crust with a thickness of 40 km. The calcite content of the sediment averages more than 90%. Well 807C indicates that the depth to basement in Site 807 is near 1380 mbsf. Age assignments are made using a linear fit to the biostratigraphic control points identified by Kroenke et al. (1991). The sedimentation rates can be calculated from the age assignments and depths of the sediments before compaction. Decompaction is conducted based on the method described in section 5.3. The sedimentation rates are reversely correlated with water depths of the sites. Site 803 with the largest water depth has the slowest sedimentation rate, and Site 806 has the smallest water depth and the largest sedimentation rate.

The studied sites are believed to be free of major disturbances in the sediment columns. Most of the sediments are homogeneous nannofossil-foraminiferal oozes composed of low magnesium calcite. Most have not been exposed to subaerial diagenesis and meteoric waters during sea level lowering or tectonic uplifts, nor have they been subjected to tectonic deformation that would alter their petrology and physical properties. Site 804 is not selected for this study because this site was affected by mass movement. Seismic profiles exhibit irregular seismic reflections and show evidence of wedging. Physical properties profiles in Site 804 reflect these major sediment disturbances (Kroenke et al., 1991).

There is no evidence of a significant flux of modern seawater into the sedimentary section at the studied sites (Fantle and DePaolo, 2006), which limits the transport of aqueous species to diffusion. Therefore, the results from this study are applicable to deep sea environments with low energy and minimum external disturbances, which are referred to as closed systems in some references (Bjørlykke and Jahren, 2012).

5.3 Mathematical model

This section outlines the procedures used in developing the coupled 1D depositional and reactive transport model, using the data from deep sea drilling site 807 as an example. The model is capable of modeling deposition and compaction of the sediments, advection and diffusion of chemical species in pore fluids, and reactions between sediment minerals and pore fluids. The model starts with no sediments or pore fluids above the base rock. In each time step, one layer of sediment and associated pore fluid is added. The pore fluid would inherit the composition of seawater at deposition as it initial condition. The Sr/Ca ratios in newly deposited sediments are set up in a way that the modeled post-diagenesis Sr/Ca ratios in the bulk solid matches the measured values in the sediments today. Diffusion and reactions are calculated based on the governing equations and parameters listed below. The advection and vertical flow in the sediments are not considered in the study of ODP Sites 803-807 as the advection caused by sediments' compaction is relatively minor and not critical to the final results (Richter, 1993). Currently, there is no evidences of Sr isotopes and concentrations that can confirm the exitance of significant vertical flow at these sites.

The recrystallization rate of calcite in the sediments is essentially constrained by matching the Sr concentrations in pore fluids. Sr concentration in the fluid generally increases with depth in sea sediments due to its higher concentration in the solid phase than in seawater. As calcite dissolves, Sr is released from the solid phase to pore fluids in sediments, and this is balanced by the incorporation of Sr in the solid phase during calcite precipitation, diffusion and advection at steady state (Morse and Bender, 1990; Richter, 1996).

In order to simulate the pore fluid Sr concentrations correctly, sulfate and calcium concentrations are required. The history of sulfate concentration in pore fluids is needed to evaluate whether the pore fluid is saturated with celestite, in which case the Sr concentration is modeled based on celestite equilibrium. The partition of Sr between the pore fluid and solid is based on Sr/Ca ratios, therefore requiring the Ca concentration history. The Sr concentration in the pore fluid is modeled after both calcium and sulfate concentrations are matched.

5.3.1 Deposition and compaction

The data from Site 807 (age, depth, porosity, etc.) is first interpolated on to a uniform 1m grid. The mass fraction of solid (*m*) at each grid point is calculated using the relation between volume fraction of fluid φ and sub-bottom depth z (Richter and Depaolo, 1987):

$$m(z)=\frac{\left(1-\phi\right)\rho_c}{\left(1-\phi\right)\rho_c+\phi\rho_f}, \tag{5.1}$$

where ρ_c and ρ_f are the densities of carbonate solid and porewater. The 1 m intervals are uncompacted to a uniform solid mass fraction $m(0)$ which results in a new thickness h for each interval:

$$h=m(z)/m(0). \tag{5.2}$$

The unevenly spaced uncompacted data is used to construct a new uniform 1 m grid. The new 1 m layers are the units deposited at the appropriate time in the calculation. Every time a new layer is added, the total thickness of sediment has to be calculated by requiring that the mass of solid is conserved consistent with the porosity-depth relation. If the total thickness before deposition is H, and $H + \Delta H$ after deposition, we must require that:

$$\int_0^{H+\Delta H} m(z)dz = \int_0^{H} m(z)dz + m(0)\,. \tag{5.3}$$

Finding the unknown ΔH involves repeating the integration until the correct value is found to sufficient accuracy. After decompaction, the sedimentation rates of studied site are plotted in Fig. 5.1.

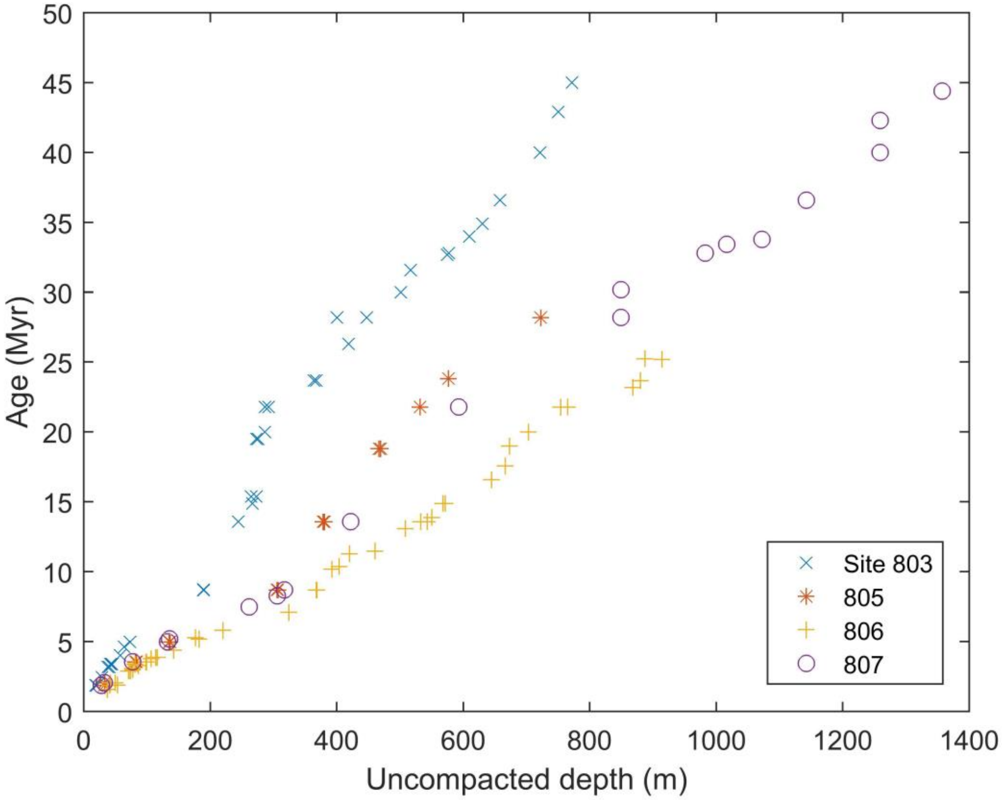

Fig. 5.1 Sedimentation rates in the studied sites from uncompacted depth and age.

5.3.2 Sulfate and organic carbon budget models

The equations for porewater sulfate used here are taken from the Sulfate budge model (Berner, 1980). The rate of change of the sulfate concentration, $[SO_4^{2-}]$, and utilizable organic carbon, G, in constant porosity porewaters are governed by:

$$\frac{\partial[SO_4^{2-}]}{\partial t} = D_{[SO_4^{2-}]}\frac{\partial^2[SO_4^{2-}]}{\partial z^2} - v\frac{\partial[SO_4^{2-}]}{\partial z} - Lk_{[SO_4^{2-}]}G\,, \tag{5.4}$$

$$\frac{\partial G}{\partial t} = -k_{[SO_4^{2-}]}G\,, \tag{5.5}$$

where $D_{[so_4^{2-}]}$ is the sulfate ion diffusion coefficient, which is assumed to be same value as strontium diffusion coefficient in this study, L is a stoichiometric coefficient corresponding to the number of sulfate ions reduced for every carbon oxidized, and $k_{[so_4^{2-}]}$ is the carbon oxidation rate constant. The stoichiometric constant, L, is taken to be 1/2. v is velocity in the pore water.

5.3.3 Calcium reactive transport

The pore fluid calcium concentration [Ca^{2+}] can be modeled using an equation similar to Eq.(5.4):

$$\frac{\partial[Ca^{2+}]}{\partial t} = D_{[Ca^{2+}]}\frac{\partial^2[Ca^{2+}]}{\partial z^2} - v\frac{\partial[Ca^{2+}]}{\partial z} + f_c M[Ca^{2+}]_s R_{net}\,, \tag{5.6}$$

where $R_{net} = R_d - R_p$, R_d is the dissolution rate of calcite, and R_p is the precipitation rate of calcite. [Ca^{2+}]$_s$ is the concentration of calcium in carbonate solid, in unit of mole/g. f_c is the fraction of calcite in the total sediment, and M is the mass ratio of solid to fluid ($\rho_s(1-\phi)/\rho_f\phi$). The diffusion coefficient for Ca in solution $D_{[Ca^{2+}]}$ (m^2/Myr) is considered as a function of temperature T (in kelvin) (Boudreau, 1997; Fantle, 2015): $D_{[Ca^{2+}]} = \left(3.60 + 0.179\times\ (\text{T-273.15})\right)\ \times\ 525.6$. The seawater Ca concentration (mM) is varied with time (Myr). The estimation of historical Ca concentration in the ocean from

Antonelli et al. (2017) is adopted as the initial conditions of Ca concentration in the pore water: $[Ca^{2+}]_{seawater} = 10.62 + 0.161 \times t$.

5.3.4 Strontium reactive transport

The conservation equations for the pore fluid [Sr^{2+}] and solid [Sr^{2+}]$_s$ strontium are descripted as follows:

$$\frac{\partial [Sr^{2+}]}{\partial t} = D_{[Sr^{2+}]} \frac{\partial^2 [Sr^{2+}]}{\partial z^2} - v \frac{\partial [Sr^{2+}]}{\partial z} + R_d f_c M [Sr^{2+}]_s - R_p f_c M K_{Sr} [Sr^{2+}], \tag{5.7}$$

$$\frac{\partial [Sr^{2+}]_s}{\partial t} = -V \frac{\partial [Sr^{2+}]_s}{\partial z} - R_d [Sr^{2+}]_s + R_p K_{Sr} [Sr^{2+}], \tag{5.8}$$

where K_{Sr} is the effective equilibrium partition coefficient for Sr between calcite solid and porewater; V is the velocity of solid due to compaction. It is worthwhile to note that the velocities of the pore fluid and solid at ODP leg 130 are very small, which can be ignored (Fantle and DePaolo, 2006, 2007). The diffusion coefficient for Sr in solution $D_{[Sr^{2+}]}$ (m^2/Myr) is considered as a function of temperature T (in kelvin) (Boudreau, 1997; Fantle, 2015): $D_{[Sr^{2+}]} = \left(3.69 + 0.169 \times \text{ (T-273.15)}\right) \times 525.6$. The concentration of strontium in pore fluid is also affected by celestite. We assume that the precipitation of celestite is instantaneous; therefore, the strontium concentration is calculated from celestite equilibrium whenever the product of strontium and sulfate concentrations exceeds saturation. The apparent solubility of celestite ($K_{sp}^{\text{celestite}}$) is obtained by fitting the measured $[Sr]_f [SO^{2-}]_f$ with depth at depths below 200 meters, where the pore fluid is saturated with regard to celestite.

The DuFort-Frankel finite difference algorithm is adopted to overcome the stability problems of the simple FTCS and Richardson methods. It is unconditional stable with the Von Neumann-stability analysis. Eqs. (5.7)-(5.8) are written in the forms as follows:

$$\begin{aligned}\frac{Cf_j^{n+1}-Cf_j^{n-1}}{2\Delta t} &= \frac{D}{\Delta z^2}\left(Cf_{j+1}^{n}+Cf_{j-1}^{n}-Cf_j^{n+1}-Cf_j^{n-1}\right)-v\,\frac{Cf_{j+1}^{n}-Cf_{j-1}^{n}}{2\Delta z}, \\ &\quad +R_d f_c M Cs_j^{n-1}-R_p f_c M K_{Sr} Cf_j^{n-1}\end{aligned} \tag{5.9}$$

$$\frac{Cs_j^{n+1}-Cs_j^{n-1}}{2\Delta t} = -V\,\frac{Cs_{j+1}^{n}-Cs_{j-1}^{n}}{2\Delta z}-R_d Cs_j^{n-1}+R_p K_{Sr} Cf_j^{n-1}, \tag{5.10}$$

where C_f and C_s refer to the strontium concentration in the pore fluid $([Sr^{2+}])$ and carbonate solid ($[Sr^{2+}]_s$), the subscription *j* and superscription *n* are the step numbers of depth and time, respectively.

Below we list the values of input parameters used in the simulation in Table 5-1. The porosity functions with depth are from Bassinot et al. (1993). The net dissolution rate of calcite is obtained by fitting the measured calcium-depth profile with Eq.(5.6). The seawater calcium concentration ($[Ca^{2+}]_{sw}$) is assumed as a function of time in the geological history, based on estimations in Antonelli et al. (2017). The pore fluid sulfate concentration is modeled using Eq.(5.4) by assuming the seawater sulfate concentration ($[SO_4^{2-}]_{sw}$) also as a function of time (Algeo et al. (2015). Strontium concentrations in fluid and solid are modeled with Eqs. (5.7)-(5.8), but the pore fluid strontium is also subject to saturation with celestite.

The equilibrium partition coefficient of strontium in calcite K_{Sr} is a function of temperature. In-situ temperature is the studied sites are measured by temperature logging tools (Sawyer et al., 1994). The empirical relation between K_{Sr} and temperature T (in kelvin) is adopted:

$$\ln K_{Sr} = -4.38 + 1.71 \times 10^{3} / T - 4.22 \times 10^{5} / T^{2}. \tag{5.11}$$

We find that the pore fluid Sr concentrations cannot be fit with the calculate K_{Sr} no matter how we tune the value of R_d and can only be fit reasonably well when all K_{Sr} values are decreased by 0.006. This indicates the value of K_{Sr} might have been overestimated before. In any case K_{Sr} generally increases with temperature and therefore depth of the sediment. The range of calculated K_{Sr} values (after subtraction by 0.006) are listed in Table 5-1 and 5-2.

It is worthwhile to point out the initial conditions of this system. As a large reservoir of dissolved Sr, the ocean supplies the initial conditions of the system. At each time step, it created the initial pore fluids with equal Sr and Ca concentrations to the contemporaneous seawater. The Sr/Ca ratio in the initially deposited carbonate bulk was related to seawater by an effective partition coefficient, which is assumed to be a constant parameter over time and keep identical among all Leg 130 sites (Fantle and DePaolo, 2006). In this study, the value of the effective partition coefficient between carbonate bulk and seawater would be adjusted until the simulated seawater at $t = 0$ matches modern oceanic compositions, which equals to 0.194.

Table 5-1 Parameters of calcium, sulfate and strontium models at Site 807.

Parameter	Value (Site 807)
Porosity (ϕ)	$0.696\times e^{-0.00051z}$
Sedimentation Rate (S) [m/Myr]	30.4
R_{net} [Myr^{-1}]	2×10^{-5}
$[Ca]_{sw}$ [mM]	10.3+0.1556×t
G_0 [mM/kg]	11
$k_{[SO_4^{2-}]}$ [Myr^{-1}]	0.3
$[SO_4^{2-}]_{sw}$ [mM]	28-0.15×t
$K_{sp}^{celestite}$ [mM^2]	20.73-0.003557×z
K_{Sr}	0.0177 - 0.0221
R_d [Myr^{-1}]	$0.019\times e^{(-z/400)}$

Table 5-2 Parameters of coupled models at Sites 803, 805 and 806.

Parameter	Site 803	Site 805	Site 806
ϕ	$0.686\times e^{-0.00075z}$	$0.702\times e^{-0.00076z}$	$0.692\times e^{-0.00045z}$
S [m/Myr]	16.9	26.0	36.9
R_{net} [Myr^{-1}]	2×10^{-4}	2×10^{-4}	5×10^{-5}
$[Ca]_{sw}$ [mM]	10.3+0.1556×t	10.3+0.1556×t	10.3+0.1556×t
G_0 [mM/kg]	19	19	34
$k_{[SO_4^{2-}]}$ [Myr^{-1}]	0.28	0.35	0.17
$[SO_4^{2-}]_{sw}$ [mM]	28-0.15×t	28-0.15×t	28-0.15×t
$K_{sp}^{celestite}$ [mM^2]	20.7-0.0014×z	16	18.7-0.0007×z
K_{Sr}	0.0177 - 0.0199	0.0181 - 0.0225	0.0185 - 0.0201
R_d [Myr^{-1}]	$0.018\times e^{(-z/120)}$	$0.038\times e^{(-z/150)}$	$0.03\times e^{(-z/400)}$

5.4 Results analysis and validation

5.4.1 Chemistry species profiles in the solid and porewater

Initially, the oceanic Sr concentration is assumed to be a constant over time. This produces current Sr/Ca ratios in the bulk solid that are different from the measured ratios. The Sr concentrations in the depositional sediment are then modified and iterated until the modeled solid Sr/Ca ratios match the current measurements to adequate accuracy. The corresponding Sr concentrations in seawater are also modified since the carbonate calcite was initially deposited with a certain partition coefficient from seawater.

Fig.5.2 presents the initial Sr/Ca ratios in sediments before diagenesis (yellow line) that produce the post diagenesis Sr/Ca ratios (blue line) that best match the measured data. The shift of the Sr/Ca ratios in the bulk sediment is larger in deep sediments because they have been through more diagenetic changes, while the top sediments are less heavily modified. Diagenesis generally reduces the Sr/Ca ratios in the sediments because the release of Sr by calcite dissolution is larger than the incorporation of Sr by reprecipitation. The shift can be as high as 0.3 mM/M.

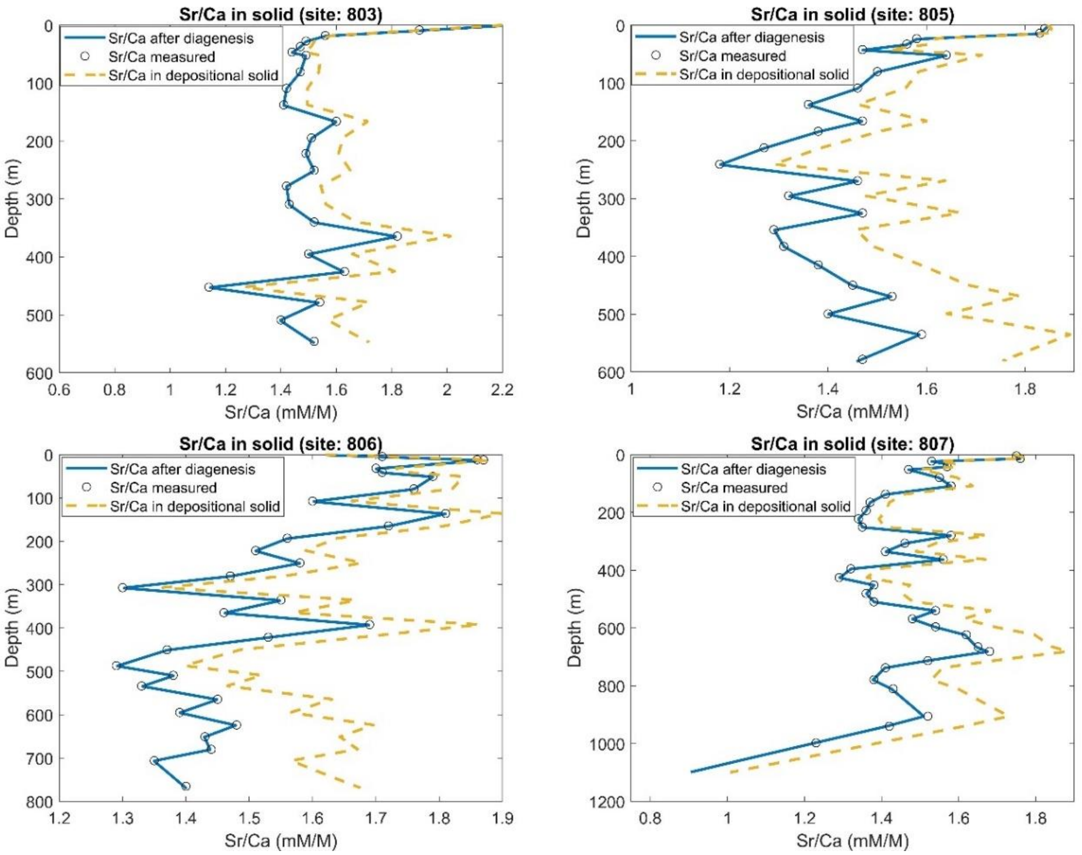

Fig. 5.2 The Sr/Ca ratio in bulk carbonate before and after diagenesis, compared with measured data of solid samples.

The pore fluid Ca concentration in Site 807 can be matched reasonably well with a constant $R_{net} = 2 \times 10^{-5}$, which is much smaller than the estimated R_d (0.019 at the top of the sediments). This confirms that calcite is close to equilibrium with the pore fluid, and the net reaction rate is extremely small compared to the dissolution rate. The measured pore fluid concentrations of calcium can therefore be assumed as equilibrium values for calcite.

Another approach to model the evolution of calcium concentration in pore fluids is to formulate the net reaction rate as $R_{net} = k_{Ca^{2+}} \left(\left[Ca^{2+} \right]_{eq} - \left[Ca^{2+} \right] \right)$, where $k_{Ca^{2+}}$ is the reaction rate constant, and $\left(\left[Ca^{2+}\right]_{eq}-\left[Ca^{2+}\right]\right)$ is how far the pore fluid Ca is from the equilibrium value. $\left[Ca^{2+}\right]_{eq}$ is obtained by fitting the current Ca concentrations in pore fluids as a function of depth. In the geological past when the seawater Ca concentration was higher, $\left[Ca^{2+}\right]_{eq}$ is modified by the ratio of paleo Ca concentration to current Ca concentration in seawater. Therefore, the only tunable parameter in the Ca model is $k_{Ca^{2+}}$. The parameters used to model Ca, sulfate, and Sr listed in Table 5-2.

Figs. 5.3-5.5 present the fitting of our model to the measured pore fluid concentrations of sulfate, calcium and strontium. The historical concentrations are also presented for illustrative purposes. Because the sediments grow upward during geological history, the upper boundary of the concentration profiles moves up with the top of the sediments. These upper boundaries of sulfate and calcium, when connected, record the paleo seawater concentrations, which are assumed to be linear functions of geological time. The concentration of Sr in seawater is calculated from the Ca concentration and the Sr/Ca ratio in seawater recorded in the bulk solid as in Fig.5.2. The best fitting of Sr concentration in pore fluids is achieved by tuning the value of R_d, which provides the recrystallization rates of calcite needed for this study.

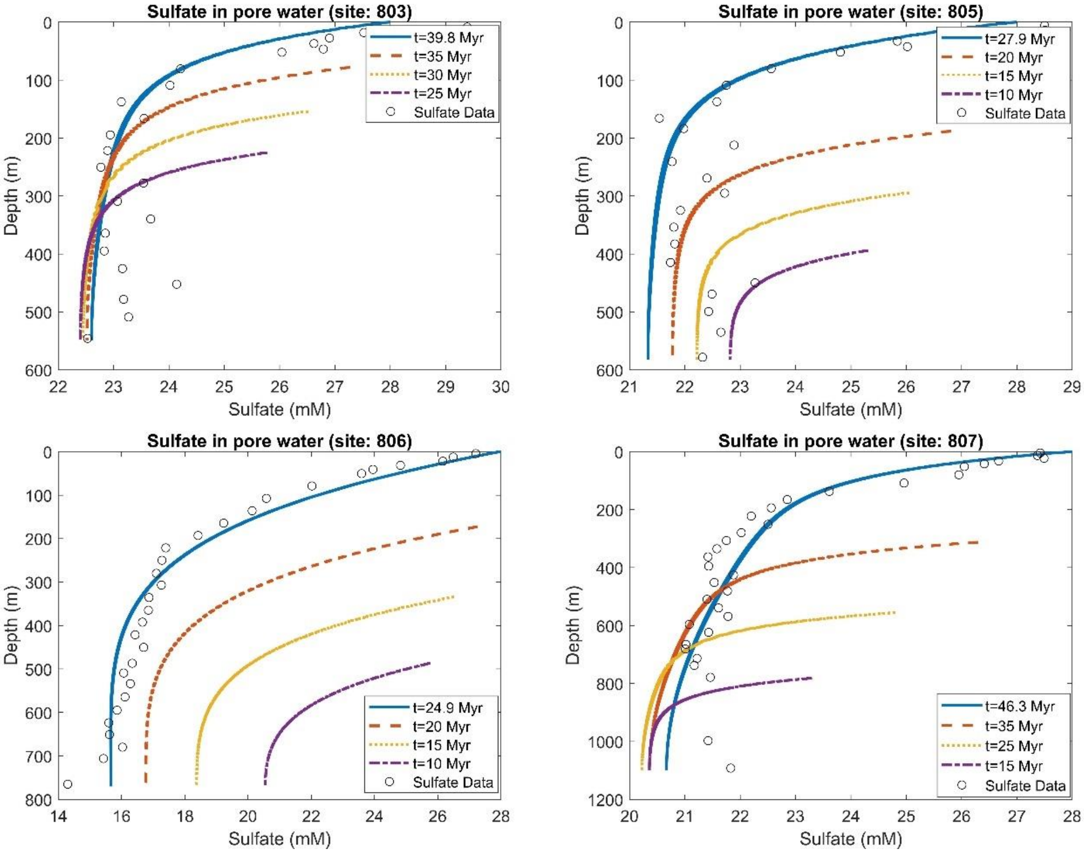

Fig. 5.3 Modeled evolution of sulfate concentration in the pore fluid compared with measured concentrations in samples.

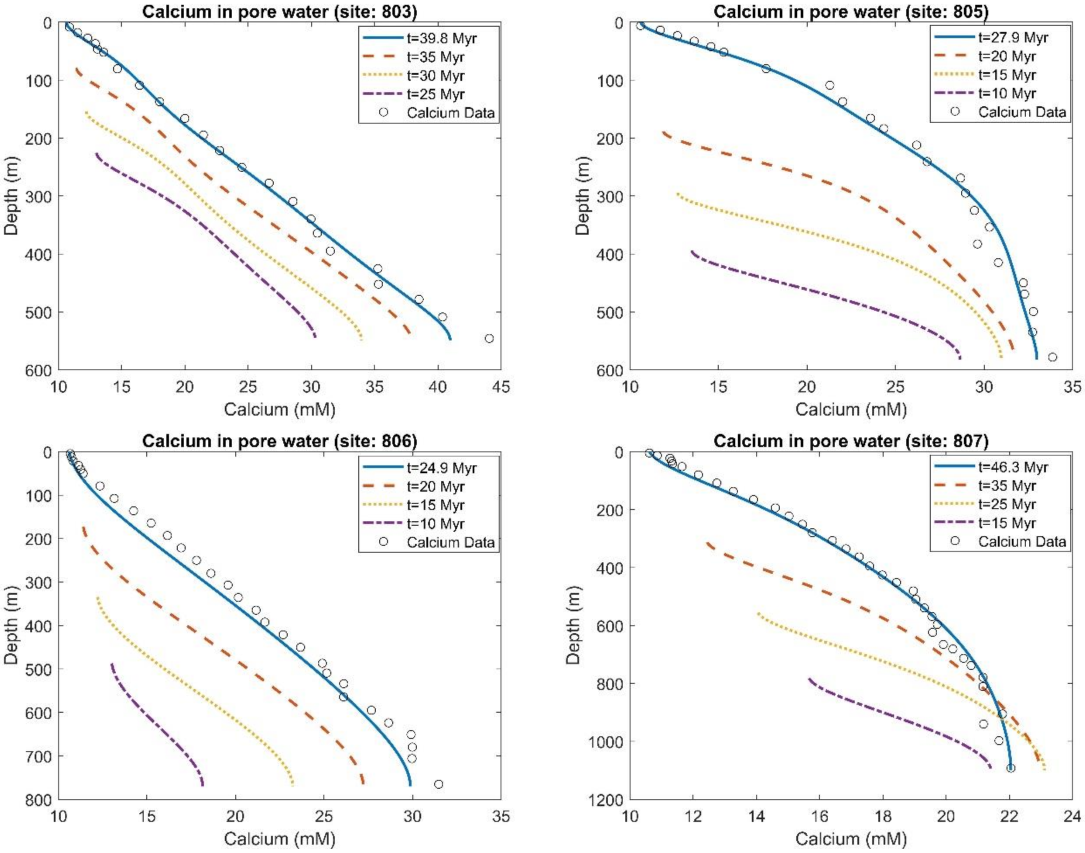

Fig. 5.4 Modeled evolution of calcium concentration in the pore fluid compared with measured concentrations in samples.

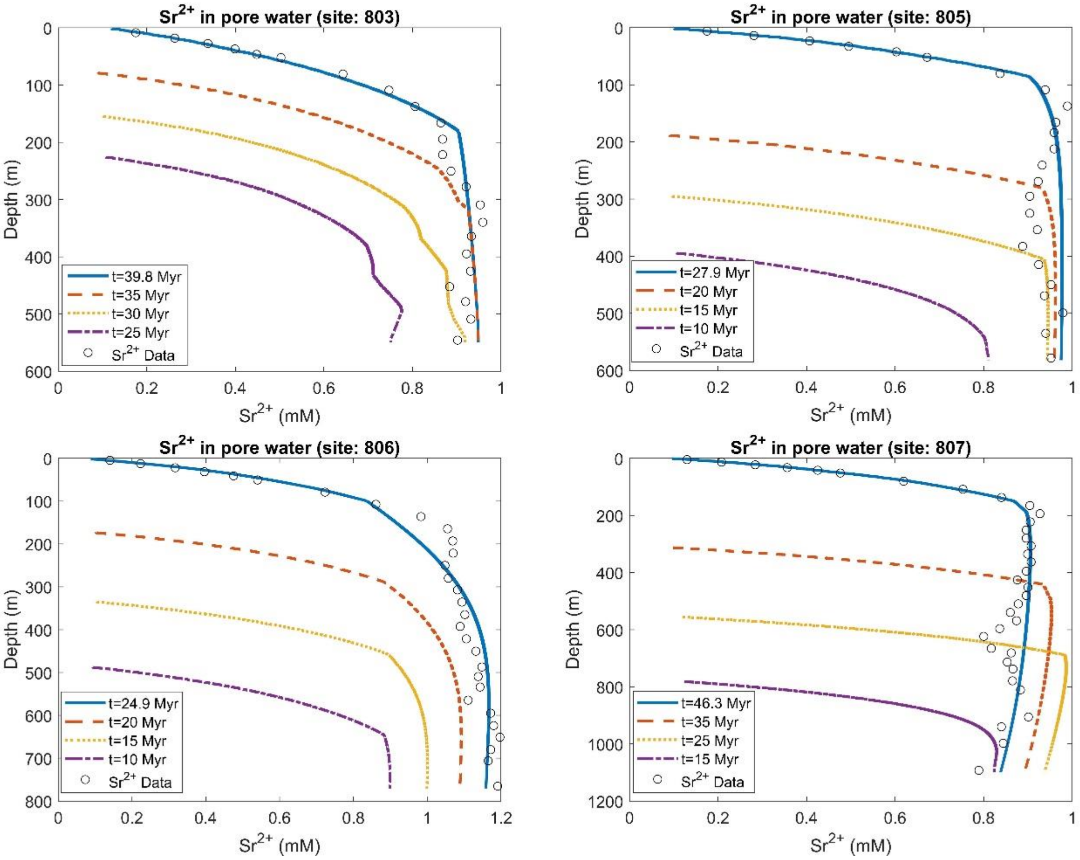

Fig. 5.5 Modeled evolution of strontium concentration in the pore fluid compared with measured concentrations in samples.

5.4.2 Reconstruction of past chemical conditions in the ocean

After matching the measured data of strontium, calcite and sulfate concentrations in the pore fluid and the carbonate bulk, the paleo Sr/Ca ratios in seawater can be produced. The simulation is validated against the experimental measurements in foraminiferal by Lear et al. (2003). The Sr/Ca ratio measured in planktonic foraminiferal has been considered for a while in the study of seawater Sr/Ca ratios (Delaney et al., 1985; Graham et al., 1982; Martin et al., 1999). However, the results showed considerably large variation. Compared to Planktonic foraminiferal, benthic foraminifera are usually better preserved in deep sea core with excellent age control. Therefore, benthic foraminifera are considered as an outstanding indicator for paleo record of seawater Sr/Ca ratios. Lear et al. (2003) carefully picked the well-preserved foraminifera to minimize the influence of post-depositional diagenesis. Samples were crushed and cleaned with ultra-sonication treatments and other solutions. They are dissolved in 0.075 M HNO_3 and analyzed with Inductively Coupled Plasma Atomic Emission Spectroscopy (ICP-AES) after leaching with a weak acid. The measurements were then converted to the seawater Sr/Ca ratio with effective partition coefficients. Thus, the experimental work done by Lear et al. (2003) is considered to provide an accurate and reliable measurements on past oceanic chemical conditions.

Both simulated results from Leg 130 (Sites 803, 805, 806 and 807) and measured data from Lear et al. (2003) are plotted with different markers in Fig 5.6. The simulated results from four sites are in good agreement with each other and show narrow variations compared to the experimental measurements. The modeled results disagree with Coggon et al. (2010) estimations from the compositions of calcite veins in oceanic crust. This discrepancy is mainly attributed to the uncertain biogenic carbonate-Sr partition coefficient in their study.

The measured data points from Lear et al. (2003) are intensively distributed in 14 Ma to present and 50 Ma to 30 Ma. Many details are missing due to availability of benthic foraminifera samples from 30 Ma to 14 Ma. The simulation results from this study could replenish this gap and provide the detailed variations within 30 Ma to 14 Ma. As indicated in Fig. 5.6, Sr/Ca ratios between 26 Ma to present were lower than modern ocean. There are several Sr/Ca ratios cycles from 40 Ma to present: from 40 Ma to 26 Ma (Eocene to Oligocene), seawater Sr/Ca ratios gradually increased from 6.5 mM/M to 10 mM/M; from 26 Ma to 8 Ma (Miocene to Pliocene), it decreased at first and then increased to 8.5 mM/M in a short term and followed by a slightly decreasing to 7 mM/M; from 8 Ma to present, Sr/Ca ratio in the ocean increased from 7 mM/M to 10 mM/M. The temporal changes in Sr/Ca ratio represent the fluxes variations of Sr in and out the ocean. River usually plays the most important role of supplier of Sr into seawater. Carbonate production and diagenesis are the main sinks for Sr and Ca concentrations. The short-term changes of Sr/Ca ratio in the ocean are the result of the sea level variations, which cause exposure of diagenesis of shelf carbonates.

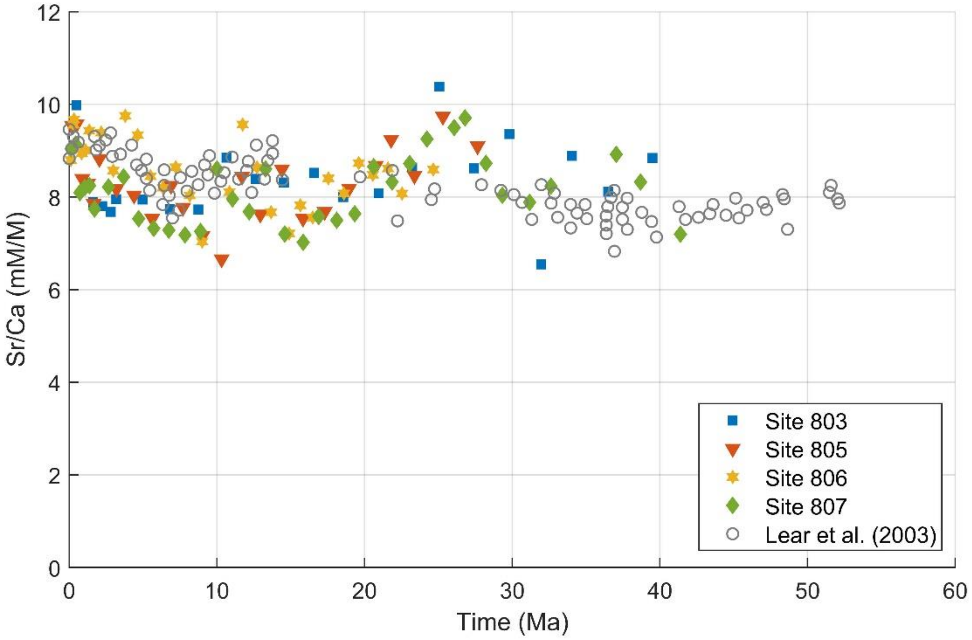

Fig. 5.6 Reconstructed paleo Sr/Ca ratios in the ocean and the experimental measured data from Lear et al. (2013).

5.5 Discussion and conclusions

This study couples the depositional and compactional processes, advective and diffusive transport, and recrystallization processes (dissolution and precipitation) in the deep-sea carbonate sediments. Strontium, calcium and sulfate concentrations of ODP core data at Sites 803, 805, 806 and 807 are used to support our model. The effect of celestite precipitation on Sr budge is also taken into consideration: when the pore fluid is saturated with celestite, the Sr concentration is controlled by the apparent solubility of celestite.

As important proxies to reconstruct the historical ocean conditions and investigates the early diagenesis of carbonate sediments, the simulated concentrations of Sr and Ca are carefully compared to the ODP measured data. By matching the profiles of both chemical elements in carbonate bulk and pore fluids, this coupled model can simulate the calcite diagenetic processes, reconstruct past 40 million years seawater Sr/Ca ratios and provide a quantitative estimations of calcite recrystallization rate in the deep-sea sediments. After the validation against the experimental measurements from benthic foraminifera, our estimations are proven to be reliable and robust: the simulated results from ODP Sites 803, 805, 806 and 807 show a narrow variation and a good agreement with the experimental measurements. It replenishes the missing measurements with more details and data points during 30 Ma to 14 Ma in Fig.5.6: the experimental results from Lear et al. (2003) indicated a slowly decreasing trend of Sr/Ca ratios in the ocean from 30 Ma to 14 Ma due to its own limitations (missing samples of this time period). However, our modeled results provide more information and show that the Sr/Ca ratios rapidly increased from 30 Ma to 26 Ma, and then gradually dropped from the peak value at 10 mM/M at 26 Ma to 7 mM/M at 14 Ma. The modeled past seawater strontium cycles can be used to other relevant research areas, such as the ocean circulations, paleo climate and the chemical evaluation of the ocean.

This coupled model has some obvious advantages than the experimental measurements: the model is very efficient to make estimations without long-time preparation works and does not require the investigation of samples’ eligibility. Lear et al. (2003) selected benthic foraminiferal calcite for the best performance. Coggon et al. (2010) used the composition of calcite veins formed in the oceanic crust to reconstruct past oceanic Sr/Ca ratios. However, our model can directly use the measurements from ODP core data.

However, the study still has some limitations for future improvement: Firstly, to reconstruct past seawater chemical history, this coupled model requires reliable measurements of Sr/Ca ratio in the carbonate bulk and porewater. The Sr concentration in the pore fluid is very sensitive to the calcite recrystallization rate. Thus, an inaccurate measurement of Sr concertation in the pore fluid would result to unreliable estimations of recrystallization rates. The time scale of solid chemical data also limits the time scale of reconstruction. The reconstruction of oceanic conditions can only be tracked up to the earliest time of the solid data. Secondly, this one-dimensional coupled model considers the vertical advection and diffusion in the solid and pore water and ignores the horizontal transport processes, which may also affect the chemical conditions and can be added in the future study. Thirdly, this coupled model requires relatively consistent sedimentation environment without major sediment disturbances or tectonic activities. Thus, the sedimentation history and depositional age profile would be carefully checked before simulation.

6. CHEMICAL AND MECHANICAL COMPACTIONS IN CARBONATE SEDIMENTS DURING EARLY MARINE DIAGENESIS

6.1 Introduction

Carbonate geologists have been trying to understand the various diagenetic pathways through which carbonate sediments become lithified for decades. It was believed for a long time that carbonate sediments compact very little mechanically (Bathurst, 1970; Weller, 1959). Bathurst (1970) stated that most ancient micrites and biomicrites showed no sign of having been compacted. Delicate tests were uncrushed, thin skeletal structures had not been broken because of grain-to-grain movement. The conclusion is that cement was precipitated in the pores in sufficient quantity to form a resistant framework before the overburden was great enough to cause detectable compaction.

Evidence for mechanical compactibility emerged later (Chanda et al., 1977; Shinn et al., 1977). Several experiments were conducted after that on compaction of carbonate sediments (Bhattacharyya and Friedman, 1979), which provided certain constraints on the parameters of the compaction process. The approach to study compaction in natural settings, however, was mostly limited to examining compacted rocks for characteristics and evidence of compaction. Quantitative evaluation of the relative fractions of mechanical compaction and chemical cementation during lithification is challenging from just examining the rocks after compaction.

Another question that bothers geologists for a long time is the source of the calcite cement (Bathurst, 1970). Because the concentration of calcium in the pore fluid is much lower than in the solid, it requires thousands of pore volumes to precipitate the amount of calcite observed in the rocks today. Consensus has been reached now that pressure solution provides calcite for all the cement precipitated during burial diagenesis of carbonate ooze in some deep-sea cores (Matter, 1974; Schlanger and Douglas, 1974). Pressure solution is defined as a process by which grains dissolve at intergranular or intercrystalline contacts. This process is presumably related to the higher solubility under non-hydrostatic stress at the contacts than at free grain surfaces. The process often, although not always, is accompanied by reprecipitation at adjacent free grain surfaces. Therefore, the dissolution of carbonate sediment itself provides the source for calcite precipitation and does not require transport of thousands of pore volumes of fluid.

The assumption that local pressure solution provides the calcite for cementation allows us to calculate the relative fraction of chemical compaction and mechanical compaction in reducing porosity in deep sea cores. It is observed that the dissolution rate of calcite in deep sea cores is slow, but significant, and decreases with depth in the sections (Fantle and DePaolo, 2006). If chemical compaction is mediated by dissolution on the vertical direction where stress is high, and precipitation on the horizontal directions, the vertical deformation of sediments can be assumed equal to the amount of calcite dissolution. By integrating the dissolution rates of carbonates during the depositional history, one can estimate the porosity loss caused by chemical compaction. The porosity today, when compared with depositional porosity, provides the total porosity loss by both chemical compaction and mechanical compaction. Therefore, we can quantitatively evaluate the importance of each component in reducing porosity during carbonate lithification.

The deep-sea cores selected for this study come from the Ocean Drilling Program (ODP), Site 803, 805, 806, and 807. During Leg 130, nearly 4800 m of pelagic calcareous sediments were recovered from 16 holes drilled at 5 sites (803-807) on a depth transect located in the northeastern part of the Ontong Java Plateau (Kroenke et al., 1991). Based on DSDP and ODP data, numerous studies have been conducted on changes of porosity with depth of burial and age in pelagic calcareous sediments (Bassinot et al., 1993; Hamilton, 1971).

Hamilton (1971) derived the empirical polynomial equations of porosity and density over depth for various types of deep-sea sediments (pelagic clay, radiolarian ooze, diatomaceous ooze, and calcareous ooze). These generalized equations give an approximate idea of how porosity evolves with depth of burial. Bassinot et al. (1993) used shipboard laboratory porosity values where sedimentological analyses (such as carbonate content) were performed on the same sample and fit the porosity-depth profiles with regression curves for the same sites chosen for this study. They show that the porosity can be fit reasonably well with exponential equations. Their regression equations are used in this study as the true porosity of the sediments today.

Based on DSDP data, Schlanger and Douglas (1974) proposed a diagenetic model for calcareous sediments. In this model, two stages are present in the reduction of porosity with depth of burial: (1) an early dewatering stage in the upper 200 mbsf, in which porosity is reduced from about 80% to 60% and the dominant mechanism is mechanical compaction; (2) a slower dewatering stage in which porosity is reduced from about 65% to 40% between 200 and 1000 mbsf and the dominant mechanism is cementation. Later studies show that the initiation of cementation through solution-precipitation mechanisms may occur more rapidly (after burial of a few tens of meters) in the calcareous sedimentary column, with cement reaching about 25% of the solid volume at the ooze-chalk transition (Wetzel, 1989). For Leg 130 sites, Bassinot et al. (1993) concluded that chemical compaction was of minor importance in ooze and chalk samples from Sites 803 and 807, and mechanical compaction is most likely the major process acting throughout the entire ooze-chalk sections studied.

In this study, we re-evaluate the conclusion in Bassinot et al. (1993) by numerically modeling the depositional history of the carbonate sediments in these four sites, considering compaction of the sediments, reactions between carbonate solid and pore fluids, and transport of aqueous species by diffusion. The measured pore fluid strontium concentrations are used to constrain the rates of calcite recrystallization. The reaction rates are then integrated through the depositional history which provides the estimation of porosity loss by the chemical compaction. The results indicate that neither chemical compaction nor mechanical compaction dominates the total porosity loss, but both contribute significantly throughout the sections.

6.2 Site descriptions and analytical methods

This study adopts the coupled depositional and reactive transport model in the previous chapter. The processes of advection, diffusion, and reaction of strontium and calcium, and the organic carbonate related budget model of sulfate are coupled with the sediments deposition and compaction processes. The simulation results are supported by the ODP data, which includes the major geochemical data and core descriptions. The ODP Leg 130 (Sites 803, 805,806 and 807) data is used mainly for the discussion of chemical and mechanical compaction in carbonate sediments. The detailed site descriptions are mentioned in Section 5.2. This coupled model is also applied to some other sites of ODP data (Sites 925, 926, 927, 928, 984, 1082, 1085, 1119 and 1239) for the discussion of the relationship between the calcite recrystallization rate and sediments conditions, such as the carbonate content ratio and sedimentation rate.

ODP Sites 925-928 (Leg 154) are located on the Ceara Rise, which is a bathymetric high formed at the Mid-Atlantic Ridge. The sites positions are located northeastward of South American coast and the Amazon Delta. The high terrigenous influx from Amazon River delivered relatively moderate to high sedimentation rates (from 18.9 m/Myr to 25.9 m/Myr). The dominant sediments are the nannofossil oozes, nannofossil clays and some terrigenous silt. ODP Site 984 (Leg 162) is situated on the Bjorn Drift in about 1650 m water depth. It is in the North Atlantic, southwest of Iceland. The major sediments of ODP Site 984 are terrigenous and fine-grained from Holocene to late Pliocene. The sediments were accumulated from the detrital flow along the southwest edge of the Reykjanes Ridge at a very high sedimentation rate (163 m/Myr). The carbonate fraction of ODP Site 984 at about 8%, mainly contributed by authigenic carbonate minerals and calcareous nannofossil ooze. ODP Sites 1082 and 1085 are from Leg 175, which is located off western coast of Africa. Sedimentation rates at Leg 175 are relatively high: Site 1082 has an average sedimentation rate at 118 m/Myr, Site 1085 has an average sedimentation rate at 53.6 m/Myr. Site 1082 sediments are mainly composed of nannofossil and foram-rich and diatom-rich clays. Site 1085 is composed of nannofossil ooze and various amounts of silts and clay. ODP Site 1119 is located about 93 km offshore from eastern South Island (New Zealand) at about 395 m water depth on the upper continental slope. The sedimentary materials are shed eastward or southward from Southern Alps into eight major river systems. These rivers delivered a larger amount of terrigenous sediments to the east coast area, which would finally transport northward and enter the ocean environment. Thus, the sedimentation rate at this site is very high (195.8 m/Myr). ODP Site 1239 (Leg 202) is situated about 120 km off the Ecuador coast, near the eastern crest of Carnegie Ridge at about 1414 m water depth. Sediments at Site 1239 are dominated by foraminifer-bearing diatom nannofossil oozes and occasional ash layers. It has an average relatively high sedimentation rate of 82 m/Myr.

6.2.1 The rates of calcite recrystallization and mechanical compaction

The recrystallization rates of calcite obtained in this study are defined as the fraction of calcite dissolved per million years. The results are around 2-4 percent per million years at the top of the sediments and decrease exponentially with depth (Table 5-2). The total compaction rate can be calculated from the decrease of porosity with age as the following:

$$R_{total} = \frac{\Delta\phi}{(1-\phi)\Delta t}, \tag{6.1}$$

where Δt is the age of the sediment, and $\Delta \phi$ is the change of porosity from depositional porosity, which is assumed be to the same as the porosity of the top sediments today. Bassinot et al. (1993) uncompacted the porosity in the four studied sites to the original depositional porosity using site-specific empirical regression equations and found that the depositional porosity was rather constant (their figure 6). Therefore, we could calculate the total compaction rate from the rate of porosity decrease per unit time from its original value. The results are around 3-5 percent per million years at the top of the sediments and decrease with depth/age (Fig. 6.1).

The difference between total compaction rate and calcite recrystallization rate gives the rate of mechanical compaction. Our first order conclusion is that the total compaction rate is generally less than twice the value of chemical compaction rate at the top of the sediments, therefore the mechanical compaction rate is smaller than the chemical compaction rate. As the depth becomes larger, both compaction rates decrease, but the total mechanical compaction rate becomes more than twice the value of the chemical compaction rate, and in some cases is more than 10 times larger. Therefore, the main mechanism responsible for porosity reduction in deep sections is mechanical compaction.

If one compares only Site 803, 806, and 807, the mechanical and chemical compaction rates are related to sedimentation rate. Slow sedimentation rate (Site 803) is associated with smaller compaction rate, both chemical and mechanical, while high sedimentation rate (Site 806) has larger compaction rates. Site 805 has abnormally high compaction rates although its sedimentation rate is intermediate. It seems that the chemical rate is related to mechanical compaction rate. When the mechanical compaction rate is high, chemical compaction follows.

6.2.2 The relative importance in reducing porosity

Integrating the compaction rates with time gives the cumulative effect of each component on porosity reduction. For a given amount of calcite dissolution $R_d\Delta t$, the porosity change caused by chemical compaction can be calculated as:

$$\Delta\phi_c = \left(1-\phi\right) R_d \Delta t \; . \tag{6.2}$$

Because both chemical and mechanical compaction rates decrease with depth (therefore age) exponentially, the reduction in porosity is mainly controlled by the compaction rates in the first few million years. In shallow sediments, the reduction of porosity by mechanical and chemical compaction is almost equal because the rates are similar for Site 803. In deeper sections, both mechanical and chemical compactions still contribute to porosity reduction, but the mechanical compaction rate becomes larger than the chemical compaction rate. Therefore, the relative fraction of porosity loss by mechanical compaction becomes larger with depth. The fraction of chemical compaction in total porosity loss is about 1/4-1/3 in the deepest section. This is smaller than the fraction of mechanical compaction but is still significant. In the cases of Site 805 and 807, chemical compaction contributes more to porosity reduction than mechanical compaction in shallow sections. This relation is reversed in deeper sections, but in Site 806 chemical compaction contributes more throughout the whole section.

The relative contribution of chemical compaction to porosity reduction is related to sedimentation rate of the site, which is expected due to the correlation between compaction rates and sedimentation rates. Site 803 has the slowest sedimentation rate (16.9 m/Myr), and the relative importance of chemical compaction is smallest in Site 803 compared to in other sites. Site 806 is the opposite. Site 805, although with extremely high compaction rates, also falls into this order.

Our quantitative estimation of the compaction rates and their contributions to porosity reduction disagrees with previous conclusions in Bassinot et al. (1993) and Schlanger and Douglas (1974) in two perspectives: 1) Mechanical compaction is not the dominant process in the upper section; chemical compaction contributes an equal amount or even more to porosity reduction. 2) Chemical compaction becomes relatively less important in deep sections compared to in shallow sections, not more important.

The estimation of chemical compaction in this study is based on the assumption that all calcite dissolution occurs in the vertical direction along grain contacts. Therefore, the chemical compaction rate is equal to the calcite recrystallization rate, which is constrained by the pore fluid Sr concentrations. However, it is also possible that calcite dissolution occurs horizontally which also releases Sr into the pore fluid, which does not cause chemical compaction. In that case the chemical compaction rate is smaller than the calcite recrystallization rate estimated based on Sr profiles. Therefore, our calculation in this study provides the upper limit of chemical compaction in contributing to porosity reduction.

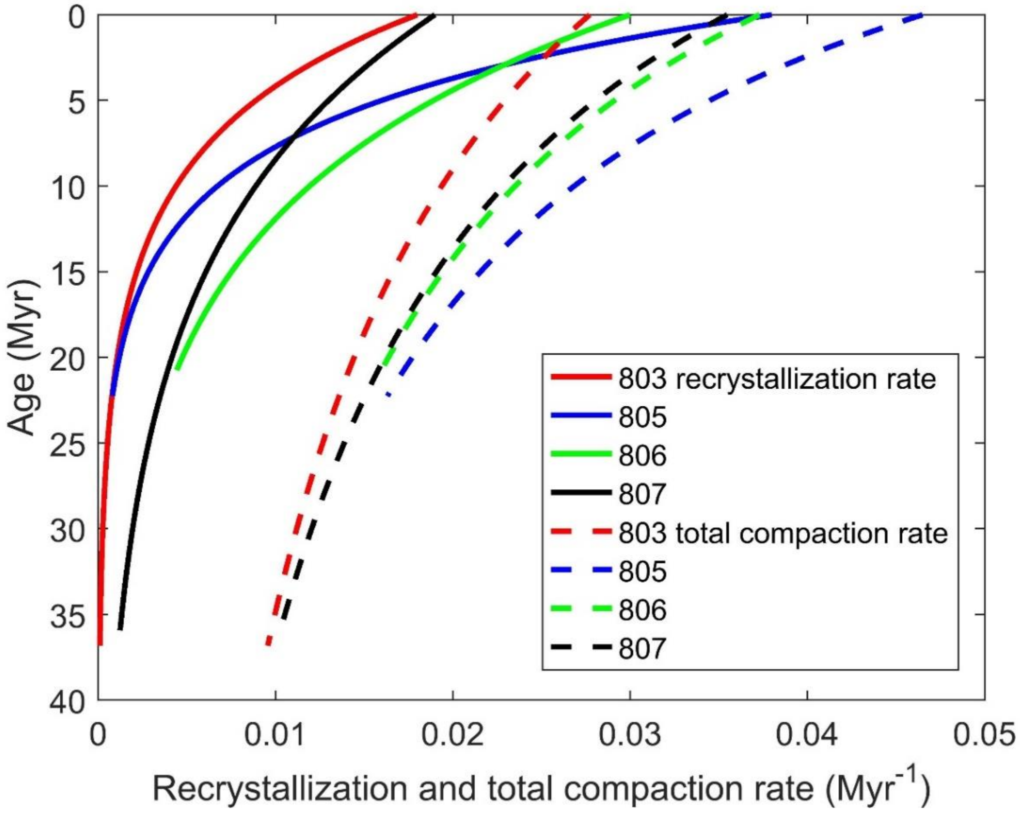

Fig. 6.1 Recrystallization rates of calcite inferred from strontium concentrations in the pore fluid of Sites 803-807, compared with compaction rates of sediment.

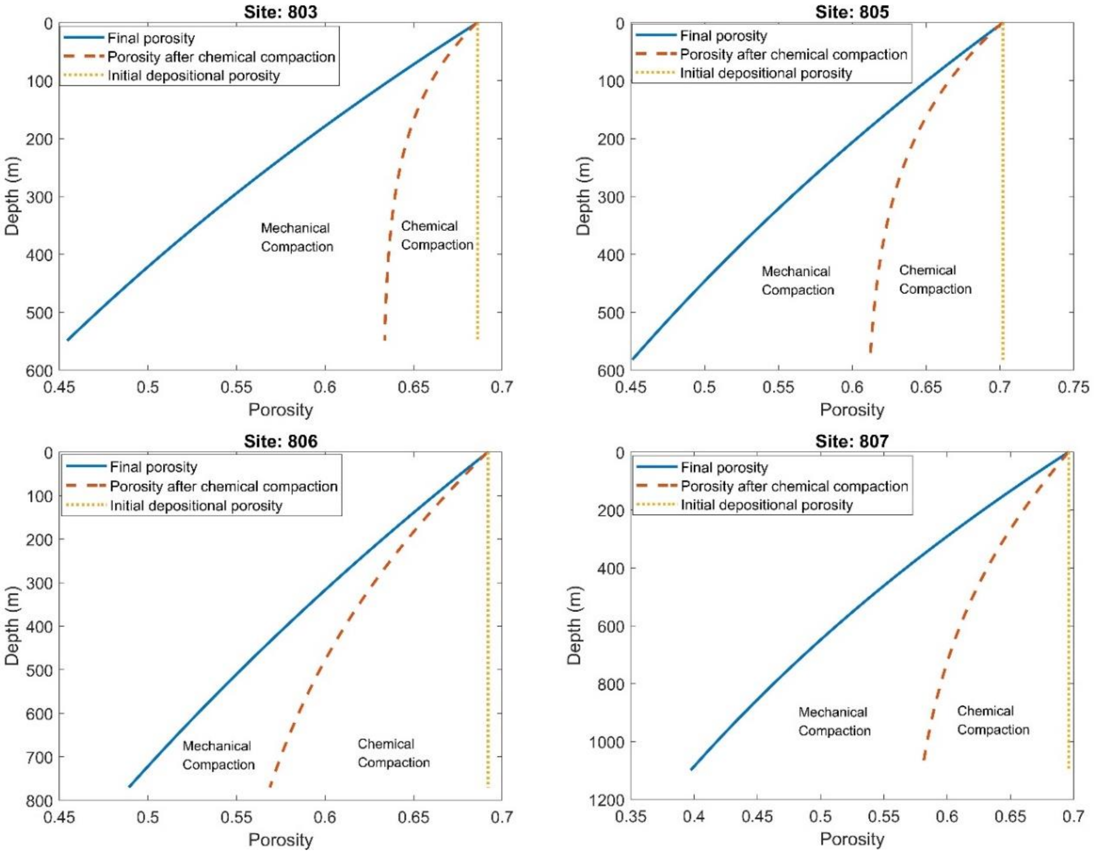

Fig. 6.2 Fractions of mechanical compaction and chemical compaction in contributing to porosity reduction.

6.2.3 Recrystallization rate and depositional conditions

To fully analyze the calcite Sr/Ca ratios in terms of carbonate diagenesis and oceanic evolution history, it is required to distinguish the influence of changes in ocean conditions and different mixes of calcite-depositing organisms as contributors on deep-sea sediments during diagenetic calcite recrystallization. In this section, the impact of sedimentation conditions on calcite recrystallization process would be summarized and discussed.

By matching Sr and Ca concentrations in pore fluids, the reaction rate can be estimated. The reaction rates of calcium in carbonate sediments are concluded as an age-dependent parameter in previous studies (Fantle and DePaolo, 2006; Richter and Liang, 1993): the dissolution rate (R_d) of carbonate sediments decreases with age. However, the relationship between the depositional conditions (such as carbonate content ratio and sedimentation rate) and the dissolution rate (R_d) has never been discussed yet.

This coupled model is applied to more sites (Sites 803-807, 925-928, 984, 1082, 1085, 1239 and 1119) with various sedimentation conditions. Those chosen sites here have relatively stable sedimentation conditions. The previous studies of reaction rates (Sites: 590B, 575, 575B, 594, 305, 516 and 289) are also summarized (Richter and Liang, 1993). The simulation results of strontium and calcium and measured data from ODP are plotted in Figs. 6.3-6.4. The modeled values are listed in Table. 6-1.

It is worthwhile to point out that more precipitation than dissolution is observed in the ODP Sites 984, 1082, 1085, 1119 and 1239. To better characterize the exchange processes of Sr and Ca between carbonate solid and pore fluids during precipitation of calcite from aqueous solutions, a kinetic model of trace element fractionation proposed by DePaolo (2011) is adopted here to quantify K_{sr} for sites with more precipitation:

$$K_{sr} = \frac{K_f}{1 + \frac{R_d}{R_p}\left(\frac{K_f}{K_{eq}} - 1\right)} , \tag{6.3}$$

where K_f is the forward kinetic fractionation factor for Sr/Ca ratio in the precipitation reaction, K_{eq} is the equilibrium Sr/Ca partition coefficient when the precipitation is extremely slow, the value of K_{eq} can be acquired by the activity coefficient of dissolved

$SrCO_3$ in calcite. In this study, we adopt their values (K_f = 0.24, K_{eq} = 0.025) from DePaolo (2011).

The relationships between calcite dissolution rates at the top of sediments and the carbonate content ratio and average sedimentation rate are carefully examined and plotted in Figs. 6.5-6.6. The carbonate content ratio is from a very low value of 8% at Site 984 with an initial calcite dissolution rate of 0.002 Myr^{-1} to a relative pure carbonate site of 92.4% with initial calcite dissolution rate of 0.019 Myr^{-1} at Site 807. Most of our investigated sites are within the range of 60% to 90%. As shown in Fig. 6.5, the higher the carbonate content, the more thoroughly sediments would be cemented. The exponential regression of all data sets between carbonate content (f_c) and calcite dissolution rate (R_d) is: $R_d = 0.002 \times e^{0.0328 f_c}$. The upper bound is $R_d = 0.002 \times e^{0.0328 f_c} \times 3$ while the lower bound is $R_d = 0.002 \times e^{0.0328 f_c} / 3$. All the data points are within the range between the lower and upper bounds. Based on the modeled results and collected data, for sites with low average carbonate contents in sediments, their calcite dissolution rates appear to be slower. It suggests that large composition of noncarbonate sedimentary components, such as terrigenous sediments or biogenic silica, has suppressed calcite recrystallization at these sites.

The average sedimentation rates (corrected for decompaction) of modeled sites has the value from 5.4 m/Myr at Site 305 (R_d = 0.0181 Myr^{-1}) to 195.9 m/Myr at Site 1119 (R_d = 0.005 Myr^{-1}). Most of them are deposited at the rate between 10 m/Myr to 40 m/Myr. In Fig. 6.6, the empirical exponential regression between the average sedimentation rate (SR) and calcite dissolution rate (R_d) is: $R_d = 0.0338 \times e^{-0.012 SR}$. The upper and lower bounds are $R_d = 0.0338\times e^{-0.012SR}\times 6$ and $R_d = 0.0338\times e^{-0.012SR}/6$. The sites with lower sedimentation rates during deposition would have more extensive dissolution rates. The calcite dissolution would benefit from low sedimentation rate at those sites.

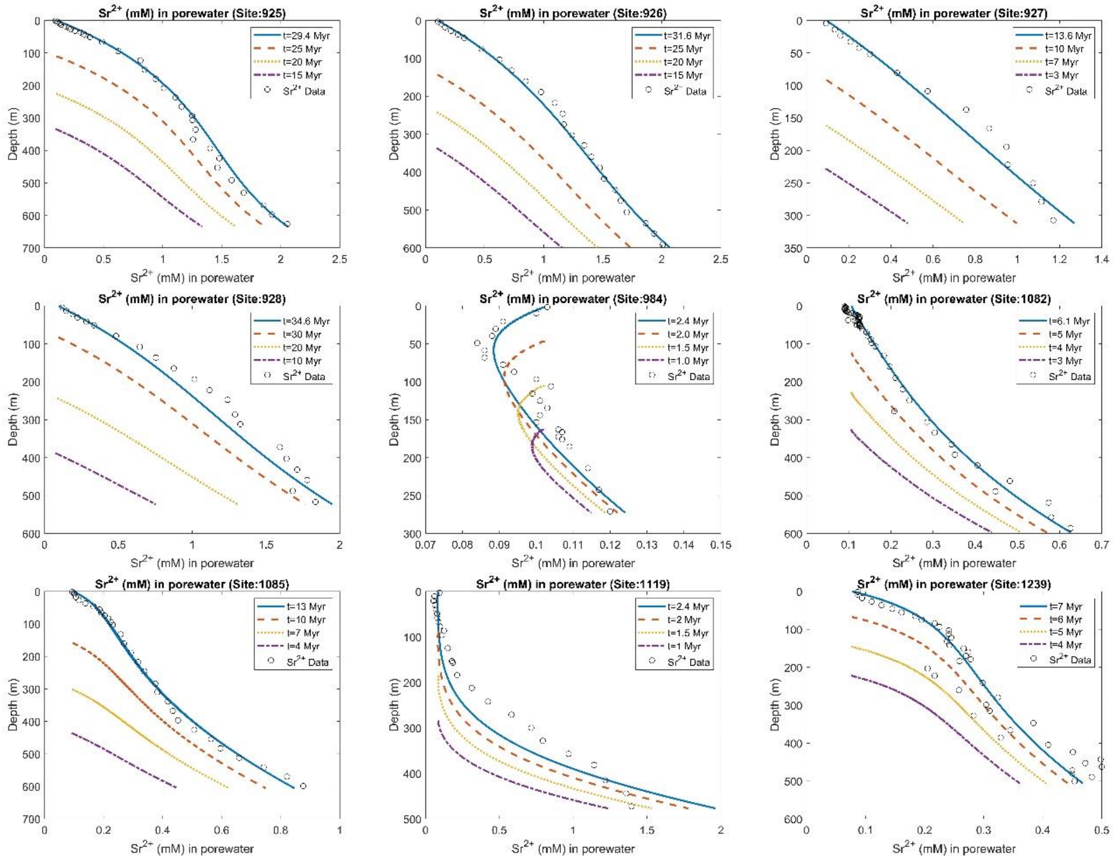

Fig. 6.3 Simulation results of Sr concentration in the pore fluid at Sites (925, 926, 927, 928, 984, 1082, 1085, 1119 and 1239) from ODP data.

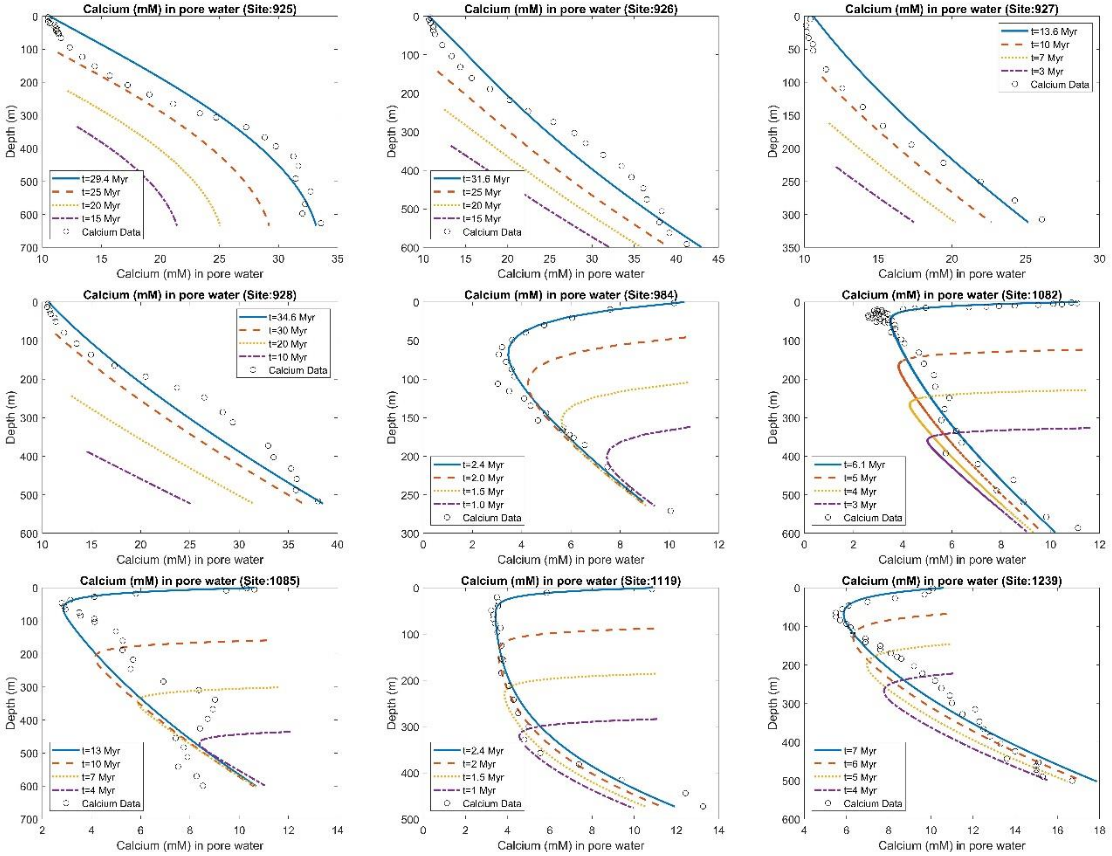

Fig. 6.4 Simulation results of Ca concentration in the pore fluid at Sites (925, 926, 927, 928, 984, 1082, 1085, 1119 and 1239) from ODP data.

Table 6-1 Simulated parameters of various sites.

Site	Average sedimentation rate (m/Myr)	Average carbonate content (%)	R_d (Myr^{-1})	R_{net} (Myr^{-1})
925	26	66.4	0.013×exp(-z/600)	0.00015×exp(-z/600)
926	22.6	61.9	0.012×exp(-z/600)	0.00008×exp(-z/100)
927	25.9	58	0.011×exp(-z/300)	0.00001×exp(-z/100)
928	18.9	57.5	0.012×exp(-z/500)	0.00002×exp(-z/100)
984	163	8	0.002×exp(-z/25)	-0.0385×exp(-z/23.5)
1082	118	44.9	0.013×exp(-z/600) + 0.0008	-0.025×exp(-z/10) + 0.00008
1085	53.6	65.9	0.0095×exp(-z/110)	-0.0035×exp(-z/15)
1119	195.9	15.5	0.005×exp(-z/50)	-0.037×exp(-z/10)
1239	82	59	0.028×exp(-z/100)	-0.0037×exp(-z/22)

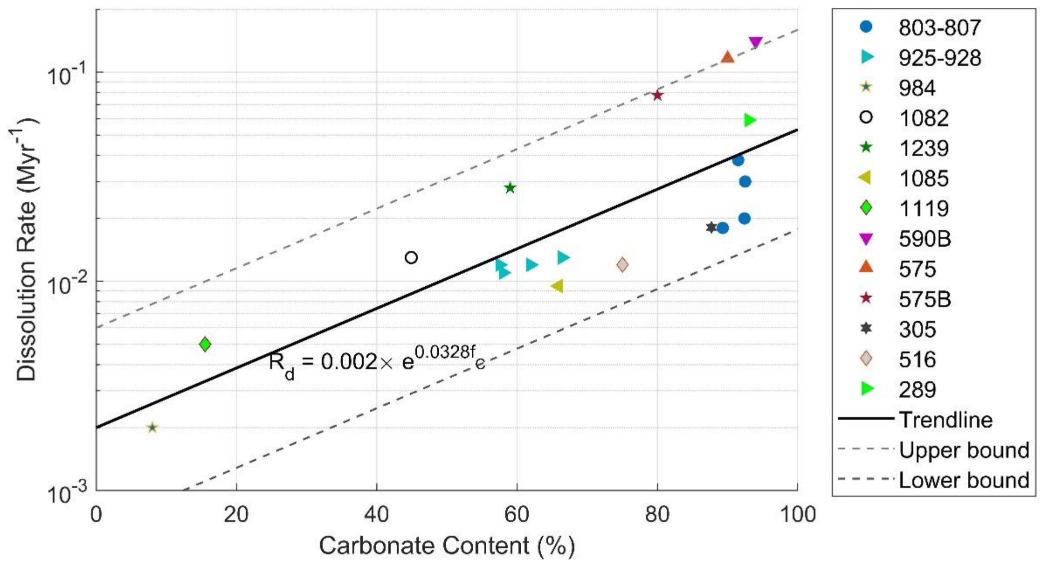

Fig. 6.5 Relationship between dissolution rate (Myr^{-1}) and carbonate content (%).

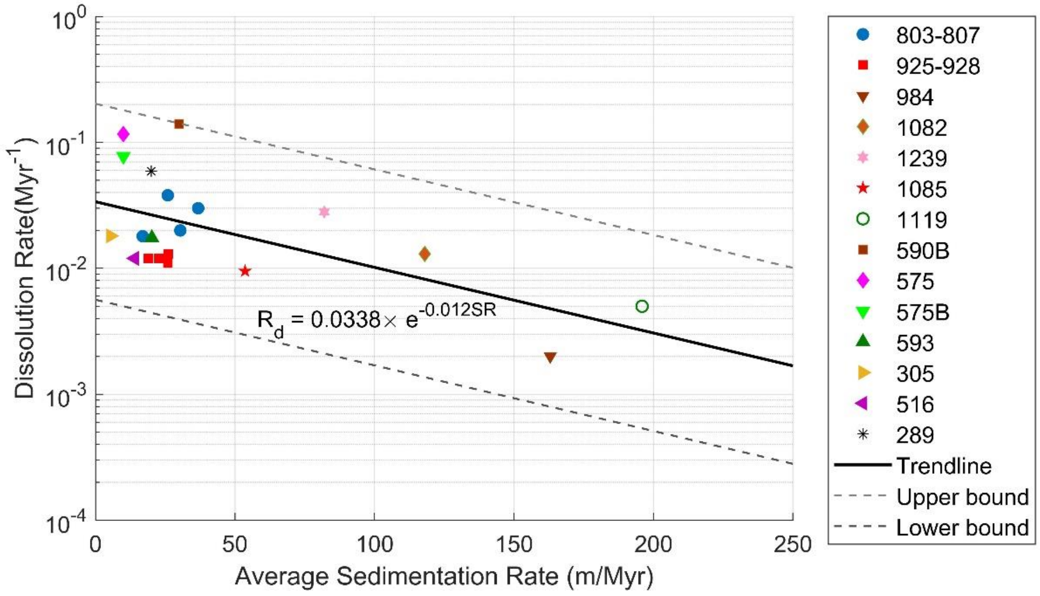

Fig. 6.6 Relationship between dissolution rate (Myr^{-1}) and average sedimentation rate (m/Myr).

6.3 Discussion and conclusions

This study models the Sr and Ca exchange processes in the deep-sea carbonate sediments with respect to the rates of dissolution and precipitation. The calcite recrystallization rates are large at the top of sediments ant dramatically decreased with depth or the age of the sediments. Also, our coupled numerical models of chemical compaction in four calcite cores (Sites 803, 805, 806 and 807) indicate that chemical compaction could contribute significantly to total porosity loss, in some cases even more than mechanical compaction does. Previous studies attempt to divide the carbonate core into shallow and deep sections and to identify the dominant compaction process for each section. We believe that both mechanical and chemical compaction contributes significantly to porosity reduction throughout the core and their relative fractions change smoothly with depth. Neither process is too small to be ignored in either shallow or deep sections. This conclusion is drawn mainly based on numerical modeling of pore fluid Sr and other components, which provide constraints on the recrystallization rates of calcite. Potentially this can be compared with petrographical studies, if available, where the fraction of authigenic carbonate can be measured.

In addition, by matching the chemical profiles of Sr and Ca, this numerical model can calculate the calcite dissolution rate in other more sites with various sedimentation conditions. Combined with other data in previous studies, the study could shed some insight for the general relationship between the calcite dissolution rate at the top of sediments and sedimentation conditions. It can be summarized as follows: the sites with higher carbonate content would have higher diagenetic potential; the sites with quicker sedimentation rate usually have lower dissolution rate. The regression results could be used to make reasonable prediction of calcite recrystallization prediction when the sedimentation conditions are known.

There are some ideas I would like to point out for the future study: 1). Experimental work would be helpful to support our numerical simulations. The fractions of authigenic and secondary carbonate from experimental measurements would be the direct evidence for the study in this area. 2). To draw a convincing conclusion of the quantitate relationship between the sedimentation conditions and the calcite dissolution rates at the top of sediments, more data points would be helpful.

REFERENCES

Algeo, T.J., Luo, G.M., Song, H.Y., Lyons, T.W., Canfield, D.E., 2015. Reconstruction of secular variation in seawater sulfate concentrations. Biogeosciences 12, 2131-2151.

Antonelli, M.A., Pester, N.J., Brown, S.T., DePaolo, D.J., 2017. Effect of paleoseawater composition on hydrothermal exchange in midocean ridges. Proc. Natl. Acad. Sci. U. S. A. 114, 12413-12418.

Baker, P.A., Gieskes, J.M., Elderfield, H., 1982. Diagenesis of Carbonates in Deep-Sea Sediments - Evidence from Sr/Ca Ratios and Interstitial Dissolved Sr2+ Data. Journal of Sedimentary Petrology 52, 71-82.

Barenblatt, G.I., Zheltov, I.P., 1960. Fundamental equations of filtration of homogeneous liquids in fissured rocks. Doklady Akademii Nauk Sssr 132, 545-548.

Bassinot, F., Marsters, J.C., Mayer, L.A., Wilkens, R.H., 1993. Variations of porosity in calcareous sediments from the Ontong Java Plateau.

Bathurst, R., 1970. Problems of lithification in carbonate muds. Proceedings of the Geologists' Association 81, 429-440.

Batu, V., Vangenuchten, M.T., 1990. 1st-Type and 3rd-Type Boundary-Conditions in 2-Dimensional Solute Transport Modeling. Water Resour. Res. 26, 339-350.

Bear, J., 1972. Dynamics of Fluids in Porous Media.

Benson, D.A., Wheatcraft, S.W., Meerschaert, M.M., 2000a. Application of a fractional advection-dispersion equation. Water Resour. Res. 36, 1403-1412.

Benson, D.A., Wheatcraft, S.W., Meerschaert, M.M., 2000b. The fractional - order governing equation of Lévy motion. Water Resour. Res. 36, 1413-1423.

Berkowitz, B., Cortis, A., Dror, I., Scher, H., 2009. Laboratory experiments on dispersive transport across interfaces: The role of flow direction. Water Resour. Res. 45.

Berkowitz, B., Kosakowski, G., Margolin, G., Scher, H., 2001. Application of continuous time random walk theory to tracer test measurements in fractured and heterogeneous porous media. Ground Water 39, 593-603.

Berkowitz, B., Scher, H., 1995. On Characterization of Anomalous Dispersion in Porous and Fractured Media. Water Resour. Res. 31, 1461-1466.

Berkowitz, B., Scher, H., 1997. Anomalous transport in random fracture networks. Phys. Rev. Lett. 79, 4038-4041.

Berkowitz, B., Scher, H., 1998. Theory of anomalous chemical transport in random fracture networks. Phys. Rev. E 57, 5858-5869.

Berner, R.A., 1980. Early diagenesis: a theoretical approach. Princeton University Press.

Bhattacharyya, A., Friedman, G.M., 1979. Experimental Compaction of Ooids and Lime Mud and Its Implication for Lithification during Burial. Journal of Sedimentary Petrology 49, 1279-1286.

Bjørlykke, K., Jahren, J., 2012. Open or closed geochemical systems during diagenesis in sedimentary basins: Constraints on mass transfer during diagenesis and the prediction of porosity in sandstone and carbonate reservoirs. AAPG bulletin 96, 2193-2214.

Bodin, J., Delay, F., de Marsily, G., 2003. Solute transport in a single fracture with negligible matrix permeability: 1. fundamental mechanisms. Hydrogeol. J. 11, 418-433.

Boudreau, B.P., 1997. Diagenetic models and their implementation. Springer Berlin.

Bradner, G.C., Murdoch, L.C., 2005. Effects of skin and hydraulic fractures on SVE wells. Journal of Contaminant Hydrology 77, 271-297.

Bromly, M., Hinz, C., Aylmore, L.A.G., 2007. Relation of dispersivity to properties of homogeneous saturated repacked soil columns. Eur. J. Soil Sci. 58, 293-301.

Brown, S., Caprihan, A., Hardy, R., 1998. Experimental observation of fluid flow channels in a single fracture. J Geophys Res-Sol Ea 103, 5125-5132.

Burns, E.R., Zhu, Y.H., Zhan, H.B., Manga, M., Williams, C.F., Ingebritsen, S.E., Dunham, J.B., 2017. Thermal effect of climate change on groundwater-fed ecosystems. Water Resour. Res. 53, 3341-3351.

Butters, G.L., Jury, W.A., 1989. Field Scale Transport of Bromide in an Unsaturated Soil .2. Dispersion Modeling. Water Resour. Res. 25, 1583-1589.

Caine, J.S., Evans, J.P., Forster, C.B., 1996. Fault zone architecture and permeability structure. Geology 24, 1025-1028.

Carrera, J., Sanchez-Vila, X., Benet, I., Medina, A., Galarza, G., Guimera, J., 1998. On matrix diffusion: formulations, solution methods and qualitative effects. Hydrogeol. J. 6, 178-190.

Chanda, S., Bhattacharyya, A., Sarkar, S., 1977. Deformation of ooids by compaction in the Precambrian Bhander Limestone, India: Implications for lithification. Geological Society of America Bulletin 88, 1577-1585.

Chen, C.S., 1986. Solutions for radionuclide transport from an injection well into a single fracture in a porous formation. Water Resour. Res. 22, 508-518.

Chen, C.S., 1987. Analytical solutions for radial dispersion with cauchy boundary at injection well. Water Resour. Res. 23, 1217-1224.

Chester, F.M., Logan, J.M., 1986. Implications for Mechanical-Properties of Brittle Faults from Observations of the Punchbowl Fault Zone, California. Pure Appl. Geophys. 124, 79-106.

Cipollari, P., Cosentino, D., 1995. Miocene unconformities in the central Apennines: Geodynamic significance and sedimentary basin evolution. Tectonophysics 252, 375-389.

Coggon, R.M., Teagle, D.A.H., 2011. Hydrothermal calcium-carbonate veins reveal past ocean chemistry. Trac-Trends Anal. Chem. 30, 1252-1268.

Coggon, R.M., Teagle, D.A.H., Smith-Duque, C.E., Alt, J.C., Cooper, M.J., 2010. Reconstructing Past Seawater Mg/Ca and Sr/Ca from Mid-Ocean Ridge Flank Calcium Carbonate Veins. Science 327, 1114-1117.

Cvetkovic, V., Painter, S., Outters, N., Selroos, J., 2004. Stochastic simulation of radionuclide migration in discretely fractured rock near the Äspö Hard Rock Laboratory. Water Resour. Res. 40.

Cvetkovic, V., Selroos, J., Cheng, H., 1999. Transport of reactive tracers in rock fractures. J. Fluid Mech. 378, 335-356.

Davis, G.B., Laslett, D., Patterson, B.M., Johnston, C.D., 2013. Integrating spatial and temporal oxygen data to improve the quantification of in situ petroleum biodegradation rates. Journal of Environmental Management 117, 42-49.

De Hoog, F.R., Knight, J., Stokes, A., 1982. An improved method for numerical inversion of Laplace transforms. Siam J Sci Stat Comp 3, 357-366.

De La Rocha, C.L., DePaolo, D.J., 2000. Isotopic evidence for variations in the marine calcium cycle over the cenozoic. Science 289, 1176-1178.

Delaney, M.L., 1989. Temporal Changes in Interstitial Water Chemistry and Calcite Recrystallization in Marine-Sediments. Earth and Planetary Science Letters 95, 23-37.

Delaney, M.L., Be, A.W.H., Boyle, E.A., 1985. Li, Sr, Mg, and Na in Foraminiferal Calcite Shells from Laboratory Culture, Sediment Traps, and Sediment Cores. Geochimica Et Cosmochimica Acta 49, 1327-1341.

DePaolo, D.J., 2011. Surface kinetic model for isotopic and trace element fractionation during precipitation of calcite from aqueous solutions. Geochimica Et Cosmochimica Acta 75, 1039-1056.

Dershowitz, W., Miller, I., 1995. Dual porosity fracture flow and transport. Geophysical Research Letters 22, 1441-1444.

Dronfield, D.G., Silliman, S.E., 1993. Velocity dependence of dispersion for transport through a single fracture of variable roughness. Water Resour. Res. 29, 3477-3483.

Elderfield, H., Cooper, M., Ganssen, G., 2000. Sr/Ca in multiple species of planktonic foraminifera: Implications for reconstructions of seawater Sr/Ca. Geochemistry, Geophysics, Geosystems 1.

Elderfield, H., Schultz, A., 1996. Mid-ocean ridge hydrothermal fluxes and the chemical composition of the ocean. Annual Review of Earth and Planetary Sciences 24, 191-224.

Esposito, S.J., Thomson, N.R., 1999. Two-phase flow and transport in a single fracture-porous medium system. Journal of Contaminant Hydrology 37, 319-341.

Fantle, M.S., 2015. Calcium isotopic evidence for rapid recrystallization of bulk marine carbonates and implications for geochemical proxies. Geochimica Et Cosmochimica Acta 148, 378-401.

Fantle, M.S., DePaolo, D.J., 2005. Variations in the marine Ca cycle over the past 20 million years. Earth and Planetary Science Letters 237, 102-117.

Fantle, M.S., DePaolo, D.J., 2006. Sr isotopes and pore fluid chemistry in carbonate sediment of the Ontong Java Plateau: Calcite recrystallization rates and evidence for a rapid rise in seawater Mg over the last 10 million years. Geochimica Et Cosmochimica Acta 70, 3883-3904.

Fantle, M.S., DePaolo, D.J., 2007. Ca isotopes in carbonate sediment and pore fluid from ODP Site 807A: The Ca2+(aq)-calcite equilibrium fractionation factor and calcite recrystallization rates in Pleistocene sediments. Geochimica Et Cosmochimica Acta 71, 2524-2546.

Freeze, R.A., Cherry, J.A., 1979. Groundwater. Prentice-Hall, Englewood Cliffs, NJ.

Furman, A., Neuman, S.P., 2003. Laplace-transform analytic element solution of transient flow in porous media. Advances in Water Resources 26, 1229-1237.

Gao, G.Y., Zhan, H.B., Feng, S.Y., Fu, B.J., Ma, Y., Huang, G.H., 2010. A new mobile-immobile model for reactive solute transport with scale-dependent dispersion. Water Resour. Res. 46.

Gelhar, L.W., 1986. Stochastic subsurface hydrology from theory to applications. Water Resour. Res. 22, S135-S145.

Gelhar, L.W., Gutjahr, A.L., Naff, R.L., 1979. Stochastic-Analysis of Macrodispersion in a Stratified Aquifer. Water Resour. Res. 15, 1387-1397.

Gelhar, L.W., Welty, C., Rehfeldt, K.R., 1992. A critical review of data on field-scale dispersion in aquifers. Water Resour. Res. 28, 1955-1974.

Golubev, V.S., Garibyants, A.A., 1971. Diffusion in Rocks, Heterogeneous Processes of Geochemical Migration. Springer US, Boston, MA, pp. 13-43.

Graham, D.W., Bender, M.L., Williams, D.F., Keigwin, L.D., 1982. Strontium-Calcium Ratios in Cenozoic Planktonic-Foraminifera. Geochimica Et Cosmochimica Acta 46, 1281-1292.

Grisak, G.E., Pickens, J.F., 1981. An analytical solution for solute transport through fractured media with matrix diffusion. Journal of Hydrology 52, 47-57.

Guven, O., Molz, F.J., Melville, J.G., 1984. An Analysis of Dispersion in a Stratified Aquifer. Water Resour. Res. 20, 1337-1354.

Hamilton, E.L., 1971. Prediction of in-situ acoustic and elastic properties of marine sediments. Geophysics 36, 266-&.

Hampt, G., Delaney, M.L., 1997. Influences on calcite Sr/Ca records from Ceara Rise and other regions: distinguishing ocean history and calcite recrystallization, Proc. ODP, Sci. Results. Ocean Drilling Program College Station, TX, pp. 491-500.

Huang, K., Toride, N., Vangenuchten, M.T., 1995. Experimental Investigation of Solute Transport in Large, Homogeneous and Heterogeneous, Saturated Soil Columns. Transport in Porous Media 18, 283-302.

Huang, Y.C., Yeh, H.D., 2007. The use of sensitivity analysis in on-line aquifer parameter estimation. Journal of Hydrology 335, 406-418.

Jodar, J., Medina, A., Carrera, J., 2009. Gas tracer transport through a heterogeneous fracture zone under two phase flow conditions: Model development and parameter sensitivity. Advances in Water Resources 32, 315-328.

Johnson, C.A., Furrer, G., 2002. Influence of biodegradation processes on the duration of CaCO3 as a pH buffer in municipal solid waste incinerator bottom ash. Environmental Science & Technology 36, 215-220.

Joshi, N., Ojha, C.S.P., Sharma, P.K., Madramootoo, C.A., 2015. Application of nonequilibrium fracture matrix model in simulating reactive contaminant transport through fractured porous media. Water Resour. Res. 51, 390-408.

Jury, W.A., Stolzy, L.H., Shouse, P., 1982. A Field-Test of the Transfer-Function Model for Predicting Solute Transport. Water Resour. Res. 18, 369-375.

Kabala, Z.J., 2001. Sensitivity analysis of a pumping test on a well with wellbore storage and skin. Advances in Water Resources 24, 483-504.

Kroenke, L.W., Berger, W.H., Janecek, T.R., et al.,, 1991. Proc. ODP, Init. Repts., 130. 130, 369–493.

Latour, L.L., Svoboda, K., Mitra, P.P., Sotak, C.H., 1994. Time-dependent diffusion of water in a biological model system. Proc. Natl. Acad. Sci. U. S. A. 91, 1229-1233.

Lear, C.H., Elderfield, H., Wilson, P.A., 2003. A Cenozoic seawater Sr/Ca record from benthic foraminiferal calcite and its application in determining global weathering fluxes. Earth and Planetary Science Letters 208, 69-84.

Leij, F.J., Dane, J.H., Vangenuchten, M.T., 1991. Mathematical-analysis of one-dimensional solute transport in a layered soil-profile. Soil Science Society of America Journal 55, 944-953.

Logan, J.D., 1996. Solute transport in porous media with scale-dependent dispersion and periodic boundary conditions. Journal of Hydrology 184, 261-276.

Long, J.C.S., Billaux, D.M., 1987. From field data to fracture network modeling - an example incorporating spatial structure. Water Resour. Res. 23, 1201-1216.

Lunati, I., Kinzelbach, W., Sørensen, I., 2003. Effects of pore volume–transmissivity correlation on transport phenomena. Journal of Contaminant Hydrology 67, 195-217.

Maloszewski, P., Zuber, A., 1990. Mathematical modeling of tracer behavior in short-term experiments in fissured rocks. Water Resour. Res. 26, 1517-1528.

Maloszewski, P., Zuber, A., 1993. Tracer experiments in fractured rocks - matrix diffusion and the validity of models. Water Resour. Res. 29, 2723-2735.

Marseguerra, M., Zoia, A., 2006. Normal and anomalous transport across an interface: Monte Carlo and analytical approach. Annals of Nuclear Energy 33, 1396-1407.

Martin, P.A., Lea, D.W., Mashiotta, T.A., Papenfuss, T., Sarnthein, M., 1999. Variation of foraminiferal Sr/Ca over Quaternary glacial-interglacial cycles: Evidence for changes in mean ocean Sr/Ca? Geochem. Geophys. Geosyst. 1, 19.

Matter, A., 1974. Burial diagenesis of pelitic and carbonate deep-sea sediments from the Arabian Sea. Initial Reports of the Deep Sea Drilling Project 23, 421-469.

Morales-Casique, E., Neuman, S.P., Guadagnini, A., 2006. Non-local and localized analyses of non-reactive solute transport in bounded randomly heterogeneous porous media: Theoretical framework. Advances in Water Resources 29, 1238-1255.

Moreno, L., Tsang, Y.W., Tsang, C.F., Hale, F.V., Neretnieks, I., 1988. Flow and tracer transport in a single fracture - a stochastic-model and its relation to some field observations. Water Resour. Res. 24, 2033-2048.

Morse, J.W., Bender, M.L., 1990. Partition coefficients in calcite: Examination of factors influencing the validity of experimental results and their application to natural systems. Chemical Geology 82, 265-277.

Neuman, S.P., 1990. Universal Scaling of Hydraulic Conductivities and Dispersivities in Geologic Media. Water Resour. Res. 26, 1749-1758.

Noetinger, B., Roubinet, D., Russian, A., Le Borgne, T., Delay, F., Dentz, M., De Dreuzy, J.-R., Gouze, P., 2016. Random walk methods for modeling hydrodynamic transport in porous and fractured media from pore to reservoir scale. Transport in Porous Media, 1-41.

Olayinka, S., Ioannidis, M.A., 2004. Time-dependent diffusion and surface-enhanced relaxation in stochastic replicas of porous rock. Transport in Porous Media 54, 273-295.

Pang, L.P., Hunt, B., 2001. Solutions and verification of a scale-dependent dispersion model. Journal of Contaminant Hydrology 53, 21-39.

Parker, J.C., Valocchi, A.J., 1986. Constraints on the validity of equilibrium and first‐order kinetic transport models in structured soils. Water Resour. Res. 22, 399-407.

Pickens, J.F., Grisak, G.E., 1981a. Modeling of Scale-Dependent Dispersion in Hydrogeologic Systems. Water Resour. Res. 17, 1701-1711.

Pickens, J.F., Grisak, G.E., 1981b. Scale-dependent dispersion in a stratified granular aquifer. Water Resour. Res. 17, 1191-1211.

Porro, I., Wierenga, P.J., Hills, R.G., 1993. Solute Transport through Large Uniform and Layered Soil Columns. Water Resour. Res. 29, 1321-1330.

Pouya, A., 2012. Three-dimensional flow in fractured porous media: A potential solution based on singular integral equations. Advances in Water Resources 35, 30-40.

Qian, J.Z., Chen, Z., Zhan, H.B., Luo, S.H., 2011. Solute transport in a filled single fracture under non-Darcian flow. International Journal of Rock Mechanics and Mining Sciences 48, 132-140.

Qian, J.Z., Zhan, H.B., Zhao, W.D., Sun, F.G., 2005. Experimental study of turbulent unconfined groundwater flow in a single fracture. Journal of Hydrology 311, 134-142.

Raven, K.G., Novakowski, K.S., Lapcevic, P.A., 1988. Interpretation of field tracer tests of a single fracture using a transient solute storage model. Water Resour. Res. 24, 2019-2032.

Reynaud, O., 2017. Time-Dependent Diffusion MRI in Cancer: Tissue Modeling and Applications. Front. Physics 5, 16.

Rezaei, A., Zare, M., Zhan, H., 2016. Aquitard horizontal dispersion on reactive solute transport in an aquifer–aquitard system. Transport in Porous Media 113, 695-716.

Richter, F.M., 1993. Fluid flow in deep-sea carbonates: estimates based on porewater Sr. Earth and Planetary Science Letters 119, 133-141.

Richter, F.M., 1996. Models for the coupled Sr-sulfate budget in deep-sea carbonates. Earth and Planetary Science Letters 141, 199-211.

Richter, F.M., Depaolo, D.J., 1987. Numerical models for diagenesis and the Neogene Sr isotopic evolution

of seawater from DSDP Site 590B. Earth and Planetary Science Letters 83, 27-38.

Richter, F.M., Depaolo, D.J., 1988. Diagenesis and Sr isotopic evolution of seawater using data from DSDP 590B and 575. Earth and Planetary Science Letters 90, 382-394.

Richter, F.M., Liang, Y., 1993. The rate and consequences of Sr diagenesis in deep-sea carbonates. Earth and Planetary Science Letters 117, 553-565.

Roubinet, D., de Dreuzy, J.R., Tartakovsky, D.M., 2012. Semi-analytical solutions for solute transport and exchange in fractured porous media. Water Resour. Res. 48.

Sawyer, D.S., Bangs, N.L., Golovchenko, X., 1994. Deconvolving Ocean Drilling Program Temperature Logging Tool Data to Improve Borehole Temperature Estimates - Chile Triple Junction. J Geophys Res-Sol Ea 99, 11995-12003.

Schlanger, S.O., Douglas, R.G., 1974. The pelagic ooze-chalk-limestone transition and its implications for marine stratigraphy, Pelagic Sediments: on Land and under the Sea. Blackwell Scientific Publications Oxfort, London, Edingburh, Melbourne, pp. 117-148.

Schulze-Makuch, D., 2005. Longitudinal dispersivity data and implications for scaling behavior. Ground Water 43, 443-456.

Schumer, R., Benson, D.A., Meerschaert, M.M., Baeumer, B., 2003. Fractal mobile/immobile solute transport. Water Resour. Res. 39.

Sen, P.N., 2004. Time-dependent diffusion coefficient as a probe of geometry. Concepts Magn. Reson. Part A 23A, 1-21.

Seo, J.H., Mittal, R., 2011. A sharp-interface immersed boundary method with improved mass conservation and reduced spurious pressure oscillations. Journal of Computational Physics 230, 7347-7363.

Shackleton, N., 1967. Oxygen Isotope Analyses and Pleistocene Temperatures Re-Assessed. Nature 215, 15-+.

Shinn, E.A., Halley, R.B., Hudson, J.H., Lidz, B.H., 1977. Limestone compaction: an enigma. Geology 5, 21-24.

Simmons, C.T., Fenstemaker, T.R., Sharp, J.M., Jr., 2001. Variable-density groundwater flow and solute transport in heterogeneous porous media: approaches, resolutions and future challenges. Journal of Contaminant Hydrology 52, 245-275.

Starr, R.C., Gillham, R.W., Sudicky, E.A., 1985. Experimental Investigation of Solute Transport in Stratified Porous-Media .2. The Reactive Case. Water Resour. Res. 21, 1043-1050.

Stoll, H.M., Schrag, D.P., 1998. Effects of Quaternary sea level cycles on strontium in seawater. Geochimica Et Cosmochimica Acta 62, 1107-1118.

Sudicky, E.A., Frind, E.O., 1982. Contaminant transport in fractured porous media: Analytical solutions for a system of parallel fractures. Water Resour. Res. 18, 1634-1642.

Sudicky, E.A., Gillham, R.W., Frind, E.O., 1985. Experimental Investigation of Solute Transport in Stratified Porous-Media .1. The Nonreactive Case. Water Resour. Res. 21, 1035-1041.

Swami, D., Sharma, A., Sharma, P.K., Shukla, D.P., 2016. Predicting suitability of different scale-dependent dispersivities for reactive solute transport through stratified porous media. J. Rock Mech. Geotech. Eng. 8, 921-927.

Swami, D., Sharma, P.K., Ojha, C.S.P., 2014. Simulation of experimental breakthrough curves using multiprocess non-equilibrium model for reactive solute transport in stratified porous media. Sadhana-Acad. Proc. Eng. Sci. 39, 1425-1446.

Tang, D.H., Frind, E.O., Sudicky, E.A., 1981. Contaminant transport in fractured porous-media - analytical solution for a single fracture. Water Resour. Res. 17, 555-564.

Turchyn, A.V., DePaolo, D.J., 2011. Calcium isotope evidence for suppression of carbonate dissolution in carbonate-bearing organic-rich sediments. Geochimica Et Cosmochimica Acta 75, 7081-7098.

Van Genuchten, M.T., Wierenga, P.J., 1976. Mass transfer studies in sorbing porous media I. Analytical solutions. Soil Science Society of America Journal 40, 473-480.

Vanderborght, J., Vereecken, H., 2007. Review of dispersivities for transport modeling in soils. Vadose Zone J. 6, 29-52.

Vangenuchten, M.T., Parker, J.C., 1984. Boundary-Conditions for Displacement Experiments through Short Laboratory Soil Columns. Soil Science Society of America Journal 48, 703-708.

Wang, Q.R., Zhan, H.B., 2015. On different numerical inverse Laplace methods for solute transport problems. Advances in Water Resources 75, 80-92.

Wealthall, G.P., Steele, A., Bloomfield, J.P., Moss, R.H., Lerner, D.N., 2001. Sediment filled fractures in the Permo-Triassic sandstones of the Cheshire basin: observations and implications for pollutant transport. Journal of Contaminant Hydrology 50, 41-51.

Weatherill, D., Graf, T., Simmons, C.T., Cook, P.G., Therrien, R., Reynolds, D.A., 2008. Discretizing the fracture-matrix interface to simulate solute transport. Ground Water 46, 606-615.

Weller, J.M., 1959. Compaction of sediments. AAPG Bulletin 43, 273-310.

Wetzel, A., 1989. Influence of Heat-Flow on Ooze Chalk Cementation - Quantification from Consolidation Parameters in Dsdp Sites 504 and 505 Sediments. Journal of Sedimentary Petrology 59, 539-547.

Wheatcraft, S.W., Tyler, S.W., 1988. An explanation of scale-dependent dispersivity in heterogeneous aquifers using concepts of fractal geometry. Water Resour. Res. 24, 566-578.

Wierenga, P.J., Vangenuchten, M.T., 1989. Solute transport through small and large unsaturated soil columns. Ground Water 27, 35-42.

Wilkinson, B.H., Algeo, T.J., 1989. Sedimentary Carbonate Record of Calcium Magnesium Cycling. Am. J. Sci. 289, 1158-1194.

Wilson, C.R., Witherspoon, P.A., 1970. An investigation of laminar flow in fractured porous rocks. Department of Civil Engineering, University of California.

Xu, S.L., Worman, A., Dverstorp, B., 2001. Heterogeneous matrix diffusion in crystalline rock - implications for geosphere retardation of migrating radionuclides. Journal of Contaminant Hydrology 47, 365-378.

Yates, S.R., 1990. An analytical solution for one-dimensional transport in heterogeneous porous media. Water Resour. Res. 26, 2331-2338.

Yates, S.R., 1992. An analytical solution for one-dimensional transport in porous media with an exponential dispersion function. Water Resour. Res. 28, 2149-2154.

You, K.H., Zhan, H.B., 2013. New solutions for solute transport in a finite column with distance-dependent dispersivities and time-dependent solute sources. Journal of Hydrology 487, 87-97.

Zech, A., Attinger, S., Cvetkovic, V., Dagan, G., Dietrich, P., Fiori, A., Rubin, Y., Teutsch, G., 2015. Is unique scaling of aquifer macrodispersivity supported by field data? Water Resour. Res. 51, 7662-7679.

Zhan, H., Wen, Z., Huang, G., Sun, D., 2009a. Analytical solution of two-dimensional solute transport in an aquifer-aquitard system. Journal of Contaminant Hydrology 107, 162-174.

Zhan, H.B., Bian, A.G., 2006. A method of calculating pumping induced leakage. Journal of Hydrology 328, 659-667.

Zhan, H.B., Wen, Z., Gao, G.Y., 2009b. An analytical solution of two-dimensional reactive solute transport in an aquifer-aquitard system. Water Resour. Res. 45, 8.

Zhang, X.X., Qi, X.B., Qiao, D.M., 2010. Change in macroscopic concentration at the interface between different materials: Continuous or discontinuous. Water Resour. Res. 46.

Zhou, R.J., Zhan, H.B., 2018. Reactive solute transport in an asymmetrical fracture–rock matrix system. Advances in Water Resources 112, 224-234.

Zhou, R.J., Zhan, H.B., Chen, K.W., 2017. Reactive solute transport in a filled single fracture-matrix system under unilateral and radial flows. Advances in Water Resources 104, 183-194.

Zhu, Y.H., Zhan, H.B., Jin, M.G., 2016. Analytical solutions of solute transport in a fracture-matrix system with different reaction rates for fracture and matrix. Journal of Hydrology 539, 447-456.

Zimmerman, R., Sassen, R., 1993. Hydrocarbon transfer pathways from Smackover source rocks to younger reservoir traps in the Monroe Gas Field, northeast Louisiana. GCAGS Transactions 43, 473-480.

APPENDIX A

DERIVATION OF REACTIVE SOLUTE TRANSPORT IN A FILLED SINGLE FRACTURE SYSTEM UNDER UNILATERAL FLOW

The governing equations of reactive solute transport in the mobile and immobile domains of filled fracture and rock matrix in Eqs.2.1-2.3 should be transformed in dimensionless formats. The dimensionless variables used in the study of the unilateral flow model are as follows:

$$\mathrm{C_{mD}} = \frac{C_m}{C_0};\ \mathrm{C_{imD}} = \frac{C_{im}}{C_0};\ \mathrm{C_{kD}} = \frac{C_k}{C_0};\ \mathrm{x_D} = \frac{x}{b};\ \mathrm{z_D} = \frac{z}{b}\sqrt{\frac{R_3 D_m}{R_1 D_d}};\ \mathrm{t_D} = \frac{D_m}{R_1 b^2} t;\ \mathrm{Pe} = \frac{v_m b}{D_m}$$

$$\theta_1 = \theta_{im}/\theta_m;\ \theta_2 = \theta_k/\theta_m;\ \alpha = \frac{R_1 b^2}{D_m};\ \alpha_1 = \theta_2\sqrt{\frac{R_3 D_d}{R_1 D_m}};\ M'_{fmD} = \frac{M'_{fm}}{C_0 b^2\sqrt{\frac{R_1 D_d}{R_3 D_m}}};\ M'_{fimD} =$$

$$\frac{M'_{fim}}{C_0 b^2\sqrt{\frac{R_1 D_d}{R_3 D_m}}};\ M'_{kD} = \frac{M'_{k}}{C_0 b^2\sqrt{\frac{R_1 D_d}{R_3 D_m}}}.$$

In the unilateral flow model, the non-dimensional governing equations (Eqs. (2.1)-(2.3)) now are transformed to their dimensionless formats of Eqs. (A1)-(A3):

$$\frac{\partial C_{mD}}{\partial t_D} + \frac{\theta_1 R_2}{R_1}\frac{\partial C_{imD}}{\partial t_D} = \frac{\partial^2 C_{mD}}{\partial x_D^2} - Pe\frac{\partial C_{mD}}{\partial x_D} - \lambda_1 \alpha C_{mD} - \lambda_2 \theta_1 \alpha \frac{R_2}{R_1} C_{im} + \alpha_1 \left.\frac{\partial C_{kD}}{\partial z_D}\right|_{z_D=\sqrt{\frac{R_3 D_m}{R_1 D_d}}}, \quad \text{(A.1)}$$

$$\frac{\partial C_{imD}}{\partial t_D} = \frac{\omega\alpha}{\theta_{im} R_2}\left(C_{mD} - C_{imD}\right) - \lambda_2 \alpha C_{imD}, \quad \text{(A.2)}$$

$$\frac{\partial C_{kD}}{\partial t_D} = \frac{\partial^2 C_{kD}}{\partial z_D^2} - \lambda_3 \alpha C_{kD}. \quad \text{(A.3)}$$

Applying Laplace transform to Eqs. (A.1)-(A.3) would lead to the following equations:

$$p\overline{C_{mD}} + p\frac{\theta_1 R_2}{R_1}\overline{C_{imD}} = \frac{d^2\overline{C_{mD}}}{dx_D^2} - Pe\frac{d\overline{C_{mD}}}{dx_D} - \lambda_1\alpha\overline{C_{mD}} - \lambda_2\theta_1\alpha\frac{R_2}{R_1}\overline{C_{imD}} + \alpha_1\left.\frac{d\overline{C_{kD}}}{dz_D}\right|_{z_D=\sqrt{\frac{R_3D_m}{R_1D_d}}} \quad , \tag{A.4}$$

$$p\overline{C_{imD}} = \frac{\omega\alpha}{\theta_{im}R_2}\left(\overline{C_{mD}} - \overline{C_{imD}}\right) - \lambda_2\alpha\overline{C_{imD}} \, , \tag{A.5}$$

$$p\overline{C_{kD}} = \frac{d^2\overline{C_{kD}}}{dz_D^2} - \lambda_3\alpha\overline{C_{kD}} \, , \tag{A.6}$$

where p is the Laplace transform parameter in respect to the dimensionless time, t_D and overbar means the term in Laplace domain. From Eq. (A.6), one has

$$\frac{d^2\overline{C_{kD}}}{dz_D^2} = \left(\lambda_3\alpha + p\right)\overline{C_{kD}} \quad , \tag{A.7}$$

The general solution of Eq. (A.7) is

$$\overline{C_{kD}} = Ae^{wz_D} + Be^{-wz_D} \, , \tag{A.8}$$

where $w = \sqrt{\lambda_3\alpha + p}$.

Recalling boundary condition of rock matrix at infinity (Eq. (2.11)), Eq. (A.8) can be simplified as:

$$\overline{C_{kD}} = Be^{-wz_D} \ . \tag{A.9}$$

Substituting Eq. (A.9) to Eq. (A.6), one can get the following relation:

$$\overline{C_{mD}} = \left.\overline{C_{kD}}\right|_{z_D=\sqrt{\frac{R_3D_m}{R_1D_d}}} \, , \tag{A.10}$$

$$B = \overline{C_{mD}}e^{\sqrt{\lambda_3\alpha+p}\sqrt{\frac{R_3D_m}{R_1D_d}}} \ . \tag{A.11}$$

Now one has the relation between $\overline{C_{kD}}$ and $\overline{C_{mD}}$:

$$\overline{C_{kD}} = \overline{C_{mD}} e^{\sqrt{\lambda_3 \alpha + p}\left(\sqrt{\frac{R_3 D_m}{R_1 D_d}} - z_D\right)} . \tag{A.12}$$

Based on Eq. (A.5), the relation between $\overline{C_{mD}}$ and $\overline{C_{imD}}$ is demonstrated:

$$\overline{C_{imD}} = \frac{\omega}{\frac{\theta_{im} R_2 p}{\alpha} + \omega + \lambda_2 \theta_{im} R_2} \overline{C_{mD}} . \tag{A.13}$$

Substituting Eqs. (A.12)-(A.13) into Eq. (A.4), the final solutions will be reached in the Laplace domain.

Converting M'_{fm}, M'_{fim} and M'_{k} in Eqs. (2.30)-(2.32) into their dimensionless forms defined above, the dimensionless mass per unit width stored in the fracture-rock matrix system of unilateral flow is given as:

$$M'_{fmD} = 2\theta_m \sqrt{\frac{R_3 D_m}{R_1 D_d}} \int_0^\infty C_{mD} \, dx_D \ , \tag{A.14}$$

$$M'_{fimD} = 2\theta_{im} \sqrt{\frac{R_3 D_m}{R_1 D_d}} \int_0^\infty C_{imD} dx_D \ , \tag{A.15}$$

$$M'_{kD} = 2\theta_k \int_{\sqrt{\frac{R_3 D_m}{R_1 D_d}}}^\infty \int_0^\infty C_{kD} \, dx_D \, dz_D . \tag{A.16}$$

APPENDIX B

DERIVATION OF REACTIVE SOLUTE TRANSPORT IN A FILLED SINGLE FRACTURE SYSTEM UNDER RADIAL FLOW

The governing equations (Eqs. (2.20)-(2.21)) are transformed to dimensionless formats. The dimensionless variables used in the study of the radial flow model are defined as follows:

$C_{mD} = \frac{C_m}{C_0}$; $C_{imD} = \frac{C_{im}}{C_0}$; $C_{kD} = \frac{C_k}{C_0}$; $t_D = \frac{At}{R_1 d^2}$; $r_D = \frac{r}{d}$; $z_D = \left(\frac{z}{d}\right)\sqrt{\frac{R_3 A}{R_1 D_d}}$; $\tau_1 = \frac{\theta_2 d}{b}\sqrt{\frac{R_3 D_d}{R_1 A}}$; $\tau = \frac{d^2 R_1}{A}$; $\theta_1 = \theta_{im}/\theta_m$; $\theta_2 = \theta_k/\theta_m$; $M_{fmD} = \frac{M_{fm}}{C_0 d^3\sqrt{\frac{R_1 D_d}{R_3 A}}}$; $M_{fimD} = \frac{M_{fim}}{C_0 d^3\sqrt{\frac{R_1 D_d}{R_3 A}}}$; $M_{kD} = \frac{M_k}{C_0 d^3\sqrt{\frac{R_1 D_d}{R_3 A}}}$.

Converting the system into the dimensionless format, as done for the unilateral flow model, with details provided above, one has:

$$\begin{aligned}\frac{\partial C_{mD}}{\partial t_D} + \frac{\theta_1 R_2}{R_1}\left(\frac{\partial C_{imD}}{\partial t_D}\right) &= \frac{1}{r_D}\left(\frac{\partial^2 C_{mD}}{\partial r_D^2}\right) - \frac{1}{r_D}\left(\frac{\partial C_{mD}}{\partial r_D}\right) \\ &\quad -\lambda_1 \tau C_{mD} - \theta_1 \lambda_2 \frac{R_2}{R_1}\tau C_{imD} + \tau_1 \left(\frac{\partial C_{kD}}{\partial z_D}\right)\Bigg|_{z_D = b/d\sqrt{\frac{R_3 A}{R_1 D_d}}},\end{aligned} \tag{B.1}$$

$$\frac{\partial C_{imD}}{\partial t_D} = \frac{\omega \tau}{\theta_{im} R_2}\left(C_{mD} - C_{imD}\right) - \lambda_2 \tau C_{imD}, \tag{B.2}$$

$$\frac{\partial^2 C_{kD}}{\partial z_D^2} - \frac{\partial C_{kD}}{\partial t_D} - \tau \lambda_3 C_{kD} = 0. \tag{B.3}$$

Applying the Laplace transform to Eqs. (B.1)-(B.3) would yield to the following equations in the Laplace domain:

$$p\overline{C_{mD}}+\theta_1\lambda_2\frac{R_2}{R_1}\tau\overline{C_{imD}}+\frac{\theta_1 pR_2}{R_1}\overline{C_{imD}}=\frac{1}{r_D}\left(\frac{d^2\overline{C_{mD}}}{dr_D^2}\right)-\frac{1}{r_D}\left(\frac{d\overline{C_{mD}}}{dr_D}\right)$$
$$-\lambda_1\tau\overline{C_{mD}}+\tau_1\left(\frac{\partial\overline{C_{kD}}}{\partial z_D}\right)\Bigg|_{z_D=b/d\sqrt{\frac{R_3A}{R_1D_d}}} , \tag{B.4}$$

$$p\overline{C_{imD}}=\frac{\omega\tau}{\theta_{im}R_2}\left(\overline{C_{mD}}-\overline{C_{imD}}\right)-\lambda_2\tau\overline{C_{imD}} , \tag{B.5}$$

$$\frac{\partial^2\overline{C_{kD}}}{\partial z_D^2}-\bar{C}_{kD}\,p-\tau\lambda_3\overline{C_{kD}}=0 . \tag{B.6}$$

From Eq. (B.6), we have:

$$\overline{C_{kD}}=a\times exp\left(-\sqrt{\tau\lambda_3+p}\,z_D\right) . \tag{B.7}$$

At the interacting surface between the rock matrix and fracture:

$$\overline{C_{mD}}\left(r_D,p\right)=\overline{C_{kD}}\left(z_D=b/d\sqrt{\frac{R_3A}{R_1D_d}},p\right)=a\times\exp\left(-\sqrt{\tau\lambda_3+p}\times b/d\sqrt{\frac{R_3A}{R_1D_d}}\right). \tag{B.8}$$

So *a* can be solved as follow:

$$a=\overline{C_{mD}}exp\left(\sqrt{\tau\lambda_3+p}\times b/d\sqrt{\frac{R_3A}{R_1D_d}}\right) . \tag{B.9}$$

Substituting Eq. (B.9) into Eq. (B.7), the relationship between $\overline{C_{kD}}$ and $\overline{C_{mD}}$ can be reached:

$$\overline{C_{kD}}=\overline{C_{mD}}\exp\left[-\sqrt{\tau\lambda_3+p}\left(z_D-b/d\sqrt{\frac{R_3A}{R_1D_d}}\right)\right] . \tag{B.10}$$

From Eq. (B.5), the relation between $\overline{C_{imD}}$ and $\overline{C_{mD}}$ is as follow:

$$\overline{C_{imD}} = \frac{\omega}{\frac{\theta_{im} p R_2}{\tau} + \omega + \lambda_2 \theta_{im} R_2} \overline{C_{mD}} \quad . \tag{B.11}$$

Substituting Eqs. (B.10)-(B.11) to Eq. (B.4):

$$\frac{\partial^2 \overline{C_{mD}}}{\partial r_D^2} - \frac{\partial \overline{C_{mD}}}{\partial r_D} - r_D \beta \overline{C_{mD}} = 0 \, , \tag{B.12}$$

$$\text{where } \beta = \left(\tau\lambda_1 + \tau_1 \sqrt{\tau\lambda_3 + p} + p + \frac{R_2}{R_1} \times \frac{(p + \lambda_2 \tau)\theta_1 \omega}{\frac{\theta_{im} p R_2}{\tau} + \omega + \lambda_2 \theta_{im} R_2} \right).$$

The Eq. (B.12) is an inhomogeneous differential equation. The general solution is

$$\overline{C_{mD}} = A_1 \times \exp\left(\frac{y}{2}\right) Ai\left(\beta^{\frac{1}{3}} y\right) + A_2 \times \exp\left(\frac{y}{2}\right) Bi\left(\beta^{\frac{1}{3}} y\right), \tag{B.13}$$

where $\mathrm{y} = \mathrm{r}_D + (4\beta)^{-1}$.

Since $Bi(\infty) \to \infty$, to fulfill the boundary condition below:

$$\overline{C_{mD}}(r_D \to \infty, p) = 0 \, . \tag{B.14}$$

A_2 has to be zero. Now Eq. (B.13) is

$$\overline{C_{mD}} = A_1 \exp\left(\frac{y}{2}\right) Ai(\beta^{\frac{1}{3}} y) \, . \tag{B.15}$$

The boundary condition at the interacting surface of the injection well is given as:

$$\overline{C_{mD}}\left(r_{oD} = \frac{r_0}{d}, p\right) = \frac{1}{p} \quad . \tag{B.16}$$

The parameter A_1 can be expressed:

$$A_1 = \frac{1}{p}\exp\left(-\frac{1}{2}r_{0D} - \frac{1}{2}\left(4\beta\right)^{-1}\right)Ai^{-1}\left[\beta^{\frac{1}{3}}\left(r_D + \left(4\beta\right)^{-1}\right)\right] . \tag{B.17}$$

Now, the solutions in the Laplace domain could be reached.

By using the dimensionless parameters above, the dimensionless masses stored in the fracture-rock matrix system of radial flow are given as:

$$M_{fmD} = \int_{r_{0D}}^{\infty} \frac{4\pi b\theta_m\sqrt{R_3 A}}{d\sqrt{R_1 D_d}} r_D C_{mD} dr_D , \tag{B.18}$$

$$M_{fimD} = \int_{r_{0D}}^{\infty} \frac{4\pi b\theta_{im}\sqrt{R_3 A}}{d\sqrt{R_1 D_d}} r_D C_{imD} dr_D , \tag{B.19}$$

$$M_{kD} = \int_{\frac{b}{d\sqrt{\frac{R_1 D_d}{R_3 A}}}}^{\infty} \int_{r_{0D}}^{\infty} 4\pi\theta_k r_D C_{kD}\, dr_D dz_D . \tag{B.20}$$

APPENDIX C

DERIVATION OF REACTIVE SOLUTE TRANSPORT IN AN ASYMMETRIC FRACTURE SYSTEM

The dimensionless variables used in this study are defied as follows:

$$C_D = C / C_0\,,\ C_{1D} = C_1 / C_0\,,\ C_{2D} = C_2 / C_0\,,\ x_D = x / b\,,\ z_D = \frac{z}{b}\sqrt{\frac{R_2 D}{R D_1}}\,,\ t_D = \frac{D}{Rb^2}t\,,$$

$$Pe = \frac{vb}{D}\ ,\alpha = \frac{Rb^2}{D}\,,\ M_D = \frac{M}{C_0 \times \mathrm{b}^2 \times \sqrt{\frac{RD_1}{R_2 D}}}\ ,\ M_{1D} = \frac{M_1}{C_0 \times \mathrm{b}^2 \times \sqrt{\frac{RD_1}{R_2 D}}}\,,$$

$$M_{2D} = \frac{M_2}{C_0 \times \mathrm{b}^2 \times \sqrt{\frac{RD_1}{R_2 D}}}\ .$$

With the help of those dimensionless parameters above, the non-dimensional governing equations (Eqs. (3.1)-(3.3)) are transformed to the dimensionless formats:

$$\frac{\partial C_D}{\partial t_D} = \frac{\partial^2 C_D}{\partial x_D^2} - Pe\frac{\partial C_D}{\partial x_D} - \lambda\alpha C_D + \frac{\theta_1}{2\theta}\sqrt{\frac{R_2 D_1}{RD}}\left.\frac{\partial C_{1D}}{\partial z_D}\right|_{z_D = z_{0D}} - \frac{\theta_2}{2\theta}\sqrt{\frac{R_2 D_2^2}{RD_1 D}}\left.\frac{\partial C_{2D}}{\partial z_D}\right|_{z_D = -z_{0D}}\ , \quad \text{(C.1)}$$

$$\frac{\partial C_{1D}}{\partial t_D} = \frac{R_2}{R_1}\frac{\partial^2 C_{1D}}{\partial z_D^2} - \lambda_1 \alpha C_{1D}\,, \quad \text{(C.2)}$$

$$\frac{\partial C_{2D}}{\partial t_D} = \frac{D_2}{D_1}\frac{\partial^2 C_{2D}}{\partial z_D^2} - \lambda_2 \alpha C_{2D}\,. \quad \text{(C.3)}$$

After applying Laplace transform to Eqs. (C.1)-(C.3), the following equations would be obtained:

$$p\overline{C_D} = \frac{d^2\overline{C_D}}{dx_D^2} - Pe\frac{d\overline{C_D}}{dx_D} - \lambda\alpha\overline{C_D} + \frac{\theta_1}{2\theta}\sqrt{\frac{R_2 D_1}{RD}}\left.\frac{\partial \overline{C_{1D}}}{\partial z_D}\right|_{z_D = z_{0D}} - \frac{\theta_2}{2\theta}\sqrt{\frac{R_2 D_2^2}{RD_1 D}}\left.\frac{\partial \overline{C_{2D}}}{\partial z_D}\right|_{z_D = -z_{0D}}\ , \quad \text{(C.4)}$$

$$p\overline{C_{1D}}=\frac{R_2}{R_1}\frac{\partial^2\overline{C_{1D}}}{\partial z_D^2}-\lambda_1\alpha\overline{C_{1D}}\,, \tag{C.5}$$

$$p\overline{C_{2D}}=\frac{D_2}{D_1}\frac{\partial^2\overline{C_{2D}}}{\partial z_D^2}-\lambda_2\alpha\overline{C_{2D}}\,, \tag{C.6}$$

where p is the Laplace transform parameter in respect to the dimensionless time, t_D and overbar means the term in Laplace domain. From Eqs. (C.5)-(C.6), one has:

$$\frac{\partial^2\overline{C_{1D}}}{\partial z_D^2}=\frac{R_1}{R_2}(\lambda_1\alpha+p)\overline{C_{1D}}\,, \tag{C.7}$$

$$\frac{\partial^2\overline{C_{2D}}}{\partial z_D^2}=\frac{D_1}{D_2}(\lambda_2\alpha+p)\overline{C_{2D}}\,. \tag{C.8}$$

The general solutions of the Eqs. (C.7)-(C.8) are:

$$\overline{C_{1D}}=A_1e^{w_1z_D}+B_1e^{-w_1z_D}\ , \tag{C.9}$$

$$\overline{C_{2D}}=A_2e^{w_2z_D}+B_2e^{-w_2z_D}\,, \tag{C.10}$$

Where $w_1=\sqrt{\frac{R_1}{R_2}(\lambda_1\alpha+p)}$, $w_2=\sqrt{\frac{D_1}{D_2}(\lambda_2\alpha+p)}$.

Recalling the boundary conditions of rock matrix at infinity (Eq. (3.9)), Eqs. (C.9)-(C.10) can be further simplified as:

$$\overline{C_{1D}}=B_1e^{-w_1z_D}\,, \tag{C.11}$$

$$\overline{C_{2D}}=A_2e^{w_2z_D}\,. \tag{C.12}$$

After substituting in boundary conditions (Eqs. (3.6)-(3.8)), one can acquire:

$$\overline{C_{1D}}=\overline{C_D}\times\exp\left[-\sqrt{\frac{R_1}{R_2}\left(p+\lambda_1\alpha\right)}\left(z_D-\sqrt{\frac{R_2D}{RD_1}}\right)\right]\,, \tag{C.13}$$

$$\overline{C_{2D}} = \overline{C_D} \times \exp\left[\sqrt{\frac{D_1}{D_2}\left(p+\lambda_2\alpha\right)}\left(z_D + \sqrt{\frac{R_2 D}{R D_1}}\right)\right], \tag{C.14}$$

where $k_1 = \lambda\alpha + p + \frac{\theta_1}{2\theta}\sqrt{\frac{R_1 D_1}{RD}\left(p+\lambda_1\alpha\right)} + \frac{\theta_2}{2\theta}\sqrt{\frac{R_2 D_2}{RD}\left(p+\lambda_2\alpha\right)}$.

Substituting Eqs. (C.13)-(C.14) and the first-type boundary condition Eq. (3.10) into Eq. (C.4), the final solutions and the diffusion loss under the first-type condition can be reached:

$$\overline{C_D} = \frac{1}{p}\exp\left(\frac{Pe - \sqrt{Pe^2 + 4k_1}}{2} x_D\right), \tag{C.15}$$

$$\overline{C_{1D}} = \frac{1}{p}\exp\left[\frac{Pe - \sqrt{Pe^2 + 4k_1}}{2} x_D - \sqrt{\frac{R_1}{R_2}\left(p+\lambda_1\alpha\right)}\left(z_D - \sqrt{\frac{R_2 D}{R D_1}}\right)\right], \tag{C.16}$$

$$\overline{C_{2D}} = \frac{1}{p}\exp\left[\frac{Pe - \sqrt{Pe^2 + 4k_1}}{2} x_D + \sqrt{\frac{D_1}{D_2}\left(p+\lambda_2\alpha\right)}\left(z_D + \sqrt{\frac{R_2 D}{R D_1}}\right)\right], \tag{C.17}$$

$$\overline{q_1} = \frac{1}{p}\frac{\theta_1 D_1}{b}\sqrt{\frac{R_1 D}{R D_1}\left(p+\lambda_1\alpha\right)}\exp\left[\frac{Pe - \sqrt{Pe^2 + 4k_1}}{2} x_D\right], \tag{C.18}$$

$$\overline{q_2} = \frac{1}{p}\frac{\theta_2 D_2}{b}\sqrt{\frac{R_2 D}{R D_2}\left(p+\lambda_2\alpha\right)}\exp\left[\frac{Pe - \sqrt{Pe^2 + 4k_1}}{2} x_D\right]. \tag{C.19}$$

It is the similar method to solve the problem under the third-type boundary condition Eq. (3.11), the final solutions are:

$$\overline{C_D} = \frac{1}{p} \times \frac{2}{1 + \sqrt{1 + 4k_1 / Pe^2}}\exp\left(\frac{Pe - \sqrt{Pe^2 + 4k_1}}{2} x_D\right), \tag{C.20}$$

$$\overline{C_{1D}} = \frac{1}{p} \times \frac{2}{1+\sqrt{1+4k_1/Pe^2}} \exp\left[\frac{Pe-\sqrt{Pe^2+4k_1}}{2} x_D - \sqrt{\frac{R_1}{R_2}\left(p+\lambda_1\alpha\right)} \left(z_D - \sqrt{\frac{R_2 D}{RD_1}} \right) \right], \tag{C.21}$$

$$\overline{C_{2D}} = \frac{1}{p} \times \frac{2}{1+\sqrt{1+4k_1/Pe^2}} \exp\left[\frac{Pe-\sqrt{Pe^2+4k_1}}{2} x_D + \sqrt{\frac{D_1}{D_2}\left(p+\lambda_2\alpha\right)} \left(z_D + \sqrt{\frac{R_2 D}{RD_1}} \right) \right]. \tag{C.22}$$

Converting the mass stored in each domain (Eqs. (3.32)-(3.34)) into corresponding dimensionless formats defined above, the dimensionless mass per unit width stored in each domain is given as:

$$M_D = 2\theta \sqrt{\frac{R_2 D}{RD_1}} \int_0^{\infty} C_D dx_D \,, \tag{C.23}$$

$$M_{1D} = \int_{\sqrt{\frac{R_2 D}{RD_1}}}^{\infty} \int_0^{\infty} C_{1D} \times \theta_1 dx_D dz_D \,, \tag{C.24}$$

$$M_{2D} = \int_{-\infty}^{-\sqrt{\frac{R_2 D}{RD_1}}} \int_0^{\infty} C_{2D} \theta_2 dx_D dz_D \,. \tag{C.25}$$

For the back-diffusion problem, the water starts flushing the system after t_0. The diffusion coefficients after water flushing may change to D_{1b}, D_{2b}, D_b:

$$D_{1b} = a_1 D_1 \,,\; D_{2b} = a_2 D_2 \,, D_b = aD \,. \tag{C.26}$$

For the back-diffusion process, the governing equations are similar as:

$$\frac{\partial C_D}{\partial t_D} = a\frac{\partial^2 C_D}{\partial x_D^2} - Pe\frac{\partial C_D}{\partial x_D} - \lambda\alpha C_D + \frac{\theta_1 a_1}{2\theta}\sqrt{\frac{R_2 D_1}{RD}}\left.\frac{\partial C_{1D}}{\partial z_D}\right|_{z_D=z_{0D}} - \frac{\theta_2 a_2}{2\theta}\sqrt{\frac{R_2 D_2^2}{RD_1 D}}\left.\frac{\partial C_{2D}}{\partial z_D}\right|_{z_D=-z_{0D}}, \tag{C.27}$$

$$\frac{\partial C_{1D}}{\partial t_D} = a_1\frac{R_2}{R_1}\frac{\partial^2 C_{1D}}{\partial z_D^2} - \lambda_1\alpha C_{1D}, \tag{C.28}$$

$$\frac{\partial C_{2D}}{\partial t_D} = a_2\frac{D_2}{D_1}\frac{\partial^2 C_{2D}}{\partial z_D^2} - \lambda_2\alpha C_{2D}. \tag{C.29}$$

Following the similar method, the solutions during back diffusion are:

$$\overline{C_D}' = -\frac{1}{p}\exp\left(\frac{Pe-\sqrt{Pe^2+4k_2 a}}{2a}x_D\right), \tag{C.30}$$

$$\overline{C_{1D}}' = -\frac{1}{p}\exp\left[\frac{Pe-\sqrt{Pe^2+4k_2 a}}{2a}x_D - \sqrt{\frac{R_1}{a_1 R_2}\left(p+\lambda_1\alpha\right)}\left(z_D-\sqrt{\frac{R_2 D}{RD_1}}\right)\right], \tag{C.31}$$

$$\overline{C_{2D}}' = -\frac{1}{p}\exp\left[\frac{Pe-\sqrt{Pe^2+4k_2 a}}{2a}x_D + \sqrt{\frac{D_1}{a_2 D_2}\left(p+\lambda_2\alpha\right)}\left(z_D+\sqrt{\frac{R_2 D}{RD_1}}\right)\right], \tag{C.32}$$

where $k_2 = \lambda\alpha + p + \frac{\theta_1}{2\theta}\sqrt{\frac{R_1 D_1 a_1}{RD}\left(p+\lambda_1\alpha\right)} + \frac{\theta_2}{2\theta}\sqrt{\frac{R_2 D_2 a_2}{RD}\left(p+\lambda_2\alpha\right)}$.

The overall final solutions are:

$$C = \begin{cases} f(x,z,t) & t \le t_0 \\ f(x,z,t)+g(x,z,t-t_0) & t > t_0 \end{cases}, \tag{C.33}$$

where *f* (*x*,*z*,*t*) is the solution (Eqs. (C.15)-(C.17)) before water flushing, *g* (*x*,*z*,*t*) is the solution (Eqs. (3.30)-(3.31)) during water flushing time period.

APPENDIX D

DERIVATION OF REACTIVE SOLUTE TRANSPORT IN A STRATIFIED SYSTEM WITH SCALE DEPENDENT DISPERSIVITY

The governing equation of solute transport in the permeable layer is as follow:

$$\theta R \frac{\partial C}{\partial t} = \theta \frac{\partial}{\partial x}\left[D(x) \frac{\partial C}{\partial x} \right] - \theta v \frac{\partial C}{\partial x} - \theta \lambda R C - \frac{q_1}{2b} - \frac{q_2}{2b} . \tag{D.1}$$

The terms q_1 and q_2 refer to the diffusive mass entering the less permeable layers, which are expressed as:

$$q_1 = -\theta_1 D_1 \left. \frac{\partial C_1}{\partial z} \right|_{z=b} , \tag{D.2}$$

$$q_2 = \theta_2 D_2 \left. \frac{\partial C_2}{\partial z} \right|_{z=-b} . \tag{D.3}$$

A contaminant source at constant concentration is placed at the left boundary condition, which is also called the first type boundary condition and is expressed as:

$$C(x=0,t) = C_0 . \tag{D.4}$$

The governing equations of solute transport in the upper layer (layer 1) and lower layer (layer 2) are respectively:

$$R_1 \frac{\partial C_1}{\partial t} = D_1 \frac{\partial^2 C_1}{\partial z^2} - \lambda_1 R_1 C_1 , \tag{D.5}$$

$$R_2 \frac{\partial C_2}{\partial t} = D_2 \frac{\partial^2 C_2}{\partial z^2} - \lambda_2 R_2 C_2 . \tag{D.6}$$

The entire system is free of solute at beginning:

$$C(x,t=0) = C_1(x,z,t=0) = C_2(x,z,t=0) = 0 . \tag{D.7}$$

The permeable layer is considered as infinitely long and the less permeable layers are considered as infinity thick. Thus, we have:

$$C(x \to \infty, t) = 0\,,\ C_1(x, z \to \infty, t) = 0\,, C_2(x, z \to -\infty, t) = 0\,. \tag{D.8}$$

The concentrations at the interfaces of different layers are continuous:

$$C_1(x, z = b, t) = C(x, t)\,,\ C_2(x, z = -b, t) = C(x, t)\,. \tag{D.9}$$

The technique of Laplace transform is adopted here. Eqs. (D.1), (D.5) and (D.6) are then transformed into Laplace domain as:

$$D(x)\frac{d^2\overline{C}}{dx^2} + \left[\frac{dD(x)}{dx} - v\right]\frac{d\overline{C}}{dx} - \Psi\overline{C} = 0\,, \tag{D.10}$$

$$R_1\overline{C_1} = D_1\frac{\partial^2\overline{C_1}}{\partial z^2} - \lambda_1 R_1\overline{C_1}\,, \tag{D.11}$$

$$R_2\overline{C_2} = D_2\frac{\partial^2\overline{C_2}}{\partial z^2} - \lambda_2 R_2\overline{C_2}\,, \tag{D.12}$$

where $\Psi = pR + \lambda R + \frac{\theta_1}{2b\theta}\sqrt{(p+\lambda_1)R_1D_1} + \frac{\theta_2}{2b\theta}\sqrt{(p+\lambda_2)R_2D_2}$, p is the Laplace transform parameter and the over bar means the terms in Laplace domain.

With the consideration of continuous concentration at interfaces of layers (Eq. (D.9)), Eqs. (D.11)-(D.12) can be solved as follows:

$$\overline{C_1} = \overline{C} \times \exp\left[-\sqrt{\frac{pR_1 + \lambda_1 R_1}{D_1}}(z-b)\right]\,, \tag{D.13}$$

$$\overline{C_2} = \overline{C} \times \exp\left[\sqrt{\frac{pR_2 + \lambda_2 R_2}{D_2}}(z+b)\right]\,. \tag{D.14}$$

For the case of a linear scale-dependent dispersivity, one has: $D(x) = \alpha(x) \times v + D_0$, where $\alpha(x) = kx$. Substituting this relationship into Eq. (D.10), we have:

$$(kvx + D_0)\frac{d^2\overline{C}}{dx^2} + \left[kv - v\right]\frac{d\overline{C}}{dx} - \Psi\overline{C} = 0\,. \tag{D.15}$$

Defining a new variable $\xi_1 = \sqrt{kvx + D_0}$, then the equation above turns to:

$$\xi_1^{\,2}\frac{d^2\overline{C}}{d\xi_1^{\,2}} + \left[1 - \frac{2}{k}\right]\xi_1\frac{d\overline{C}}{d\xi_1} - \left(\frac{2}{kv}\right)^2 \xi_1^{\,2}\Psi\overline{C} = 0\,. \tag{D.16}$$

This equation has the form of the following Bessel equation:

$$\xi_1^{\,2}\frac{d^2\overline{C}}{d\xi^2} + \left[1 - 2\gamma\right]\xi_1\frac{d\overline{C}}{d\xi_1} + \left(-\delta^2\eta^2\xi_1^{\,2n} + \gamma^2 - \gamma^2\eta^2\right)\overline{C} = 0\,, \tag{D.17}$$

where $\gamma = \frac{1}{k}$ $, \delta = \frac{2}{kv}\sqrt{\Psi}$ $, \eta = 1$. It have been proven that $\xi_1^{\,\gamma} I_\gamma(\delta\xi_1^{\,\eta})$ and $\xi_1^{\,\gamma} K_\gamma(\delta\xi_1^{\,\eta})$ are two independent special solutions of the equation, where $I_\gamma(x)$ and $K_\gamma(x)$ are the first and second kinds of modified Bessel functions with the order γ. Therefore, the general solution of this equation is:

$$\overline{C} = \xi_1^{\,\gamma}\left\{A_1 K_\gamma(\delta\xi_1) + B_1 I_\gamma(\delta\xi_1)\right\}, \tag{D.18}$$

where A_1 and B_1 are two constants. According to the boundary condition (Eq. (D.8)), when $\xi_1 \to \infty$, $\overline{C}$ is finite. Thus, B_1 equals to zero. The solution could be simplified as:

$$\overline{C} = \xi_1^{\,\gamma} A_1 K_\gamma(\delta\xi_1)\,. \tag{D.19}$$

After substituting in boundary condition $\overline{C}\left(x = 0, p\right) = \frac{C_0}{p}$, one can acquire:

$$A_1 = \frac{1}{p}\frac{C_0}{\left(\sqrt{D_0}\right)^{\gamma} K_{\gamma}(\delta\sqrt{D_0})}\,. \tag{D.20}$$

The final solution in Laplace domain can be derived now as:

$$\overline{C} = \xi_1^{\gamma}\,\frac{1}{p}\frac{C_0}{\left(\sqrt{D_0}\right)^{\gamma} K_{\gamma}(\delta\sqrt{D_0})}K_{\gamma}(\delta\xi_1)\,. \tag{D.21}$$

For the case of an exponential scale-dependent dispersivity, the dispersivity can be expressed as: $\alpha(x) = a(1-e^{-k_1x})$. Thus, the governing equation could be rewritten as:

$$\left[a(1-e^{-k_1x})\times v + D_0\right]\frac{d^2\overline{C}}{dx^2} + \left[ak_1ve^{-k_1x} - v\right]\frac{d\overline{C}}{dx} - \Psi\overline{C} = 0\,. \tag{D.22}$$

Defining two variables: $\xi_2 = He^{k_1x}$, $H = 1 + D_0/(av)$, Eq. (D.22) can be expressed as:

$$\xi_2(1-\xi_2)\frac{d^2\overline{C}}{d\xi_2^{\,2}} - \left(1-\frac{1}{ak_1H}\right)\xi_2\frac{d\overline{C}}{d\xi_2} + \frac{1}{Havk_1^2}\psi\overline{C} = 0\,. \tag{D.23}$$

The above equation has the form of the following Gauss hypergeometric equation:

$$\xi_2(1-\xi_2)\frac{d^2\overline{C}}{d\xi_2^{\,2}} + \left[Q - \left(1+m+n\right)\right]\xi_2\frac{d\overline{C}}{d\xi_2} - mn\overline{C} = 0\,, \tag{D.24}$$

where $Q = 0$, $m = \frac{1}{2ak_1H}\left[-1+\sqrt{1+\frac{4aH}{v}\psi}\right]$, and $n = \frac{1}{2ak_1H}\left[-1-\sqrt{1+\frac{4aH}{v}\psi}\right]$.

As $1 \le \xi_2 \le \infty$, the solution can be written in terms of the hypergeometric function as follows:

$$\overline{C} = A_2\xi_2^{-m}F\left(m, m+1; m-n+1; \xi_2^{-1}\right) + B_2\xi_2^{-n}F\left(n, n+1; n-m+1; \xi_2^{-1}\right), \tag{D.25}$$

where $F\left(m, m+1; m-n+1; \xi_2^{-1}\right)$ and $F\left(n, n+1; n-m+1; \xi_2^{-1}\right)$ are the Gauss hypergeometric functions.

In terms of the outlet boundary condition (Eq. (D.8)), the concentration remain finite when $\xi_2 \to \infty$. Thus, the B_2 must equal zero as n is less than zero. The solution can be simplified as:

$$\overline{C} = A_2 \xi_2^{-m} F\left(m, m+1; m-n+1; \xi_2^{-1}\right). \tag{D.26}$$

After substituting $\overline{C}\left(x=0, p\right) = \frac{C_0}{p}$, A_2 could be solved as:

$$A_2 = \frac{C_0\left(1+\frac{D_0}{av}\right)^m}{pF\left(m, m+1; m-n+1; \left(1+\frac{D_0}{av}\right)^{-1}\right)} \ . \tag{D.27}$$

The final solution is then derived as:

$$\overline{C} = \frac{C_0\left(1+\frac{D_0}{av}\right)^m}{pF\left(m, m+1; m-n+1; \left(1+\frac{D_0}{av}\right)^{-1}\right)} \xi_2^{-m} F\left(m, m+1; m-n+1; \xi_2^{-1}\right). \tag{D.28}$$